University of Stavanger

Faculty of Science and Technology

MASTER'S THESIS

Study program/ Specialization: **Petroleum Engineering** **Drilling And Well Technology**	Spring semester, 2013 **Open Access**
Writer: **Hans Petter Lande**	…… (Writer's signature)

Faculty supervisor: Mesfin A. Belayneh, University of Stavanger (UiS)

External supervisor: Eric Cayeux, International Research Institute of Stavanger (IRIS)

Title of thesis:

Analysis of the Factors Influencing the Annulus Pressure Far Away From Downhole Pressure Measurements

Credits (ECTS): **30**

Key words: • Annulus pressure uncertainty • Wellbore position uncertainty • Survey errors • Systematic and cumulative errors • Wellbore pressure modeling • Cuttings transportation • Geothermal properties uncertainty	Pages: **169** Stavanger, June 13, 2013

Universitetet i Stavanger

IRIS
International Research Institute of Stavanger

Analysis of the Factors Influencing the Annulus Pressure Far Away From Downhole Pressure Measurements

Hans Petter Lande

Master's thesis

June 13, 2013

Institute of Petroleum Technology
University of Stavanger

Acknowledgments

This thesis is submitted in fulfillment of the requirements for a Master's Degree in Petroleum Technology at the University of Stavanger (UiS), Stavanger, Norway. The work took place at the International Research Institute of Stavanger (IRIS) in the period January – June 2013.

The idea behind this thesis was provided courtesy of my external supervisor, Eric Cayeux (IRIS), to whom I wish to extend my full gratitude. He always took the time to share his expertise within the fields of wellbore position uncertainty and software development and gave guidance and support throughout this whole project. I would also like to thank everyone else at the E-FORCE Realtime Research Center at IRIS for their friendliness and for taking their time to help whenever needed. Last but not least, I wish to thank my faculty supervisor Mesfin Belayneh (UiS) for all his guidance, advice and support.

Stavanger, June 2013

Hans Petter Lande

Abstract[1]

In any drilling operation, it is important to maintain the annulus pressure within the geo-pressure margins (collapse and pore pressure on one side and fracturing pressure on the other side). The downhole pressure management may simply consist of limiting the operational drilling parameters (flow-rate, pump acceleration, rotational and axial velocities and accelerations of the drill-string) in such a way that the downhole pressure stays within the open hole formation pressure window.

In Practice, the downhole pressure is only sparsely measured, both in time and depth. With traditional mud pulse telemetry, it is only possible to have sensors in the direct vicinity of the MWD (Measurement While Drilling) tool and because of the low communication bandwidth, the measurement sampling interval is seldom better than half a minute. Even with the best downhole telemetry system available for drilling (wired pipe data transmission), the sampling interval is about five seconds and multiple pressure sensors, if any, are usually distant by 300 – 400 m. Considering that the speed of sound in drilling fluids is usually more than 1000m/s, it is not possible to capture, with currently available downhole pressure instrumentation, any of the transient pressure pulses that may cause problems during a drilling operation. To compensate for this deficiency, simulations of the downhole pressure using mathematical models are used to fill the gaps, in space and time, between the downhole and surface pressure measurements.

However there are external factors that influence the accuracy of such models. For instance, the actual wellbore position is derived from indirect measurements: the inclination, the azimuth and the measured depth at the measurement. These angles and length measurements can be biased by systematic errors that can result in a miscalculation of the position of the well. As a consequence, an over or under estimation of the actual vertical depth of the well may introduce discrepancies in the estimation of the downhole pressure. Other sources of inaccuracies are the actual temperature gradient along the well, the proportion of cuttings in suspension, the presence of gas in the drilling fluid, the variations of borehole size due to

[1] This abstract has been accepted by the SIMS 2013 committee, awaiting full paper to be submitted by August 15, 2013.

cuttings beds or hole enlargements. Any of these elements influences the accuracy of the pressure prediction made by models, especially at some distance from the downhole measurement location. This thesis presents quantitative and qualitative estimations of the influence of these factors on the pressure estimation accuracy.

Table of contents

List of figures

List of tables

List of abbreviations

BHA	Bottom Hole Assembly
BHP	Bottomhole Pressure
DLS	Dogleg Severity
ECD	Equivalent Circulating Density
EMW	Equivalent Mud Weight
ERD	Extended-Reach Drilling
HPHT	High Pressure High Temperature
ID	Inner Diameter
LCM	Lost Circulation Material
MD	Measured Depth
MPD	Manage Pressure Drilling
MSL	Mean Sea-Level
NPT	Non-Productive Time
OD	Outer Diameter
OMB	Oil-Based Mud
OWR	Oil-Water Ratio
ppm	Parts Per Million
PVT	Pressure Volume Temperature
PWD	Pressure While Drilling
P-ρ-T	Pressure Density Temperature
ROP	Rate Of Penetration
RPM	Revolutions Per Minute
SBM	Synthetic Based Mud
SH	Specific Heat (capacity)
TC	Thermal Conductivity
TD	Target Depth (or Total Depth)
TVD	Total Vertical Depth
WBM	Water-Based Mud
WOB	Weight On Bit

Definitions

- **Wellbore position uncertainty** is a collective term representing the cumulative uncertainty in all the measured parameters related to the position of the wellbore (inclination, azimuth and measured depth). Uncertainty in these parameters originates from a number of systematic error sources which as a whole results in uncertainty in the actual placement of a wellbore.

- The **Covariance matrix** is (in this case) a 3x3 matrix holding the calculated variances of the borehole position vector in the north, east and vertical direction along with the covariance between these. A covariance matrix calculated at a survey station will, due to the systematic nature of error propagation, hold the cumulative uncertainty from all previous measurements.

- The volume in which the wellbore is located with a given confidence factor is represented by an **ellipsoid of uncertainty** (Figure 1), calculated from the covariance matrix**.** The ellipsoid is oriented according to the wellbore and will therefore undergo rotations in all directions as the wellbore changes inclination and azimuth.

- A **survey station** is a single depth in the well at which measurements are taken. In this context these measurements include: inclination, azimuth and measured depth.

- A **Survey** is a sequence of measurements taken, at the survey stations, in a borehole by the same survey instrument during a single run of the tool. The survey can include measurements taken while both running in – and pulling out of the well.

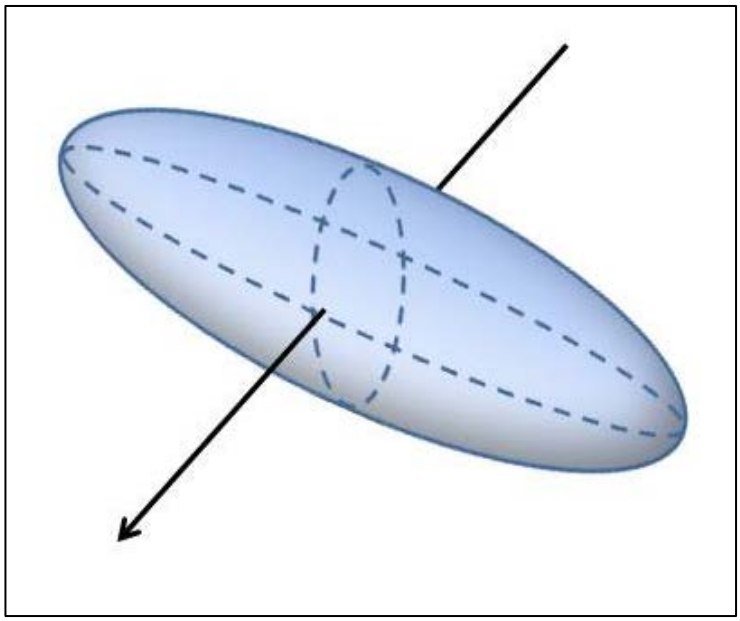

Figure 1: Ellipsoid of uncertainty

1 Introduction

1.1 Background for the thesis

At any time during the drilling operation it is critical to keep the wellbore pressure within the operational window confined by pore or collapse pressure on one side and fracture pressure on the other side as displayed in Figure 1.1. In steady state conditions, the wellbore pressure, p, as function of measured depth (MD) is given as the sum of the pressure at the start depth, p_0, the hydrostatic pressure and the frictional pressure loss. The two latter are given as integrals along the wellbore.

$$p(MD) = p_0 + \int_0^{MD} \rho_f g \cos I \, ds + \int_0^{MD} \frac{dp}{ds} ds \qquad \textbf{Equation 1.1}$$

Where I is the inclination and ρ_f is the fluid density. p_0 is usually atmospheric pressure, but in case of well control or back pressure MPD, this value can be larger than atmospheric pressure. It is usual to convert pressures into equivalent mud weights (EMW), i.e. a density, because it is then easier to relate any effects of other pressures to the mud weight. The conversion of a pressure into a density is simply based on the density of the fluid that would have caused the same pressure, in hydrostatic conditions, at the same true vertical depth, H.

$$p = p_{atm} + EMW\,gH \Longrightarrow \forall H \neq 0, EMW = \frac{p - p_{atm}}{gH} \qquad \textbf{Equation 1.2}$$

Drilling programs are designed to stay within the operating window with good margins, but in some cases wells have to be drilled with small margins; increasing the possibility of taking a kick, collapsing or fracturing. In these cases it is critical to have precise pressure control otherwise the results could be catastrophic. However large numbers of uncertainties are associated with determining the wellbore pressure including uncertainties in mud density, rheology and the wellbore position. The concept of systematically increasing wellbore position uncertainty has been a known fact to the industry since the early 1980's. However few analyses have been made discussing what implications this has on the wellbore pressure. This thesis provides a qualitative analysis of wellbore position uncertainty using existing uncertainty models. This uncertainty will be seen in connection with uncertainty in other

critical drilling parameters such as drilling fluid properties and geothermal properties of formation rocks.

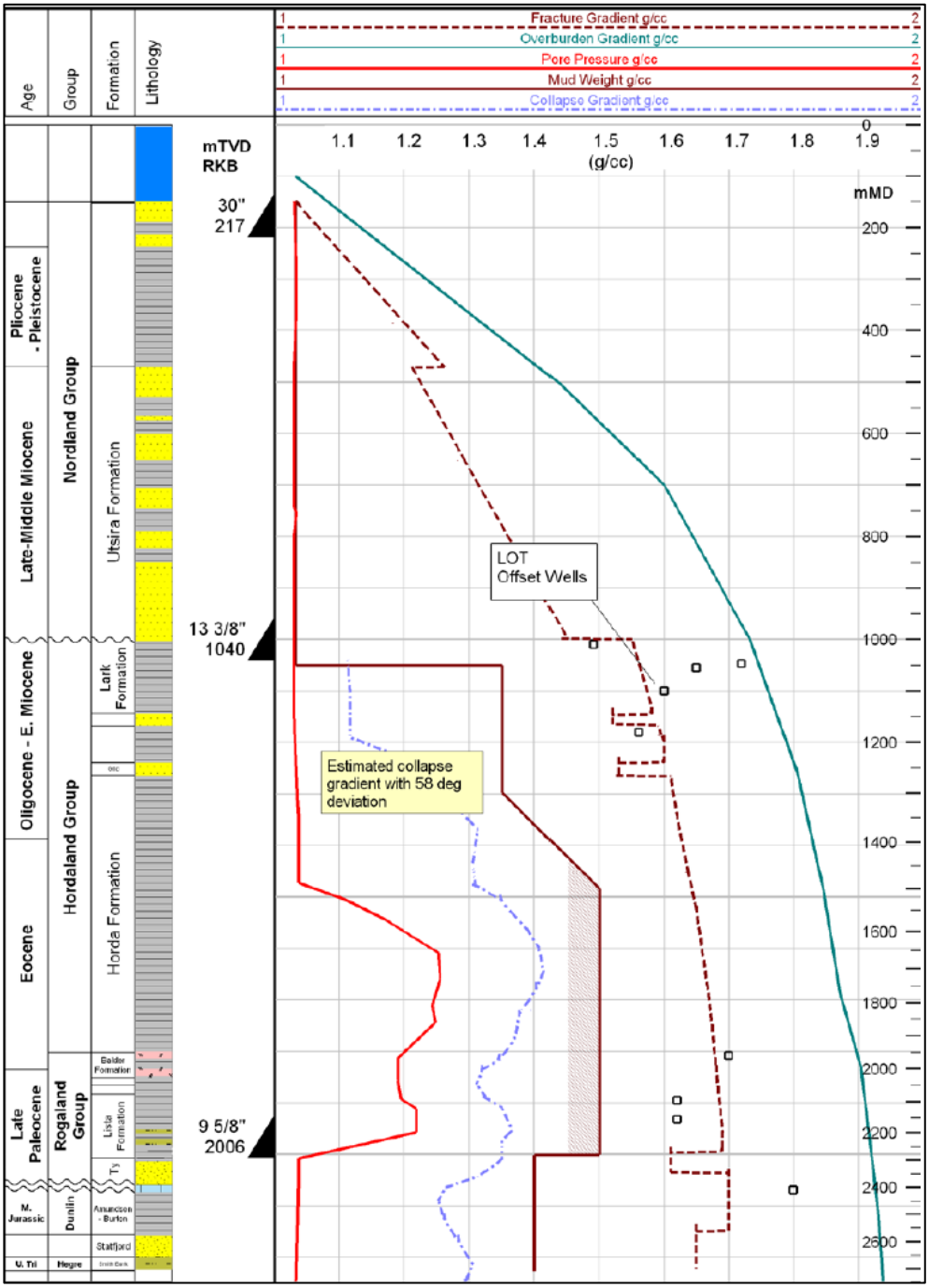

Figure 1.1: Typical pore pressure plot [1]

1.2 Assumptions and objective

The purpose of this thesis is to discuss and uncover sources that will produce uncertainties in the annulus pressure far away from downhole measurements and to some extent review the magnitude of these. Focus will first be directed to how wellbore position uncertainty will influence pressure uncertainties, in which case the vertical uncertainty is the most interesting. The objective is to simulate a situation where the pressure model has been calibrated to fit the most likely wellbore trajectory, but in reality the trajectory is located at one of the vertical extremities of the ellipsoid of uncertainty. To review the effect this will have on the pressure uncertainties further up the annulus, the two wellbores associated with these extremities reconstructed to uncover where these wellbore would be located at the point of investigation. Typically this point of interest will be right below the previous casing shoe or at a point where the margin between annulus pressure and the pore and fracture pressure is minimum.

The two most extreme wellbores in vertical depth variation are reconstructed based on a hypothesis that the wellbore position deviation compared to the measurements is due to the same source of systematic error on inclination, azimuth and MD all along the trajectory. Consequently, the position of the wellbores within an ellipsoid, derived at one survey station, will be the same at any other survey station in the well. This is only valid if the positions of the wellbores are given according to the local coordinate system of the ellipsoid itself. The hypothesis is supported by the theory of errors being systematic between survey stations, first introduced by Wolff and de Wardt [2]. Logical arguments can also be used to support the theory as it is reasonable to assume large degrees of consistency of the wellbore placement within successive ellipsoids.

The described method will have its basis in a covariance matrix providing the dimension for the ellipsoid of uncertainty. The covariance matrix itself is assumed to be known in this thesis. Calculation of this can be done according to the models by Wolff and de Wardt [2] or Williamson [3]. It is however, important to note that the method described does not rely on any specific error model to be used for calculating the covariance matrix.

The resulting pressure uncertainties from applying the minimum and maximum TVD trajectory will be analyzed in three different cases with wells of various lengths and shapes.

These uncertainties will be seen in connection with variations resulting from uncertainties in other downhole parameters such as the mud density, oil – water ratio and formation geothermal properties. Quantitative analysis of these uncertainties will be presented.

2 Analysis of wellbore position uncertainty and the effect on annulus pressure

In this section a qualitative analysis of the factors influencing the wellbore position uncertainty will be performed. Furthermore, derivation of a method to calculate maximum and minimum TVD from an ellipsoid uncertainty and reconstructing the wellbore trajectories according to these extremities will be presented.

2.1 Introduction to wellbore position uncertainty

The uncertainties involved with determination of the true course of a borehole have been a concern in the industry in the past 4 decades. Since then, many models have been produced with the intention of quantifying the borehole position uncertainties. To give a better understanding of the complex issue of wellbore position uncertainty, some of the most important contributions are mentioned below.

The pioneering work in wellbore position uncertainty was performed in the late 1960s. The objective was to explain why operators would experience large differences between various surveys made in the same well. As early as 1969 Walstrom et al. [4] introduced a wellbore position uncertainty model along with the ellipse of uncertainty. The ellipse later evolved into an ellipsoid and is widely used today in describing the wellbore position uncertainty. There was however a problem with the model by Walstrom et al. Error was considered as randomly occurring between survey stations. This meant that they would have a tendency to compensate each other, leading to a large underestimating of the position uncertainty and the ellipse size.

Then, in 1981 Wolff and de Wardt [2] published their model which by many is considered as the quantum leap of wellbore position uncertainty. The main reason for this is how Wolff and de Wardt realized that errors had to be considered as systematic from one survey station to another, but random between separate surveys and instruments. This meant that errors would get progressively larger throughout a survey and each ellipsoid would describe the cumulative uncertainty of the previous ellipsoids. Their work lead to a far more realistic approach in determining the magnitude of uncertainty, even though the model itself may be considered as relatively simple.

In 1990 Thorogood [5] expressed some concerns about the model developed by Wolff and de Wardt. He especially addressed the issue of all errors being considered as systematic between survey stations. He stated that this assumption may in some cases produced false results and explained this with the effect of axial rotation on misalignment errors. He developed a new model called IPM (Instrument Performance Model) but unfortunately this one has never been published.

In 1998 Ekseth [6] submitted his PhD dissertation which has become the basis for subsequent developments of error models and examinations techniques.

Until the late 1990s there was no industry standard on how to determine wellbore position uncertainty. This meant that every major operator swore by their own model. It was very important to have the best model, considering the largest number of variables. Then a group of industry experts gathered to form the Industry Steering Committee on Wellbore Survey Accuracy (ISCWSA) later known as the SPE Wellbore Positioning Technical Section (SPE-WPTS). The primary aim of the group is to produce and maintain standards for the industry relating to wellbore survey accuracy [7]. Their primary work, which became the industry standard, was published by Williamson in 1999 and updated in 2000 [3]. The initial model treated only magnetic measurements.

In 2004 Torkildsen et al. published an extension of the ISCWSA model. The model contained a new method for determining wellbore position uncertainty when surveyed with gyroscopic tools. This paper was revised for publication in 2008 [8].

2.2 Error model for wellbore position uncertainty

In this section the scope and application of a basic error model for wellbore position uncertainty will be explained. The purpose of this thesis is not to develop any new error model nor to modify on existing ones, but rather use the results of these for determining annulus pressure uncertainties. For simplicity reasons, the far less complicated model by Wolff and de Wardt [2] will therefore be used in this explanation.

As previously mentioned, Wolff and de Wardt developed their ground breaking model based on the assumption that errors could be considered as systematic throughout a survey, but vary randomly between separate surveys. In other words, the magnitude and direction of an error would within reason be considered as random from one survey to another, but would be consistent within a survey. This means that the error would grow progressively larger throughout subsequent survey stations. Accordingly, an ellipsoid calculated at one survey station will hold the cumulative uncertainty of the all survey stations taken to that point. This is what the model is based on.

The Wolff and de Wardt model has its basis in 6 uncertainty parameters. Each of those parameters corresponds to a random variable describing the source of the systematic error and a weighting factor that indicates how the local inclination and azimuth at the station influences the calculation on the wellbore position. The first three parameters; ΔC_1, ΔC_2 and ΔC_3 are related to compass errors:

$$\Delta C_1 = \Delta C_{10} \qquad \textbf{Equation 2.1}$$

ΔC_1 is related to the compass reference error, or the error within the compasses themselves. Apart from magnetic storms which could cause variation in the magnetic north by a few degrees, the compass reference error has proven to be consistent throughout a survey. These storm occur no more than 10 times a year and lasts only for a day. The parameter ΔC_1 is therefore described by its standard deviation: ΔC_{10}.

$$\Delta C_2 = \sin I \sin A \cdot \frac{\Delta B_Z}{B_N} = \sin I \sin A \cdot \Delta C_{20} \qquad \textbf{Equation 2.2}$$

ΔC_2 is the deflection of the compass as a result of magnetization by the drillstring. The actual bias on the compass readings depends on the direction of the borehole. Consequently, a weighting factor based on the inclination (I) and azimuth (A) is included. B_N is the horizontal (north-pointing) component of the Earth's magnetic field and ΔB_Z is the erroneous magnetic field in drillstring, in the Z direction. $\Delta C_{20} = \frac{\Delta B_Z}{B_N}$ is the standard deviation describing the effect of drill-string magnetization.

$$\Delta C_3 = \frac{1}{\cos I} \cdot \Delta C_{30} \qquad \textbf{Equation 2.3}$$

ΔC_3 is a variable describing the characteristics of a gyro compass. Generally speaking, the reliability of a free gyro, i.e. with two degrees of freedom decreases at higher inclinations and such a gyro will flip over randomly when used at inclinations close to horizontal. Hence the term $\frac{1}{\cos I}$, denoting decreasing performance of the gyrocompass as inclination increases. ΔC_{30} is the standard deviation characterizing the gyro compass error.

Given by the physical interpretation of these parameters, it is clear that ΔC_1 and ΔC_2 are related to magnetic compasses and ΔC_1 and ΔC_3 are related to gyrocompasses. The general compass error (ΔC) is made up of the parameters involved as follows:

$$\Delta C = \sqrt{\sum_i \Delta C_i^2} \qquad \textbf{Equation 2.4}$$

Parameters ΔI_m and ΔI_t represents the misalignment error and true inclination error respectively. Misalignment error is related to the tool not being centralized within the wellbore. If the tool is rotated this misalignment error can be conceived as a cone around the borehole with half the apex equal to ΔI_m. Misalignment errors are discussed further in section 2.3.2.

True inclination error differs from the misalignment error since it acts only in the vertical plane. The effect of the true inclination error is weighted by its deviation from vertical. ΔI_{to} is the standard deviation of the random variable describing the true inclination error:

$$\Delta I_t = \sin I \cdot \Delta I_{to} \qquad \textbf{Equation 2.5}$$

The sixth parameter is the relative depth error (ε), defined as the along hole depth error divided by the along hole depth. The relative depth error is related to measurement errors along the borehole axis, or uncertainties in MD. In general this error is due to elongation and compression of the drill string due to surface tension, weight on bit, temperature and pressure effect. However, other sources of faulty measurements may occur.

$$\varepsilon = \frac{\Delta D_{AH}}{D_{AH}} \qquad \textbf{Equation 2.6}$$

These parameters form the basis for calculating the covariance matrix and thereby also the ellipsoid of uncertainty. For magnetic cases, the center of the ellipsoid is displaced from the center of the wellbore due to geo-magnetic deflection. When drilling in the northern hemisphere the ellipsoid is displaced to the north-east. The coordinated for the center is given by the following equations:

$$N_{mag} = N + \Delta C_2 \cdot a_{21} \qquad \textbf{Equation 2.7}$$

$$E_{mag} = E + \Delta C_2 \cdot a_{22} \qquad \textbf{Equation 2.8}$$

Where N_{mag} and E_{mag} are the new coordinates for the center of the ellipsoid and E and N represent the initial coordinates. The accumulated directional change caused by geo-magnetic deflection of the compass (ΔC_2) is represented by a vector $\overrightarrow{a_{2J}}$, where a_{21} is the North facing component and a_{22} is the east facing component.

2.3 Sources of error

The wellbore position uncertainty is a result of contributions from a number of different sources. These sources have varying magnitude and significance for the total uncertainty. Some of the contributions such as considering the earth's curvature only have significance in very long wells. However, the number of different contributions will still cause wellbore positions uncertain, even in shorter wells. Some of the most significant of these contributors are mentioned in the following.

2.3.1 Compass errors

Compass errors are a large error source with a number of contributions. Two main groups of compasses exists namely; electronic magnetic compasses and gyroscopic compasses.

2.3.1.1 Electronic magnetic compasses

The magnetic tools consist of a set of accelerometers and magnetometers. The accelerometers are used to determine the inclination and toolface angle and the magnetometers will together with the accelerometers determine the magnetic azimuth. These sensors are specified to work within certain environmental limits of pressure, temperature, vibrations etc. and calibration is performed according to a predefined accuracy level. Measurements performed outside these limits will provide false results. [6]

The most obvious source of error lies within the instruments themselves. Both accelerometers and magnetometers are accompanied by uncertainty which can be grouped into a random component, a bias and a scale factor. Accelerometers may also be associated with a second order scale factor. This is, however, only significant when large accelerations are present. The bias and the scale factor uncertainty are systematic throughout a survey. These will account for most of the uncertainty, leaving the random component as insignificant in comparison [6]. The bias uncertainty is considered as randomly varying between instruments.

There are also a number of external factors that will affect accuracy of compasses. For magnetic compasses, most of these are a result of some sort of magnetic disturbance. The earth's magnetic field is built up of three major sub fields; the earth principal field, the local crust field and the atmospheric field. None of these fields are constant. They vary with both

geographic position and time. Large random fluctuations may occur, however this is unusual. Random fluctuations are therefore only be seen as significant when operating with confidence levels above 99,9 %. Daily variation will, however have large amplitudes and must therefore be accounted for [6]. When drilling at higher latitude, near the magnetic poles, there is a natural disturbance of the magnetic field which may cause additional problems. Magnetic field variation will also be depending on the types of rock present in the area. Generally, areas with volcanic rocks closer to the surface will show more variations than areas where sedimentary rocks dominate [3]. Daily shifting of the magnetic field will also be experienced as a result of magnetic storms which could cause variation in the magnetic north by a few degrees [2]. These error sources must be accounted for as estimates of the magnetic field are used directly in magnetic directional survey. The survey accuracy is therefore largely depending on the accuracy of these estimates.

Magnetization and magnetic shielding by other elements in the well is also common factors. Magnetic interference of the compass by magnetization will always occur due the vast presence of steel in the well. In order to reduce the effect of drillstring magnetization the practice is to mount the tool within the non-magnetic drill collar (NMDC) section. However local magnetic fields may be generated by the BHA and other structures made up of ferromagnetic materials such as casings, platforms, templates etc. in the drilled or in nearby wells. These fields may be very strong and significantly affect the survey quality [6].

Another substantial source of error to consider is magnetic shielding by the fluids present in the wellbore. Tellefsen et al. [9] highlighted the fact that additives like clays and weight materials and swarf from tubular wear will distort the geomagnetic field. Their analysis shows that both added weighting materials like bentonite and metal swarf in the well will have significant effect on magnetic shielding.

2.3.1.2 Gyroscopic compasses

Gyros are widely used for completion surveys and provide higher accuracy, especially in areas with high magnetic interference where magnetic compasses become less reliable. Gyro tools can also be incorporated in the drilling operation by the MWD gyro. The gyroscopic compass uses accelerometers and rotor gyros which together with the earth's rotation is able to determine geographical direction i.e. true north. A gyroscopic survey tool can contain up to three accelerometers and up to three single-axis, or two dual-axis gyroscopes installed in various configurations [8]. However, even though gyroscopic compasses can be more accurate than the magnetic compasses, they still have their weaknesses and related errors in orientation. Accelerometers and rotating gyroscopes in gyro tools have similar biases and scale factor errors as for electronic magnetic compasses. Errors in gyroscopes may be described as a product of reading errors and mass unbalances. Mass unbalances are a result of imperfect manufacturing changing with time due to effects like creep and thermal expansion. It can be defined as a standard deviation in the instrument calibration [6]. Gyrocompasses may also drift a substantial distance during surveys. Parameters that will affect the gyro drifting are the gyroscopic movement of inertia, earth's rotation, time, temperature, borehole orientation, DLS and running procedures. [8]

2.3.2 Misalignment errors

Misalignment errors may be grouped into three categories; sensor misalignment, instrument misalignment and collar misalignment. These are similar for both gyroscopic and magnetic tools. Sensor misalignment is a result of the assumption that the principal instrument axis (x, y, z) are forming a perfect orthogonal coordinate system. In general this is not the case and the result will be some small misalignment errors after sensors are calibrated [6].

Instrument misalignment is errors that are caused by the tool being out of position from the central line in the borehole. Ekseth [6] argues how instrument misalignment could be split into two components one in the x-y plane and one in the y-z plane. Accordingly, effects will be seen on both azimuth and inclination readings. As the errors are originating from the same misalignment these components are correlated. The instrument misalignment is seen as systematic for one instrument as long as the instrument is not damaged or the misalignment is corrected.

Collar misalignment is caused by borehole deformations, mechanical forces or gravity acting on the drill sting or wireline including washouts and key seats. These are random effects and as a result the contribution to the total position uncertainty is small. In MWD surveys, the vertical collar alignment is often referred to as sag or BHA sag, see Figure 2.1. This is a more complicated error source as it is depending on the actual BHA properties, drill string stiffness, weight on bit, stabilizers etc. [6]

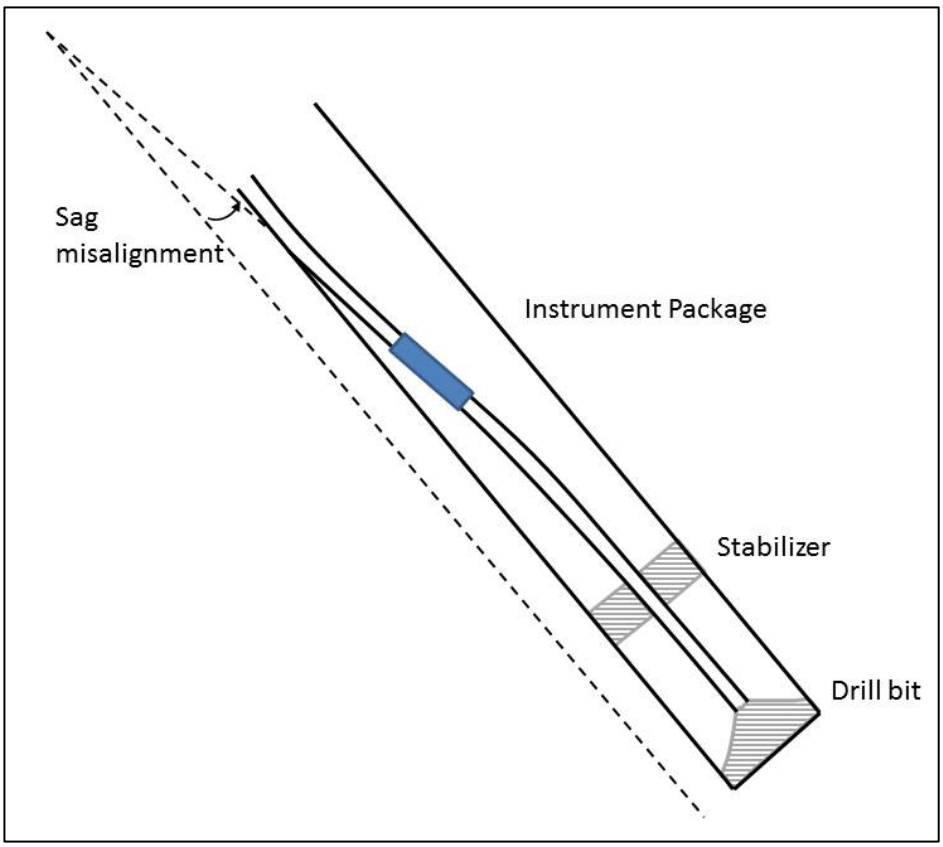

Figure 2.1: Schematic illustration of sag misalignment

2.3.3 Relative depth error

The relative depth error term is related to errors omitted when a false reference level for measurements is used. When a survey data set is used to compute wellbore displacement, these data sets are applied to a set of fixed station in the wellbore as displayed in Figure 2.2. The instrument is stopped at survey station corresponding to a certain MD to proceed with the measurements [5]. If there is a deviation between the actual location of the instrument and the depth of the survey station the result will be an inaccurate prediction of the wellbore curvature. Errors in MD measurement may occur from elongation of cable or drill pipe due to temperature, pressure or the effect of elasticity. Another error source may be the use of MSL as a reference or datum point. The sea level will change in cycles and may therefor differ from the mean value at the time of measurement.

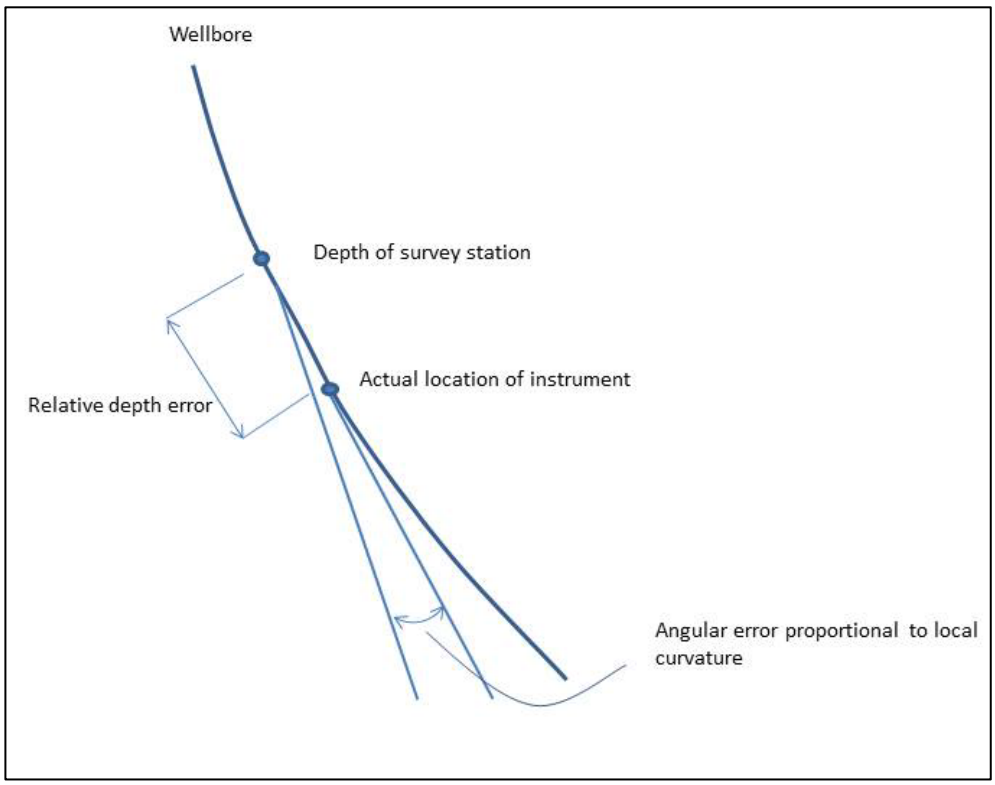

Figure 2.2: Effect of relative depth error

2.3.4 Earth's curvature

Curvature of the earth is an error source that not will have any insignificant effect on shorter wells, but will need to be taken into account when drilling longer ERD wells. For these well using a flat earth model and project the earth's surface onto a grid will be a source of error for the wellbore position. The general issue will lie within the source of reference for borehole positioning. If the well is drilled maintaining a constant angle with respect to the earth's gravity field the well will then follow the curvature of the earth. Whereas a well drilled with a gyro tool for maintain a constant local angle will not follow the earth's curvature and can create a deviation in long horizontal section. Williamson and Wilson [10] calculated that for a 10km well the error omitted by not considering the earth's curvature could be up to 10 m and likewise up to 3m for a 3km well.

2.3.5 Gross errors

Gross errors also known as human- or other larger random errors, is also something that should be mentioned in this context. Such errors do occur, however the extent and occurrence of these are purely random. These errors can occur at any time or anywhere during the well planning and drilling process. This makes prediction and modeling of these errors very difficult, but one should always be aware that they sometimes occur.

2.3.6 Wellbore tortuosity

Wellbores are generally speaking not straight, the shape will more precisely be described as curved or crooked. This occurs when drilling with bent-subs, downhole motors and different variations of rotary steerable systems. Wellbore tortuosity is a term describing this crookedness which may cause many drilling related problems such as increased torque and drag, increased tubular wear etc. [11] Effects can also be seen with respect to wellbore position uncertainty. When drilling in a crooked wellbore the limited flexibility of the drill pipe will not allow it to follow the wellbore completely. Instead it will go over the top of the curves. This will in practice imply that the wellbore actually is longer that the drill pipe inside. The magnitude of position error caused by wellbore tortuosity is not highly significant, but will still make some contribution to final result.

2.4 Converting measurements into borehole position uncertainty

As the magnitude of different survey errors are established, they can be quantified into a covariance matrix as given in Equation 2.9. The covariance matrix contains information regarding the variance in the north, east and vertical coordinates of a wellbore and the covariance between the error sources.

$$COV = \begin{bmatrix} var(N,N) & cov(N,E) & cov(N,V) \\ cov(N,E) & var(E,E) & cov(E,V) \\ cov(N,V) & cov(E,V) & var(V,V) \end{bmatrix} \quad \textbf{Equation 2.9}$$

The covariance matrix can be solved yielding the uncertainty volume in which the wellbore is placed. This is described as an ellipsoid of uncertainty, see Figure 2.3. In general the axial axis is related to relative depth error. The lateral axis is related to compass errors and misalignment errors and variance on the up-ward axis is caused by misalignment and true inclination errors:

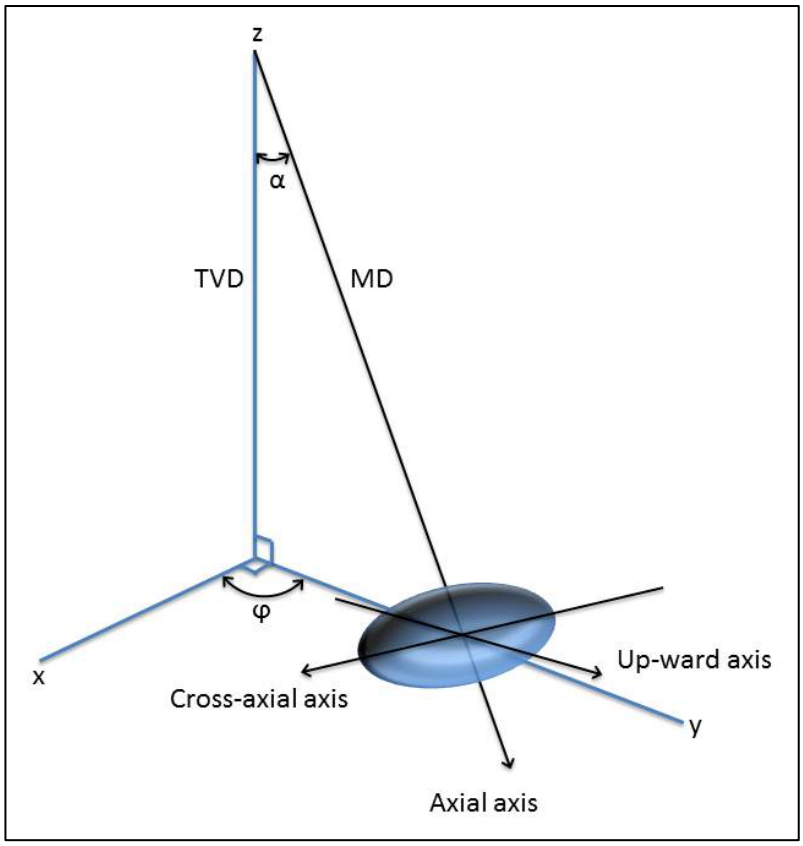

Figure 2.3: Ellipsoid of uncertainty with definition of axes

An important consideration regarding the ellipsoid of uncertainty is its confidence level. The confidence level of an ellipsoid explains to which degree of certainty the wellbore placement is actually within the ellipsoid. Thus, for a given set of data the size of the ellipsoid of uncertainty can be altered as appropriate with the confidence level changing accordingly. This implies that the ellipsoid by itself, not accompanied by some sort of confidence level, is essentially worthless. A visual display of this effect is shown in Figure 2.4, where ellipsoids with different confidence levels are obtained from the same covariance matrix. A set of standard confidence levels for Gaussian probability distributions are displayed in Table 2.1.

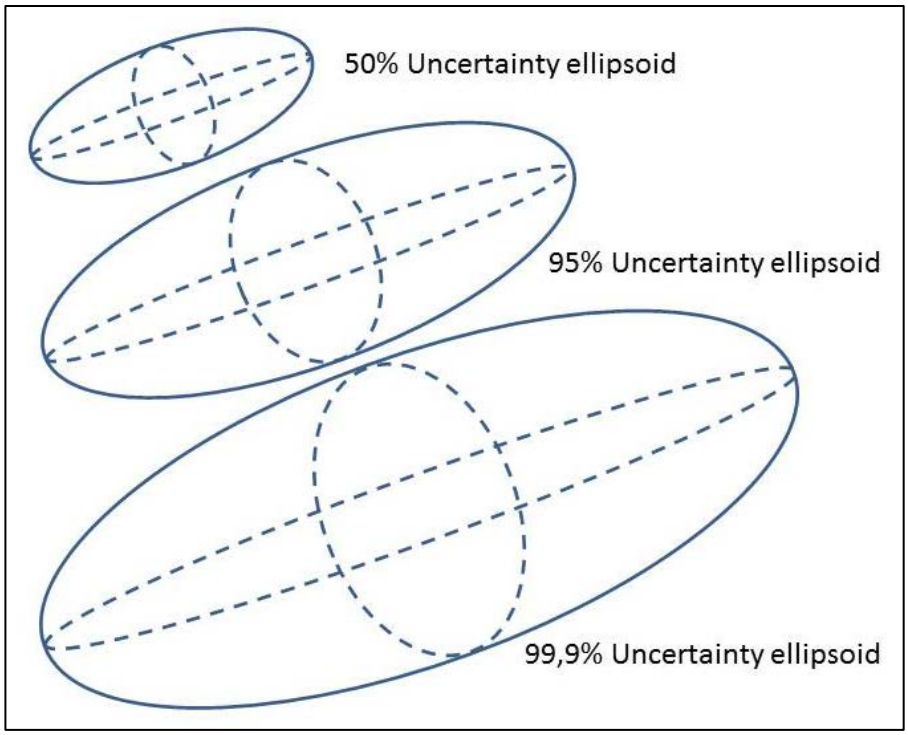

Figure 2.4: Examples on different uncertainty ellipsoids obtained from the same covariance matrix [6]

Table 2.1: Confidence level for one-, two-, and three-dimensional Gaussian distributions [2]

	One-dimensional (%)	Two-dimensional (%)	Three-dimensional (%)
1σ	68	39	20
$\sqrt{3}\sigma$	92	78	61
2σ	95	86	74
3σ	99,7	98,9	97

There is however, an issue regarding the use of confidence levels to describe position uncertainty. This issue will arise when the ellipsoid is projected into either the horizontal or vertical plane to create a two-dimensional ellipse of uncertainty or when only a single dimension is considered. Assuming first that errors can be modeled as one- two- or three-dimensional Gaussian distributions. Gaussian distributions have different relationship between confidence levels and sizes of widths, ellipses and ellipsoids. For example, a distance 3σ away from the center of a one-dimensional distribution corresponds to a confidence level of 99,7% whereas the same distance corresponds to a confidence level of 97% for a three-dimensional Gaussian distribution [2]. Thus, projection of a three-dimensional ellipsoid of a certain confidence level into the vertical plane would require an adjustment of either the ellipse size or confidence level. Wolff and de Wardt specifically argues against the use of confidence intervals for the ellipsoids in their model. What they use instead is the qualification "good" and "poor" to reflect the quality of survey equipment and procedures. Supposedly, the application of these qualifications is somewhat the same as for a confidence interval, however this is not entirely clarified.

2.5 TVD uncertainty

In order to determine the deepest and shallowest TVD, the following equation for the ellipsoid derived by Wolff and de Wardt is used:

$$\Delta\vec{r}^{T} \cdot COV^{-1} \cdot \Delta\vec{r} = 1 \qquad \textbf{Equation 2.10}$$

Where COV^{-1} represents the inverse covariance matrix and $\vec{r}$ is borehole position vector characterized by an ellipsoid having a center in $\vec{r}_0$ and dimension given by the covariance matrix. The same equation is given in another form in Equation 2.11, where the elements of the covariance matrix is denoted as h_{ij} and x, y and z is the position vector and transpose of the position vector.

$$[x \quad y \quad z] \cdot \begin{bmatrix} h_{11} & h_{12} & h_{13} \\ h_{21} & h_{22} & h_{23} \\ h_{31} & h_{32} & h_{33} \end{bmatrix}^{-1} \cdot \begin{bmatrix} x \\ y \\ z \end{bmatrix} = 1 \qquad \textbf{Equation 2.11}$$

Determining the inverse covariance matrix will in the general case yield a complicated expression. A basic derivation and expression of this is given in appendix 9.1. For simplicity the elements of the inverse covariance matrix will be denoted as H_{ij}. The covariance matrix is a symmetric matrix in which $COV = COV^{T}$. This property implies that the inverse matrix will also be symmetric. In practice this gives, $H_{12}=H_{21}$, $H_{13}=H_{31}$ and $H_{23}=H_{32}$. This property was utilized when deriving the following equation.

$$f(x,y,z) = H_{11}x^2 + H_{22}y^2 + H_{33}z^2 + 2H_{12}xy + 2H_{13}xz + 2H_{23}yz = 1 \qquad \textbf{Equation 2.12}$$

This is the general equation describing the ellipsoid, which it is possible to derive an expression yielding the deepest and shallowest TVD within the ellipsoid. To derive an expression containing only z as a variable, a set of conditions must be set. Foremost, the partial derivatives in x and y direction must be set equal to zero as given in Equation 2.13 and Equation 2.14. Consequently, the slope in x and y direction of these points is zero with a tangential plane parallel to the x, y plane with normal vector in positive or negative z direction.

$$\frac{df}{dx} = H_{11}x + H_{12}y + H_{13}z = 0 \qquad \textbf{Equation 2.13}$$

$$\frac{df}{dy} = H_{22}y + H_{12}x + H_{23}z = 0 \qquad \textbf{Equation 2.14}$$

The third equation needed to achieve a solution is given by the partial derivative in z-direction. The slope in z-direction is in the same direction as the normal vector of the plane parallel to the x, y plane with magnitude λ:

$$\frac{df}{dz} = H_{13}x + H_{23}y + H_{33}z = \lambda \qquad \textbf{Equation 2.15}$$

By solving this set of three equations, expressions for the x, y and z coordinates are given as follows:

$$\begin{cases} x = \dfrac{\lambda(H_{12}H_{23} - H_{13}H_{22})}{\Delta} \\ y = -\dfrac{\lambda(H_{11}H_{23} - H_{12}H_{13})}{\Delta} \\ z = \dfrac{\lambda(H_{11}H_{22} - H_{12}^2)}{\Delta} \end{cases} \qquad \textbf{Equation 2.16}$$

Where

$$\Delta = H_{33}(H_{11}H_{22} - H_{12}^2) - H_{11}H_{23}^2 + 2H_{12}H_{13}H_{23} - H_{13}^2H_{22} \qquad \textbf{Equation 2.17}$$

By inserting the three expressions for x, y and z in Equation 2.12, an expression for λ can be derived as follows:

$$\lambda = \pm\sqrt{\frac{H_{11}H_{22}H_{33} - H_{12}^2H_{33} - H_{11}H_{23}^2 + 2H_{12}H_{13}H_{23} - H_{13}^2H_{22}}{H_{11}H_{22} - H_{12}^2}} \qquad \textbf{Equation 2.18}$$

Due to λ having a positive and a negative value, two coordinates (x, y, z) yields from this set of equations. These are the points of interest – and necessary to reconstruct the wellbore trajectories. From the equations, it is clear that the two z values, representing maximum and minimum TVD, are of equal magnitude in opposite direction. This is reasonable to believe given the systematic nature of the error propagation.

2.6 Reconstructing well trajectories

The two most extreme trajectories in vertical depth variation are reconstructed based on the hypothesis that the trajectories positions according to the ellipsoid will be constant through a whole survey and given by the coordinates in Equation 2.16, above. These coordinates are given according to a global coordinate system (x, y, z) surrounding the ellipsoid. However in order to for the hypothesis to be valid, these coordinates must be given according to the local coordinate system (X, Y, Z) associated with the axes; a, b and c of the ellipsoid, displayed in Figure 2.5. This transformation is necessary due to the ellipsoid undergoing a three-dimensional rotation as the wellbore changes azimuth and inclination. Consequently, in order to describe the trajectories positions within the ellipsoids, their position must be given according to the ellipsoids themselves and not a surrounding global coordinate system. The coordinate X, Y, Z will furthermore be expressed by the parametric values of the ellipsoid, θ and ϕ. The value of the θ and ϕ are re-used at all the positions along the wellbore in order to reconstruct the two extreme trajectories. The magnitude of the position uncertainty will however, still increase or decrease according to the size of the ellipsoids.

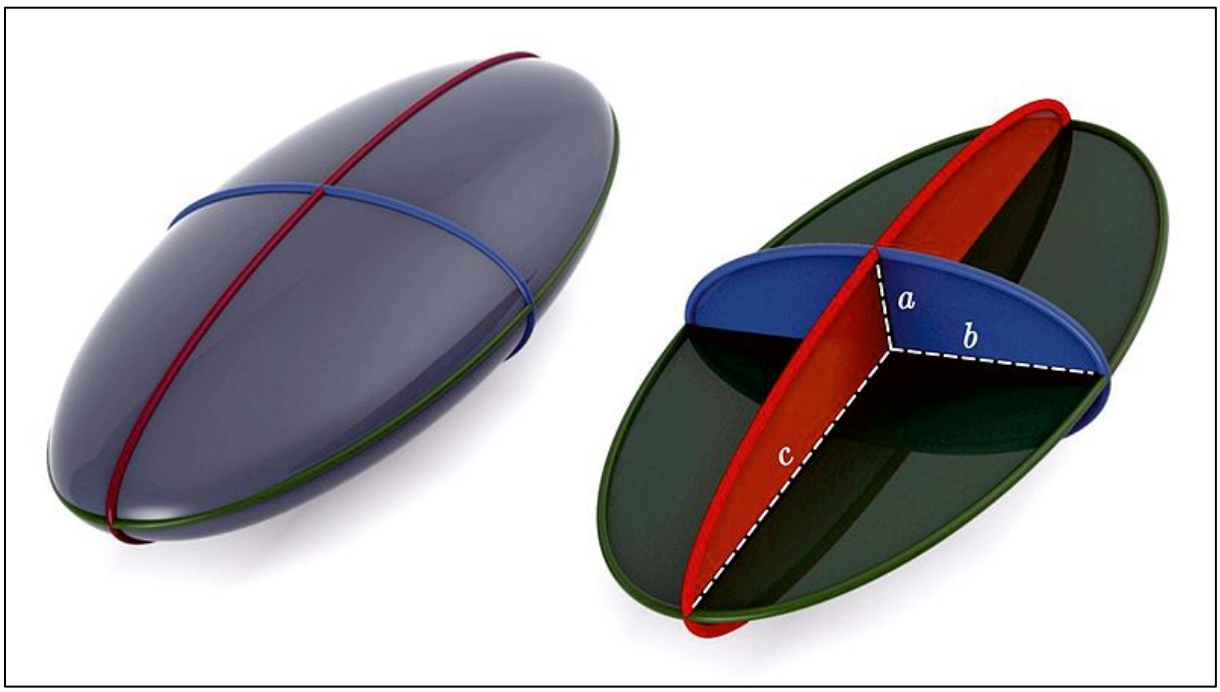

Figure 2.5: Illustration of an ellipsoid with definition of local coordinate system [12]

2.6.1 Rotation of axes in a coordinate system

A rotation of the axes in the current coordinate system for alignment with the axes of the ellipsoid is necessary to achieve the desired solution. In this section, derivation of a method to compute this rotation will be explained.

Consider first the general equation of an ellipsoid as given below. Notice the similarity between this equation and the equation for the ellipsoid of uncertainty given in Equation 2.10. The dimensions of an ellipsoid is given by its three axes a, b and c. For a tri-axial ellipsoid like the ellipsoid of uncertainty none of these axes are equal. This is in contrast to an oblate or a prolate ellipsoid in which a=b>c or a=b<c respectively. Thus, an oblate or prolate ellipsoid can be rotated around its c-axis without any effect on its orientation. This is not the case with the ellipsoid of uncertainty, therefore a three dimensional rotation of axes is necessary.

$$\left(\frac{x}{a}\right)^2 + \left(\frac{y}{b}\right)^2 + \left(\frac{z}{c}\right)^2 = 1 \qquad \textbf{Equation 2.19}$$

To describe rotation along all three axes a set of three-dimensional rotation matrices must be established. First consider a simple rotation of an x, y coordinate system as show in Figure 2.6. This displays a two-dimensional version of what will be performed with the ellipsoid. Here x and y represent the global coordinate system of the ellipsoid and x' and y' represents the local coordinate system to which we wish to align the point P. For this two dimensional case, the rotation can simply be display as a 2 x 2 matrix, given in Equation 2.20.

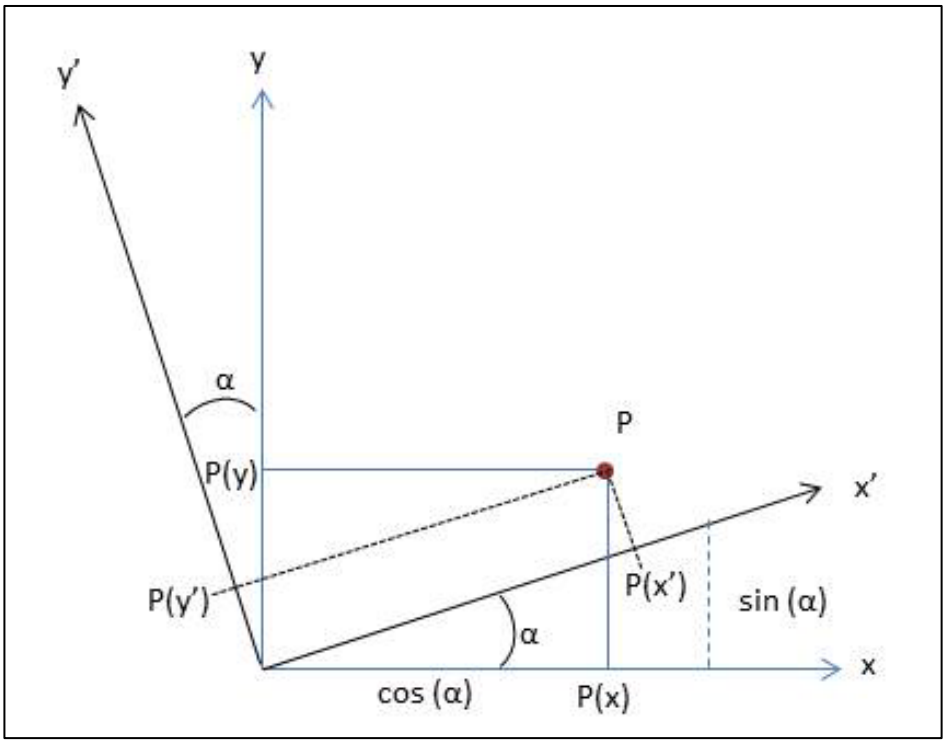

Figure 2.6: Rotation of axes in an x, y coordinate system

$$R = \begin{bmatrix} \cos\alpha & -\sin\alpha \\ \sin\alpha & \cos\alpha \end{bmatrix} \qquad \textbf{Equation 2.20}$$

For a three dimensional case, the only thing different is to keep one axis constant throughout the rotation, that is, the rotation axis. Mathematically this is done by adding a set of 0s and 1 to the 2 x 2 matrix to create a three dimensional rotation around one axis. These additional numbers are added to the matrix in the row and column that is related to the axis of rotation. The 0s will avoid any rotation of the axis and the number 1 in the center of rotation will keep the position of the axis constant throughout the rotation. The result can be seen by comparing Equation 2.20 to Equation 2.23 for the rotation around the z-axis. Similarly the matrices for rotation around the other axes are given in Equation 2.21 and Equation 2.22.

$$R_x(\beta) = \begin{bmatrix} 1 & 0 & 0 \\ 0 & \cos\beta & -\sin\beta \\ 0 & \sin\beta & \cos\beta \end{bmatrix} \qquad \textbf{Equation 2.21}$$

$$R_{y'}(\gamma) = \begin{bmatrix} \cos\gamma & 0 & \sin\gamma \\ 0 & 1 & 0 \\ -\sin\gamma & 0 & \cos\gamma \end{bmatrix}$$ **Equation 2.22**

$$R_{z''}(\alpha) = \begin{bmatrix} \cos\alpha & -\sin\alpha & 0 \\ \sin\alpha & \cos\alpha & 0 \\ 0 & 0 & 1 \end{bmatrix}$$ **Equation 2.23**

To perform a combined tri-axial rotation, these three matrices will need to be multiplied. This yields a final 3 x 3 matrix given in Equation 2.24. The order of multiplication is important when working with matrices. Any alteration of this order will give a different end result mathematically. In practice this has an implication on how the angles are defined. When performing this three-dimensional rotation there will be two intermediate coordinate systems before reaching the desired result. Angles will always be defined as rotation from the previous coordinate system. This implies that two of the three angles will be defined by the intermediate coordinate systems. As long as one is aware of this, all multiplication orders will give the same result eventually. In this case the multiplication is done according to the sequence of the matrices given.

$$R_{x,y',z''}(\beta,\gamma,\alpha) =$$

$$\begin{bmatrix} \cos\gamma\cos\alpha & -\cos\gamma\sin\alpha & \sin\gamma \\ \sin\beta\sin\gamma\cos\alpha + \cos\beta\sin\alpha & \cos\beta\cos\alpha - \sin\beta\sin\gamma\sin\alpha & -\sin\beta\cos\gamma \\ \sin\beta\sin\alpha - \cos\beta\sin\gamma\cos\alpha & \cos\beta\sin\gamma\sin\alpha + \sin\beta\cos\alpha & \cos\beta\cos\gamma \end{bmatrix}$$ **Equation 2.24**

A rotation matrix such as this is very useful. Given the correct input angles, a simple multiplication of the matrix with a vector will give the coordinates for the vector according to the new coordinate system. The transformation can also be done the opposite way by multiplying by the inverse rotation matrix. Accordingly, the desired vector X, Y, Z can be calculated by multiplying the known vector x, y, z with the rotation matrix. In order for this to be possible, the rotation matrix will need to be calculated. This can be made possible through a diagonalization of the covariance matrix as it is the covariance matrix that gives the dimensions of the ellipsoid of uncertainty.

2.6.2 Diagonalization of the covariance matrix

The eigenvalues of the covariance matrix are found by the characteristic equation given below. In which [COV] is the covariance matrix to be diagonalized, λ are the eigenvalues and I is the identity matrix. A value λ is only an eigenvalue if it satisfies this equation.

$$|[COV] - \lambda I| = 0 \qquad \textbf{Equation 2.25}$$

The result of the diagonalization will be a D and a P matrix. Where D is a diagonal 3x3 matrix with the eigenvalues along its main diagonal, all other values are zero. In practice, the eigenvalues are the dimensions of the three axes a, b and c of the ellipsoid. The P matrix is the passage matrix, also a 3x3 matrix, containing the eigenvectors. These two matrices along with the original matrix will obey by the rule as follows.

$$[COV] = PDP^{-1} \qquad \textbf{Equation 2.26}$$

The passage matrix, P, describes the orientation of the ellipsoid by its eigenvectors and can therefore be considered as equal to the rotation matrix given in Equation 2.24.

2.6.3 Calculation of coordinates within the ellipsoid

Given the findings above, the 3x3 matrix, P, can now be used to compute the desired rotation and give the position vector x, y, z by the new coordinates X, Y, Z as shown below.

$$[P] \times \begin{bmatrix} x \\ y \\ z \end{bmatrix} = \begin{bmatrix} X \\ Y \\ Z \end{bmatrix} \qquad \textbf{Equation 2.27}$$

Note that there will be no rotation of the ellipsoid or the vector itself. The vector (or point) x, y, z will only be defined according to a new coordinate system. In this case, this is the coordinate system associated with the three axes of the ellipsoid.

In order to obtain the two parameters, θ and ϕ, as mentioned introductorily, the new vector X, Y, Z will be defined by parametrical coordinates according to the ellipsoid. It should be noted that these parameters will not be identical to the azimuth and zenith angles defined in a spherical coordinate system (see Figure 2.7). The following set of equations applies for parameterization of an ellipsoid:

$$\begin{cases} X = \mathrm{a} \sin\phi \cos\theta \\ Y = b \sin\phi \sin\theta \\ Z = c \cos\phi \end{cases} \qquad \textbf{Equation 2.28 [13]}$$

Solving these will yield the desired parameters θ and ϕ as follows:

$$\begin{cases} \theta = \arctan\left(\frac{Y}{X}\frac{a}{b}\right) \\ \phi = \arccos\left(\frac{Z}{c}\right) \end{cases} \qquad \textbf{Equation 2.29}$$

Where ϕ is the zenith angle on the interval [0,π] defined from positive z-axis and θ is the azimuth angle on the interval [0,2π⟩ defined from positive x-axis. According to the hypothesis these angles can now be used to construct any matching well trajectory from the final ellipsoid and backwards or vice versa. It is important to note that even if the starting point of the trajectory is at a maximum or minimum TVD, this does not necessarily imply a trajectory at maximum or minimum TVD at the point interesting to investigate the pressure impact.

However, the objective is to discuss the impact of a worst case scenario where the pressure sensor have been calibrated to fit a wellbore actually located far away from where it is intended to be. It this case the larges impact on the pressure will be seen if the wellbore at the point of measurement is located at a maximum or minimum rather than at the point of investigation.

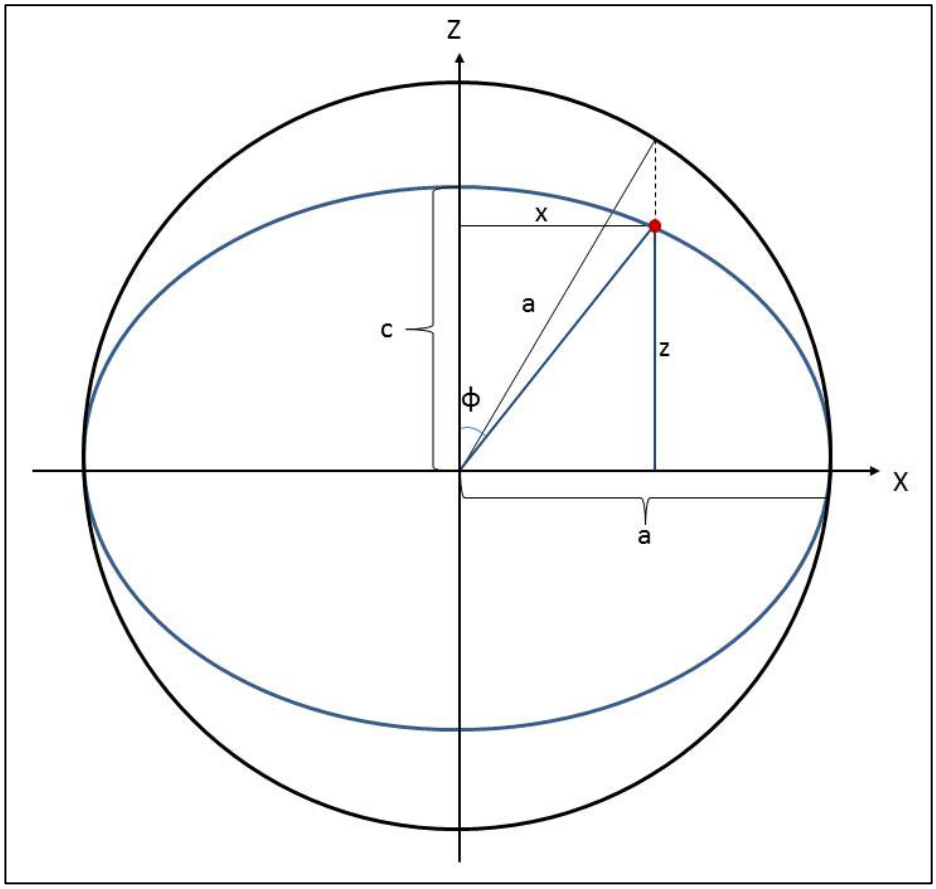

Figure 2.7: Angles on ellipse and circle

3 Analysis of factors influencing P-ρ-T properties of drilling fluid and the effect on wellbore pressure

Properties of the drilling fluid are highly significant for the downhole pressure calculations. The main parameters defining how the mud behaves is the composition of the fluid including the fraction of solid particles in suspension, the specific density and rheological properties of each component. These parameters are pressure and temperature dependent and are therefore not constant at downhole conditions, especially not at High Pressure High Temperature (HPHT) conditions. In this section factors influencing the mud properties will be discussed along with the contribution this makes to the wellbore pressure.

3.1 Temperature profile uncertainty

In the following, a qualitative analysis of the possible error sources related to downhole temperature prediction will be conducted. The object is to discuss the factors influencing the downhole temperature and enlighten the associated uncertainty.

3.1.1 Formation geothermal gradient

The formation geothermal gradient is an expression of how much the formation temperature increases with depth, expressed in degrees per unit length. A typical value for the geothermal gradient is approximately 25 – 30 °C/km. The gradient value is a result of downhole measurements and previous knowledge. In explored areas the geothermal gradient can be more or less accurately determined by well to well correlations of wells drilled in corresponding formations. However, in developing and less explored areas the geothermal gradient will have to be measured by MWD tools when drilling and will in such cases be considered a larger source of uncertainty.

3.1.2 Downhole heat transfer

Downhole heat transfer is a complicated issue due to the large number of contributing variable including: temperature, pressure, viscosity of fluids, and composition of materials, density, thermal conductivity, specific heat capacity and flow rate. Temperature can have large effect on downhole pressure, especially by thermal expansion of the drilling mud. This will cause uncertainty in the mud density which is directly linked to the hydrostatic pressure. In addition, heat exposure will also change other properties of the mud which not only affects the downhole pressure but also alter the conditions for heat transfer itself, making the issue even more complicated.

There are numerous heat transfer mechanisms in a wellbore. Heat is transferred from the formation to the annulus mud in an open hole section, from warmer annulus mud to colder mud in the drill pipe through the steel walls of the pipe, from formation to annulus mud through casing and cement for cased hole sections and from warmer mud downhole to colder mud further up. Heat transfer mechanisms through different mediums will have an effect on the temperature in wellbore and also the uncertainty. In the following some of the most important aspects of heat transfer will be discussed.

3.1.3 Specific heat capacity

Specific heat capacity is a measure of a substance ability to store heat. For a multicomponent system the specific heat capacity is the weighted average in terms of mass fractions of the specific heat capacity of each component as given in Equation 3.1.

$$C_p^m = \sum_{i \in \Omega} \varepsilon_i C_p^i , \qquad \varepsilon_i = \frac{f_i \rho_i}{\rho_m}$$

Equation 3.1 [14]

Where C_p^m is the specific is heat capacity of the mixture, ε_i and C_p^i are the mass fractions and specific heat capacity of the different components and Ω is a set of indices representing each component. For a mud mixture these indices would be: w for water or brine, o for oil, lgs for low gravity solids, hgs for high gravity solids and c for cuttings.

Consequently, in order to precisely determine the specific heat capacity of a mud mixture it is important to accurately determine the mass fraction of each component. This is a difficult task due to the constantly changing variables of a mud mixture at downhole conditions. The fraction of each component may vary with depth and time due to lost circulation, influxes, changing ROP and cutting bed formation and erosion. The specific density of non-solid components will also vary with temperature and pressure. Higher temperature will cause thermal expansion and thereby lower density. Higher pressure will cause compression and thereby higher densities. As the rate of compressibility is different for all the components, the composition of fluids and solids in a control volume will change, affecting the mass fractions. This effect is further explained in section 3.2.2. The specific heat capacity of each component is additionally pressure and temperature dependent.

The impact of the suspended cuttings on the heat capacity of the mud is important to consider. At low cutting concentration it is reasonable to assume the impact on heat capacity and thereby temperature to be relatively small and possible negligible. However, at lager concentration the impact can no longer be considered insignificant. Lager concentrations of cuttings in suspension will impact the mud density and thereby complicate determining mass fractions. With larger cutting concentration it is also important to determine the specific heat capacity and the effect on the overall heat capacity of the mud. The specific heat capacity of the cutting particles is depending on the mineral composition, density, porosity and the pore fluids stored within. Both specific heat capacity and density of the pore fluids are pressure and temperature dependent. Given the variation in compressibility for different pore fluids, saturation values may also change.

Thus, to determine the specific heat capacity of a multicomponent system is a very complicated issue when all input values are associated with uncertainty. Together with aspect of variables depending on each other, this will give reason to assume uncertainties in the wellbore temperature.

3.1.4 Thermal conductivity

Thermal conductivity is a measure of a substance ability to transfer heat. Heat transfer from one medium to another is depending on the thermal properties of the mediums through which heat is transferred. As previously indicated the downhole heat transfer mechanisms are very complicated and the thermal conductivity of multicomponent systems are no different. The first solution to calculation of effective thermal conductivity of a suspension of solid particles in a homogeneous medium was derived by Maxwell based on assumptions of spherical particles of low concentrations. None of these assumptions is particularly accurate when considering weighted drilling mud, especially not the latter. This equation has later been modified to be more accurate for higher concentration of particles, however still considering non-touching, spherical particles [15]. The resulting equation is given below for illustrational purposes:

$$k_m = k_l \frac{\frac{2+\lambda}{1-\lambda} - 2f_s + 0{,}409\frac{6+3\lambda}{4+3\lambda}{f_s}^{7/3} - 2{,}133\frac{3-3\lambda}{4+3\lambda}{f_s}^{10/3}}{\frac{2+\lambda}{1-\lambda} + f_s + 0{,}409\frac{6+3\lambda}{4+3\lambda}{f_s}^{7/3} - 0{,}906\frac{3-3\lambda}{4+3\lambda}{f_s}^{10/3}} \qquad \textbf{Equation 3.2 [14]}$$

Where f_s is the fraction of solid particles in suspension and $\lambda = \frac{k_s}{k_l}$, solid to liquid thermal conductivity ratio. Obviously the geometry of mud additives and cutting particles are not spherical, however, mathematically this is believed to be the most accurate description. The assumption of non-touching particles is in practice wrong, however, the effect on overall thermal conductivity is unknown. What does affect the thermal conductivity of mud is the fraction of solid particles, consisting of weighting additives, cuttings, swarf etc. The fraction of solid particles can be roughly calculated and samples from the return mud can be taken. However, at downhole condition the situation is different. The liquid phase of the mud will expand or be compressed depending on whether the temperature or pressure is dominating. The solid phase is usually assumed to be incompressible, however Islambourg et al. [16] argues that this could not be correct due to their findings of larger deviation between measured and calculated values than the uncertainty of the measurements.

The composition of the solid particles in suspension impacts the thermal conductivity. There are large variances depending on the mineralogical composition of the cutting particles.

Quartz has a thermal conductivity of 7-11 W/m·K while feldspar has a thermal conductivity of approximately 2 W/m·K [15]. The volume and composition of pore fluids will also have an impact. Thermal conductivity will additionally vary with temperature.

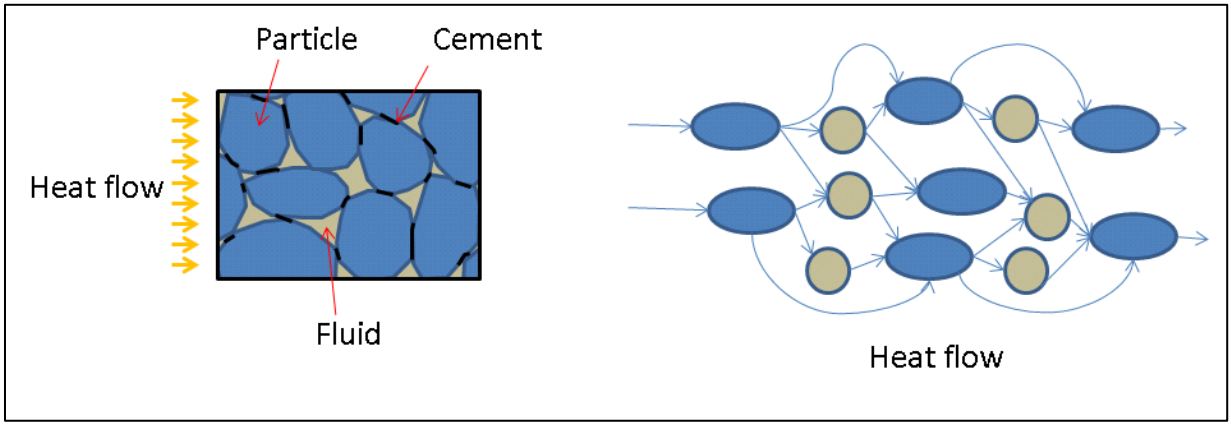

Figure 3.1: Schematic illustration of heat flow through a wetted porous medium [15]

Thermal conductivity through a wetted porous media is illustrated in Figure 3.1. Heat is transferred both within the rock matrix and from the matrix to the pore fluids and vice versa. As previously discussed, heat transfer is depending on the mineralogical composition, pore fluids and saturation, grain size. The thermal conductivity through a porous rock matrix may also depend on the layering structure and the orientation of heat transfer. If the rock matrix is composed of layers with different mineralogy it is usual to define thermal conductivity in two components; one parallel to the layers, $k_{\parallel}$, and one perpendicular to the layers, $k_{\perp}$. An estimate of the effective thermal conductivity for a layered formation was given by Robertson [17] as the average of the parallel and perpendicular component. Robertson also discusses how thermal conductivity will vary with pressure. These effects will vary depending on the mineral composition. Dense rocks will have a linear relationship with pressure while porous rock will not. The effect is also strongly depending on the compressibility of the rock matrix and properties of the pore fluids.

3.1.5 Effects of uncertainty in thermal conductivity and specific heat capacity on wellbore temperature

Based on the discussion in the previous sections it is conceivable to assume uncertainties in thermal conductivity and specific heat capacity of both the fluids in the well and the formation. Quantifying these into accurate temperature- and eventually pressure uncertainties is a very difficult task. This is due to the number of influencing variables and how many of the variables to some degree depend on each other. In an attempt to analyze how the mud temperature depends on the specific heat capacity and the thermal conductivity of the formation, Toft [18] simulated the flow of different mud types in formations with different geothermal properties over a period of time. The objective was to monitor the inlet and outlet temperature in the well for the different configurations to investigate how large variation in temperature it is reasonable to expect. The results show the largest temperature deviations with OBM at high flow rates and WBM at low flow rates as seen in Figure 3.2 and Figure 3.3. From flow of OMB, a temperature deviation of 2,4°C was recorded after 6,5 hours, between flow with formation specific heat capacity and thermal conductivity of respectively: 900 J/kg·K, 1.40W/m·K and 1500J/kg·K, 3,00 W/m·K. For a similar configuration with lower flow rate, the results shows a 3,10°C temperature deviation for water based mud. Similar simulations show decreasing temperature deviations in WBM with increasing flow rates and the opposite for OBM. The temperature deviations experienced here are relatively small given the large variation in input parameter. However these simulations are performed in a relatively shallow well, with a TVD of 2500 m and an openhole section of only 195 m. In addition, only the thermal conductivity and specific heat capacity of the formation is varied, along with the flow rate. Uncertainties in the fluid properties are not considered.

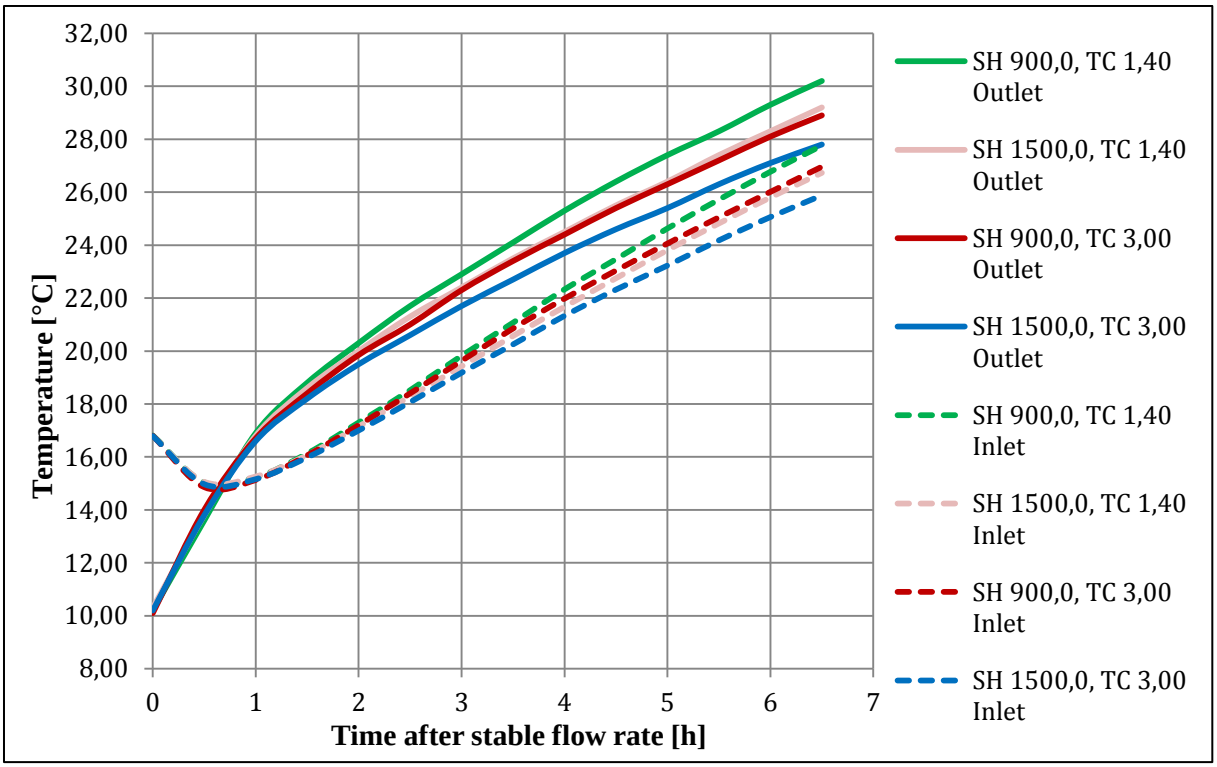

Figure 3.2: Inlet and outlet temperatures from 2520 l/min circulation with OBM [18]

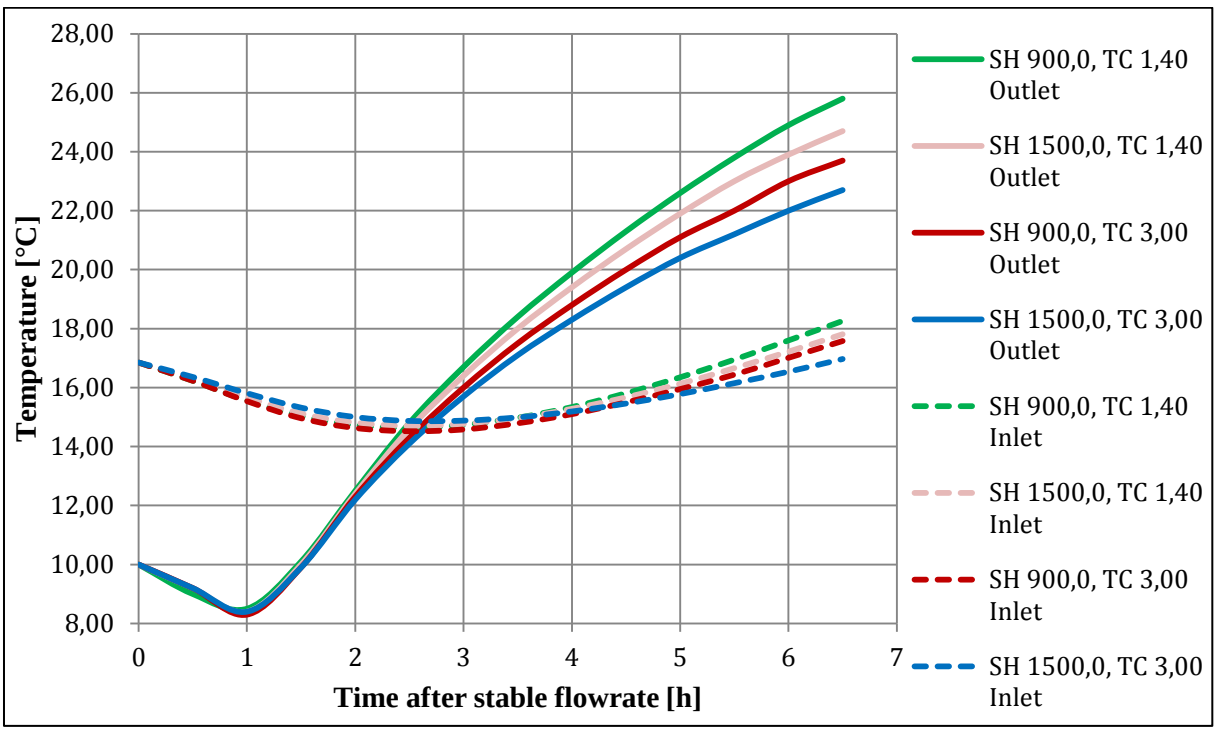

Figure 3.3: Inlet and outlet temperatures from 526 l/min circulation with WBM [18]

3.1.6 Hydraulic and mechanical friction

Heat generated from hydraulic and mechanical friction in annulus will effect on the mud temperature. Hydraulic friction is generated from pressure loss through drill pipe, bit nozzles and annulus. The magnitude of the effect of hydraulic friction on downhole temperature depends on the pump rate. At higher pump rates the frictional pressure loss is greater and therefore also the heat generation.

Mechanical friction through torque and drag of the drill string against formation and casings is also a significant source of heat generation. The significance will increase with the length and complexity of the wellbore as the contact surface increases. A study by Kumar et al [19] illustrates the concerns of frictional heating of annular fluids and drill pipe in ERD wells. The study uses a basic mathematical model to study heat transfer not considering all the important aspect discussed in section 3.1.3 and 3.1.4. The accuracy of any specific finding is therefore debatable. However, the study concludes that the maximum annular temperature will occur some distance above the bottomhole. This implies that the maximum temperature may occur above the temperature sensor of the BHA and thereby be a significant source of uncertainty in the annular temperature profile.

3.2 Fraction of solid particles in drilling fluid

Solid particles such as weighting additives, LCM etc. will account for a large fraction of the mud density if the liquid phase is not a solution of salts (brine). The solid fraction will increase with increasing mud weight as more additive is required. The solids can be divided into high gravity solids (hgs) and low gravity solids (lgs). Solid fractions at surface conditions can easily be determined to an adequate level, however at downhole condition the situation is different. The liquid phase of the mud will expand or be compressed which changes the composition within the control volume and thereby changes the solid fraction, this is illustrated in Figure 3.4. In addition there will be presence of large quantities of cuttings.

3.2.1 Cuttings transport model

Cutting transportation is known to have significant impact on the mud density and rheological parameters. Various attempts have been made to develop adequate cutting transport models to ensure good hole cleaning and reduce drilling problems such as stuck pipe and enhanced torque and drag, possibly resulting in NPT or abandonment. Several of these models are summarized by Pilehvari et al. [20]. Developing an adequate cutting transport model has proven to be difficult since cutting transportation is influenced by a number of parameters including: well geometry, fluid density, rheology, ROP, RPM, flow patterns, flow rates and cuttings size [15]. Transient flow phenomena should also be considered, applying an unlikely situation of steady-state flow in the wellbore could generate false results. Knowledge of cuttings transportation in the well is crucial for the ability to determine the impact on density and other parameters. Important factors to determine are the volume fraction of cuttings in suspension at a given time and the movement of the cutting particles out of the well.

A cutting particle in suspension is subjected to several forces; gravity, buoyancy and frictional. The frictional forces are composed of drag and lift forces [21]. Gravitational- and buoyancy forces results from the density of the drilling fluid and density and volume of the cutting particle. As the buoyance force does not overcome the gravitational force cutting particles rely on a sufficient frictional force to be transported out of the well. The frictional force relies on the rheological properties of the mud and a certain velocity to allow for cuttings transportation. This velocity is often referred to as the critical velocity [21]. If the local velocity around the cutting particles does not exceed the critical velocity, particles will

drop out of suspension. When this occurs, cutting particles will accumulate and form a cuttings bed. At low flow velocities this cuttings bed may grow to reach a substantial size until the flow area is reduced to a degree where the flow velocity exceeds the critical velocity. Cuttings particles will then go back into suspension [15]. When this phenomenon occurs it enhances the difficulty of determining the fraction of cuttings particles in suspension. In addition, rolling mechanisms of cutting particles in inclined wellbores can be experienced [21], stretching the cuttings bed formations and prolonging buildup to a degree where particles go back into suspension.

An interesting point to be made is that concentration of cuttings is not uniform along the wellbore. A non-uniform distribution will account for local variations is density and rheology. The reason for this non-uniform distribution is partly due to cuttings going into, and out of suspension and partly due to the movement of cuttings out of the well. The rate a cutting particle will flow out of the well is depending on the local velocity profile in the well and the slip velocity between the cutting particle and drilling fluid. Combined effects of fluid flow, drill pipe rotation and drill string axial movement creates complex velocity fields [15]. Drag and lift forces applied to a cutting particle is therefore different at near proximity to the borehole wall, drill pipe or any other solid boundary. This is simply because the velocity profile is different compared to the middle of the flow. A non-uniform velocity field will also have other side effects as the cutting particle may start to spin on itself. Rotation of particles will change the drag and lift forces applied to it and so forth alter its movement in the wellbore. Other events may also induce a rotation such as a shock against the wall or other particles. An asymmetric particle may even start to spin in a uniform velocity field. [15]

3.2.2 Solid fraction as a function of pressure and temperature

The fraction of solid particles in a control volume will change as the fluid in the control volume undergoes an expansion or compression as displayed in Figure 3.4. The expansion or compression of fluids in a control volume is a function of the local temperature and pressure and the PVT properties of fluid present. The following equation for estimating volume fraction of cuttings as a function of pressure and temperature was derived by Cayeux [14]:

$$f_c(p,T) = \frac{f_c^0 \rho_m(p,T)}{(1-f_c^0)\rho_m^0 + f_c^0 \rho_m(p,T)} \qquad \textbf{Equation 3.3}$$

Where $f_c(p,T)$ and $\rho_m(p,T)$ represents the fraction of cuttings and the mud density at a given pressure and temperature, f_c^0 and ρ_m^0 is the initial volume fraction and mud density. A general formula, such as this, gives an indication and a fairly good estimate on how the changes in a control volume will affect the volume fraction of cuttings. The issue is related to the input parameters. From previous sections it is clear that the temperature in the wellbore is quite uncertain and constantly changing both with time and depth, similarly for the pressure. Thus, local mud density as a function of temperature and pressure will also vary in addition to the possibility of formation influxes. Compressibility of oil and water is low compared to gas. Any presence of gas in the drilling fluid will therefor cause relatively large changes to the overall compressibility, at least locally. From discussion of the cutting transportation model it is also reasonable to assume the initial volume fraction of cutting to be uncertain and not uniformly distributed along the wellbore.

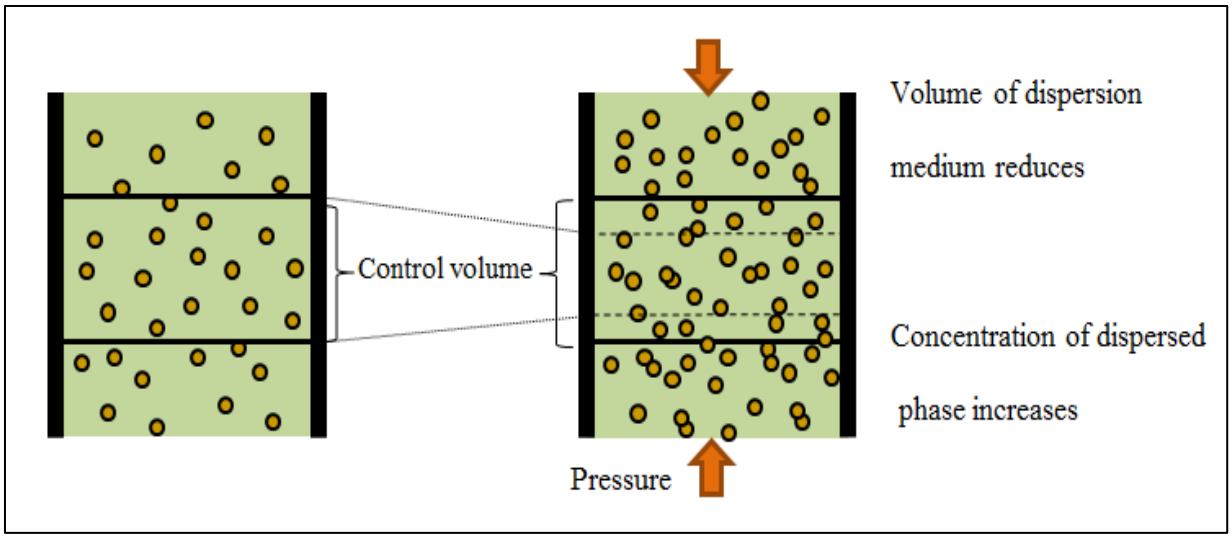

Figure 3.4: Effect of compression on solids fraction in mud [15]

Uncertainties in the volume fraction of solid particles in the wellbore are reasonable to assume and this will affect the uncertainty in the drilling fluid density. However the impact by compression or expansion of the liquid phase can be debated. Presumably thermal expansion caused by high downhole temperatures and compression caused by high pressures will to some degree compensate each other. Combining this with the relatively low compressibility of both oil and water would raise the question if this is in anyway significant. Nevertheless it adds a contribution to the cumulative uncertainty in the drilling fluid parameter which as a whole will have significance on the outcome.

3.3 Presence of gas in drilling fluid

Influxes of any formation fluid will contribute to the change of rheological properties and density of the drilling fluid. Of these, influx of gas will give the most drastic results as gases have highly different properties compared to oil and water. Gas influxes can occur at any time during the drilling operation. Probability of influxes will increase as the well pressure approaches the pore pressure gradient and are especially likely when conducting MPD operations. However it is important to note that gas also can enter the wellbore by being present as a pore fluid in cutting particles etc. It is therefore not necessary to have an influx for gas to be present in the drilling fluid.

When gas enters the wellbore it can either exist as a separate dispersed phase flowing with a slip velocity in relation to the drilling fluid (as would be the case in WBM), or be dissolved in the drilling fluid (if this is an OBM or SBM). In order to quantify the effects, the fraction of gas present in the drilling fluid is essential to determine. An expression for the gas fraction in drilling fluid was derived by Cayeux [14] as follows:

$$f_g(p,T) = \frac{\rho_g^0 f_g^0}{\rho_g^0 f_g^0 + \frac{\rho_g(p,T)}{\rho_m(p,T)}\rho_m^0(1-f_g^0)} \qquad \textbf{Equation 3.4}$$

Where $f_g(p,T)$, $\rho_m(p,T)$ and $\rho_g(p,T)$ are the volume fraction of gas, mud density and gas density at a given temperature and pressure, f_g^0, ρ_m^0 and ρ_g^0 are the initial volume fraction of gas, mud density and gas density at temperature and pressure; T^0 and p^0.

Gas density at a given temperature and pressure can be determined by re-writing the real gas law:

$$\rho_g(p,T) = \frac{pM}{Z(p,T)RT} \qquad \textbf{Equation 3.5}$$

Where M is the molecular weight of the gas, Z is the compressibility factor and R is Avogadro's number, R = 8,314462175 J/mol·K. Compressibility values for gases are

tabulated and can also by calculated solving the generalizing compressibility equation as given by Rao. [22]

The difficulty of determining the volume fraction is obvious, especially in the event that a gas influx completely dissolves in an OBM or SBM. In this case the influx could go undetected until it boils out in the riser or at surface. If the gas is dispersed in a WBM the situation can be viewed similarly as is Figure 3.4. The liquid surrounding the dispersed bubbles will be compressed altering the volume fraction. In this case the gas bubbles will also be compressed, hence the term; $\rho_g(p,T)$. One must also consider the event of gas boiling out and entering the two-phase envelope. The likelihood of this occurring depends on the composition of the gas. A gas composition with high boiling temperature and pressure may start to condensate as it moves up the wellbore whereas pure alkanes such as methane, ethane, propane etc. are dry gases and will therefore not condensate.

3.4 Effects on drilling fluid density

Density of the mud in the wellbore is directly linked to wellbore pressure and is therefore highly relevant in this analysis. Significant deviation between the mud density measured at surface conditions and downhole conditions can be expected. Density of drilling fluid is depending on a number of variables discussed in the previous sections. The effect of these variables on the uncertainty in drilling fluid density will be discussed in the following.

Density of the drilling fluid can be described as the sum of the density and fraction of the individual components:

$$\rho_m(p,T) = \sum_{i\epsilon\Omega} f_i \rho_i(p,T) \qquad \textbf{Equation 3.6 [14]}$$

Where f_i and $\rho_i(p,T)$ represents the fraction and density of the individual components, Ω is the set of indices for the individual components including; w (water), o (oil), g (gas), lgs (low gravity solids), hgs (high gravity solids) and c (cuttings). This relationship is only valid if it satisfies:

$$\sum_{i\epsilon\Omega} f_i = 1 \qquad \textbf{Equation 3.7 [14]}$$

At first sight this equations seems relatively simple and manageable, but it is clear that also the volume fractions, f_i , should also be given as a function of pressure and temperature: $f_i(p,T)$. If the drilling fluid is an emulsion the water/oil ratio should also be considered as a function of temperature and pressure. An emulsion is a mixture of two (or more) immiscible fluids. Water and oil are both considered compressible, but not necessarily at the same rate, changes in the water/oil ratio will therefore be experienced. A general equation considering these effects was derived by Cayeux [23]:

$$\rho_m(p,T) = f_c(p,T)\rho_c + \left(1 - f_c(p,T)\right)\Big[f_g(p,T)\rho_g(p,T) + \left(1 - f_g(p,T)\right)\Big(f_s(p,T)\left(\frac{\Lambda}{1+\Lambda}\rho_{lgs} + \frac{1}{1+\Lambda}\rho_{hgs}\right) + \left(1 - f_s(p,T)\right)\left(\frac{K(p,T)}{1+K(p,T)}\rho_o(p,T) + \frac{1}{1+K(p,T)}\rho_w(p,T)\right)\Big)\Big]$$

Equation 3.8 [14]

Where Λ is the volumetric ratio between low gravity solids and high gravity solids and $K(p,T)$ is the oil/water ratio at pressure p and temperature T:

$$K(p,T) = K^1 \frac{\rho_o^1 \rho_w(p,T)}{\rho_w^1 \rho_o(p,T)}$$

Equation 3.9 [14]

Where K^1, ρ_o^1 and ρ_w^1 are the oil/water ratio, oil density and water density at initial conditions.

From the complexity of Equation 3.8, the issue of accurately determining the drilling fluid density at downhole conditions is displayed. Theoretically, the accuracy of the equation will increase as the number of parameters considered increases. However as discussed in this chapter, there are substantial uncertainties in many of these parameters. All of these parameters except the density of high- and low gravity solids and the ratio between them will vary with temperature and pressure. A temperature and pressure that has proven very difficult to determine accurately and will therefore be the underlying cause of most of these uncertainty along with the uncertainty in the fraction of cuttings in well and distribution of these.

Presence of gas does affect the density, however the effects are mostly significant at lower wellbore pressure. Figure 3.5 illustrates the density effects by adding 100 ppm of gas to the drilling fluid in a variety of temperatures and pressure. At high pressures the gas will be compressed to a degree where the density effects appear to be insignificant. Decreasing pressure will allow the gas to expand and even a small quantity of 100ppm will distinctively alter the density.

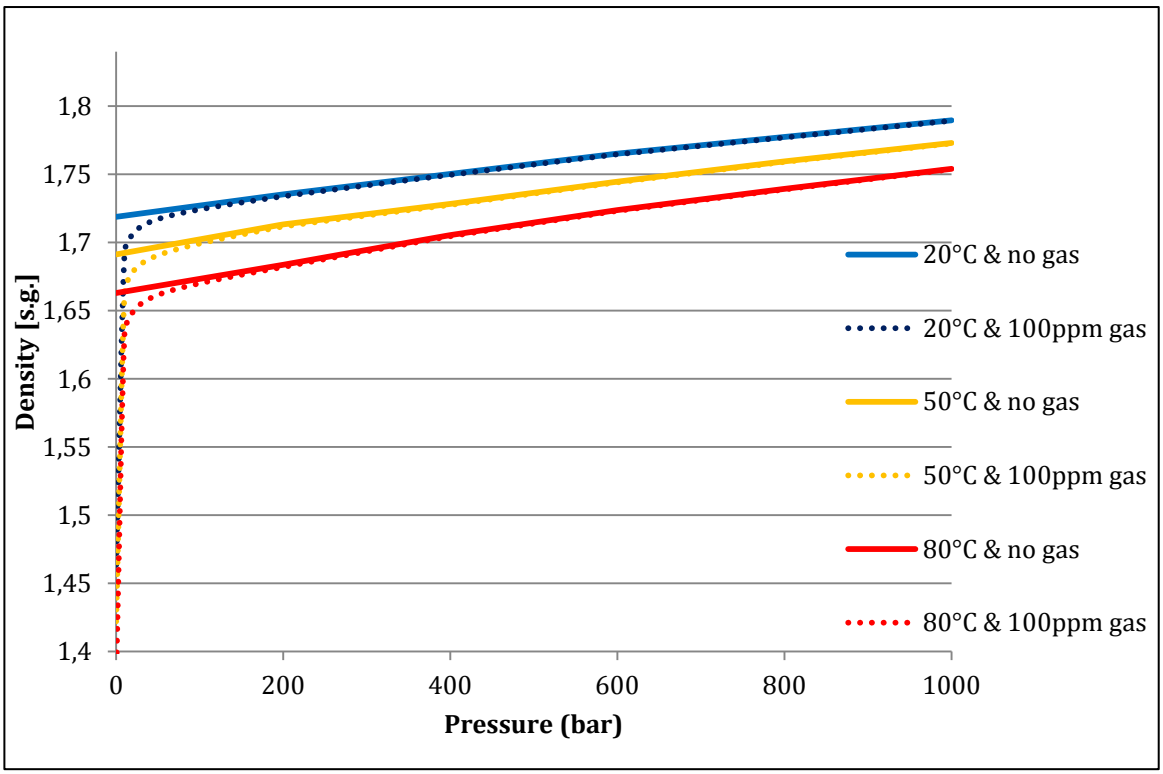

Figure 3.5: Effect of 100ppm in mass of gas on drilling fluid density at various temperatures and pressures. [24]

3.5 Effects on rheological parameters

Rheological parameters of the drilling fluid are crucial to the drillings operation and parameters will also affect the wellbore pressures. One of the parameters that will have largest effect on the wellbore pressure when circulating is the viscosity of the drilling fluid. The viscosity is defined by the shear stress and shear rate of the fluid and it is directly linked to the annulus friction factor determining the frictional pressure loss. Viscosity is also linked to surge and swab pressures as it will determine the fluids resistance to flow. Cuttings transportation will also be influenced by the fluid viscosity as frictional forces between the cuttings and the fluid. Other parameters such as gel strength will also influence the pressure. High gel strength will allow cuttings to stay suspended without circulation for a longer period of time, but will cause higher pressure spikes when the pump starts.

3.5.1 Rheology models

Many models have been proposed on how to relate shear rate and shear stress of a drilling fluid. Newtonian fluid rheology models cannot be considered for drilling fluids as they are shear thinning fluids with a yield stress [15]. In practice this means that the viscosity of the fluid will decrease as it is exposed to higher shear stresses. The shear stress (τ) can be defined as the force per unit area required to sustain a constant fluid movement. Shear rate ($\dot{\gamma}$) is considered as the rate of change in velocity at which one layer of fluid passes over an adjacent layer. For Newtonian fluid the viscosity is considered independent of shear stress. Typical rheology models used to describe the behavior of drilling fluids are given below.

The Bingham model is given as follows, where τ_y is the yield stress and μ_p is the plastic viscosity of the fluid:

$$\tau = \tau_y + \mu_p \dot{\gamma} \qquad \textbf{Equation 3.10 [25]}$$

In order to measure plastic viscosity and yield stress, 600 and 300 rpm dial readings are used from a fan viscometer. The rheological parameters of Bingham fluids can be determined be using the following equations [26]:

$$\mu_p = \theta_{600} - \theta_{300}\ [cP] \quad \textbf{Equation 3.11}$$

$$\tau_y = \theta_{300} - \mu_p\ [lb/100ft^2] \quad \textbf{Equation 3.12}$$

The Bingham model is seldom suitable for describing drilling fluids as it considers a linear relationship after initial yield. Additionally, no explicit relationship between shear stress and volumetric flow rate can be derived from this expression [27].

The power law model describes a fluid with no yield stress and a constant ratio between the logarithms of shear rate and shear stress.:

$$\tau = K\dot{\gamma}^n \quad \textbf{Equation 3.13}$$

Where K is the consistency index and n is the flow behavior index. K and n can be determined graphically or by use of the following equations [26]:

$$n = 3.321\log\left(\frac{R_{600}}{R_{300}}\right) \quad \textbf{Equation 3.14}$$

$$K = 1.067\frac{R_{300}}{511^n}\ [\ lb/100ft^2] \quad \textbf{Equation 3.15}$$

Simple explicit relationships between the shear rate and volumetric flow rate can be derived from this expression, however the model often does not fit actual data for drilling fluids [27] .

The Herschel and Bulkley [28] model combines the characteristics of the Bingham and the power law model to address fluids exhibiting both a non-linear relationship as well as a yield stress (τ_0):

$$\tau = \tau_0 + K\dot{\gamma}^n \quad \textbf{Equation 3.16}$$

The n and K values can be determined graphically. Since this is a three-parameter model, an initial calculation of τ_0 is required for other parameter calculations:

$$\tau_0 = \frac{\overline{\tau} - \tau_{min}\tau_{max}}{2\overline{\tau} - \tau_{min} - \tau_{max}}$$ **Equation 3.17 [29]**

Where $\overline{\tau}$ is calculated by plotting shear rates corresponding to several shear stresses. The mean of the shear stress is the value corresponding to the geometric mean of the shear rates as given below:

$$\overline{\gamma} = \sqrt{\gamma_{min}\gamma_{max}}$$ **Equation 3.18 [29]**

A later model derived by Robertson and Stiff [27] is said to give a more precise relationship between shear rate and shear stress for most drilling fluids:

$$\tau = A(\dot{\gamma} + C)^B$$ **Equation 3.19**

The A and B can be considered similar to the parameters of the power law model. The term $(\dot{\gamma} + C)$ may be considered as the "effective shear rate" or the shear rate that would be required for a power law fluid to produce the same shear stress [27]. These coefficients enable the model to describe yield - pseudo plastic fluids such as drilling fluid in addition to the analytical properties of a power law model. Consequently, if B=1 and C=0, the model will describe a Newtonian fluid. Likewise if B=1 and C≠0 the fluid is a Bingham plastic fluid and with B≠1 and C=0 the fluid can be characterized to follow the power law model. [27]

Parameters are evaluated by plotting the shear stress corresponding to several shear rates. The geometric mean of the shear stress is calculated as:

$$\overline{\tau} = \sqrt{\tau_{min}\tau_{max}}$$ **Equation 3.20 [27]**

The corresponding value of $\dot{\gamma}$ is red from the plot and used in the following equation to calculate C:

$$C = \frac{\dot{\gamma}_{min}\dot{\gamma}_{max} - \overline{\dot{\gamma}}^2}{2\overline{\dot{\gamma}} - \dot{\gamma}_{min} - \dot{\gamma}_{max}}$$ **Equation 3.21 [27]**

3.5.2 Influence by temperature and pressure

Rheology of any fluid is temperature dependent [15] and analysis shows that mud viscosity, at any given temperature, increases exponentially with increasing pressure [30]. In the graphs given below some examples of HPHT rheology for typical OBMs used in the North Sea is given. Figure 3.6 shows how low viscosity OBM with density of 1.52 s.g. has large variations in shear stress as the temperature changes. However any pressure increase between 1 and 300 bars seems to have very little effect, regardless of the temperature. Figure 3.7 shows quite different results for high viscosity OBM with density of 1.72 s.g. Even though temperature variations seem to be dominant also here, pressure variations make a significant impact. The magnitude of the impact caused by pressure variations is additionally clearly depending on the temperature. Pressure increases between 1 and 150 bars causes only small variations at 20°C whereas at 50°C and 80°C, the variations are more distinctive.

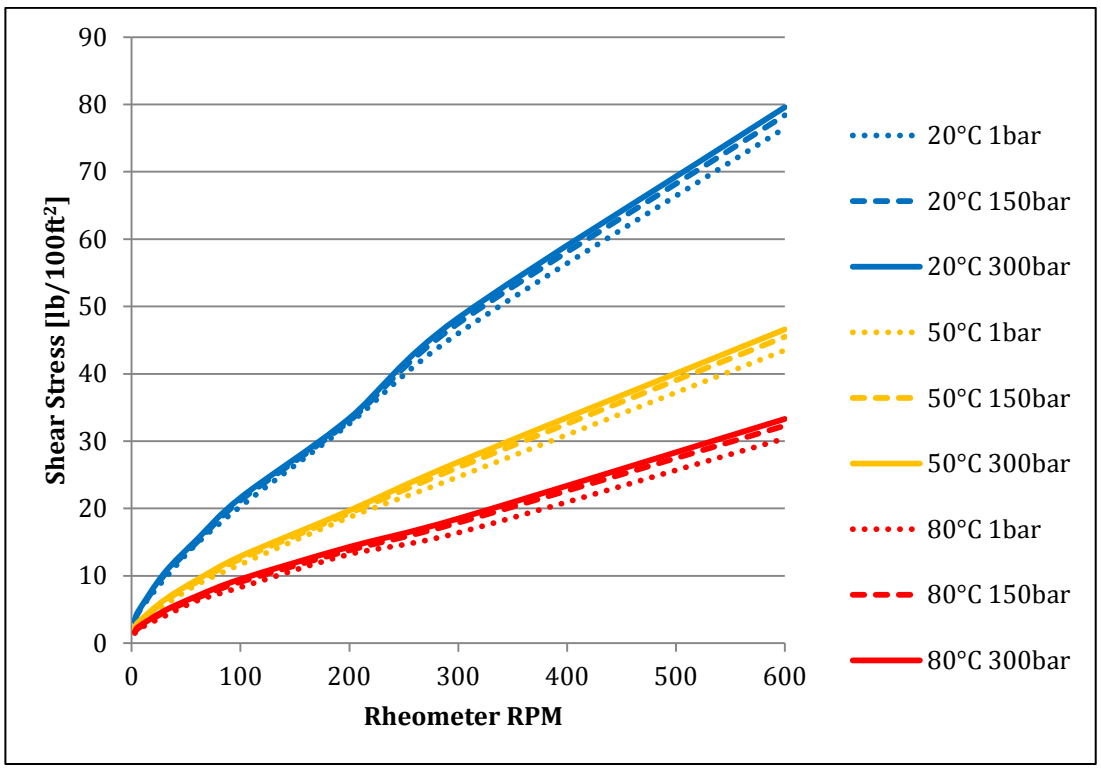

Figure 3.6: Rheology of 1.52 s.g. low viscosity OBM at different temperatures and pressures [31]

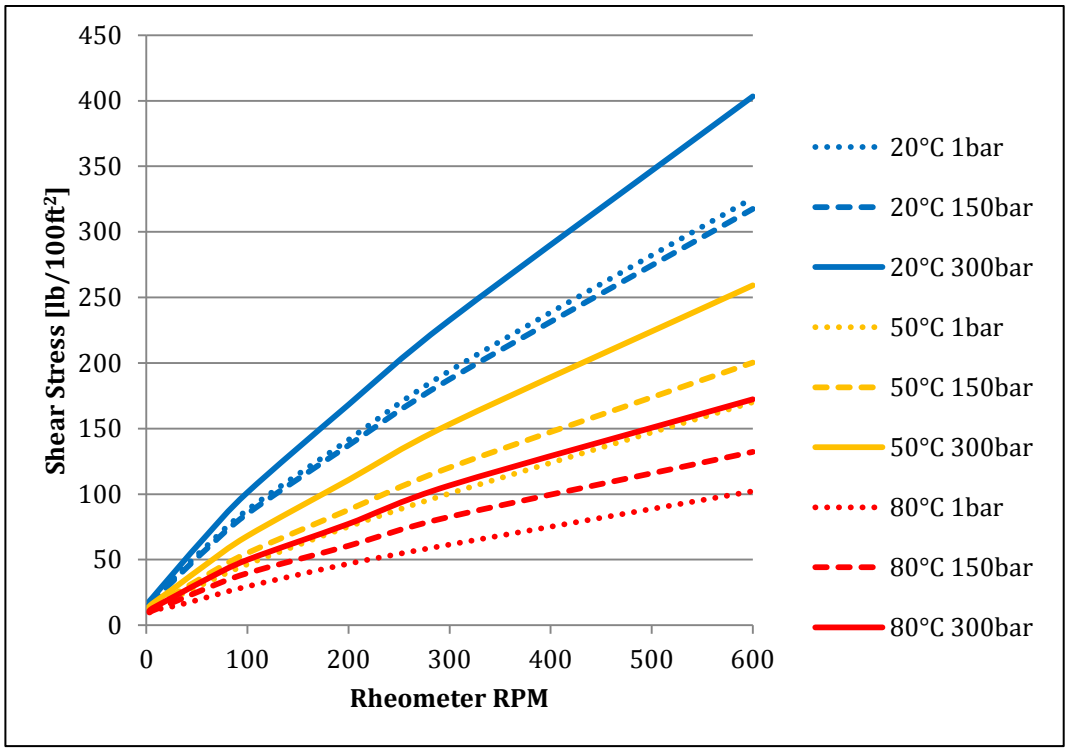

Figure 3.7: Rheology of 1.72 s.g. high viscosity OBM at different temperatures and pressures [31]

3.5.3 Solid particles suspended in a fluid

Rheological parameters are known to change as solid particles are added to a solution. This effect was first studied a century ago by Albert Einstein [32]. The early models involved the effects of adding solid particles to a Newtonian solution. The approach of a Newtonian solution is not adequate for modeling a drilling fluid. In addition, the model by Einstein is limited to with respect to particle concentration making it unrealistic for drilling fluids containing solid additives and cuttings. A modification of Einstein's law was presented by Hastcheck [33] given the possibility to consider the whole spectrum of particle concentration:

$$\mu_m^c(p,T) = \mu_m(p,T)\big(1 + 4{,}5 f_c(p,T)\big), \qquad f_c \epsilon [0{,}0.74] \qquad \textbf{Equation 3.22 [33]}$$

$$\mu_m^c(p,T) = \mu_m(p,T)\frac{1}{1 - f_c^{\,1/3}(p,T)}, \qquad f_c \epsilon [0.74{,}1] \qquad \textbf{Equation 3.23 [33]}$$

Where $\mu_m^c(p,T)$ and $\mu_m(p,T)$ is the mud viscosity as a function of pressure and temperature with- and without cuttings, f_c represents the cuttings concentration as a function of pressure and temperature.

This model can be modified [23] to fit other rheology models such the power-law to possibly give a better fit with a real drilling fluid. However, these are still mathematical models which, at best, only give an approximation of the real case.

3.5.4 Influence by presence of gas

Presence of gas in the well will also affect the mud rheology. The magnitude depends on the gas fraction in the fluid. It is also reasonable to assume different results if gas is dissolved in the mud opposed to if the gas exists in a separate, dispersed phase. For gas existing in a dispersed phase viscosity will tend to increase with increasing gas volume fraction because flow lines are distorted around the bubbles [34]. To estimate the new viscosity a modified version of the Hastcheck or Einstein equations can be used, substituting volume fraction of cuttings for volume fraction of gas. However, when these models are used other considerations must be taken since both the model by Einstein and Hatcheck considers the dispersed phase as spherical and non-deformable. While this might be a good approximation for solid particles, gas bubbles will behave differently. Bubbles dispersed in a liquid will tend to elongate as the viscosity and shear rate of the flowing liquid increases [34]. A correction factor will therefore be necessary.

When gas dissolves in the fluid it is not necessary to consider the gas bubbles as separate "particles", however modeling the behavior accurately is still challenging. It is also reasonable to assume that presence of gas will influence on how the mud will react to changes in temperature and pressure. This coincides with an analysis made by Cayeux [23] (Figure 3.8), where the rheology of a drilling foam with 5% quality (5% gas volume fraction) at 50 bar and 50°C is compared to the rheology of the original mud at different temperatures and pressures. The results show higher deviation when the pressure decreases, this is reasonable as gas is more compressible than the fluid giving a higher volume fraction of gas at lower pressures. The presence of gas also has different impact on the rheology when only the temperature is varying, e.g. difference between 40bar, 50°C and 40bar, 20°C. Note that this chart is representing the rheology of drilling foam and not a drilling fluid with a gas influx. However, as the drilling foam is modeled as an aerated fluid, the resemblance is convenient. This graph will accordingly give some indications of what will be the rheology effects of gas influxes into drilling mud.

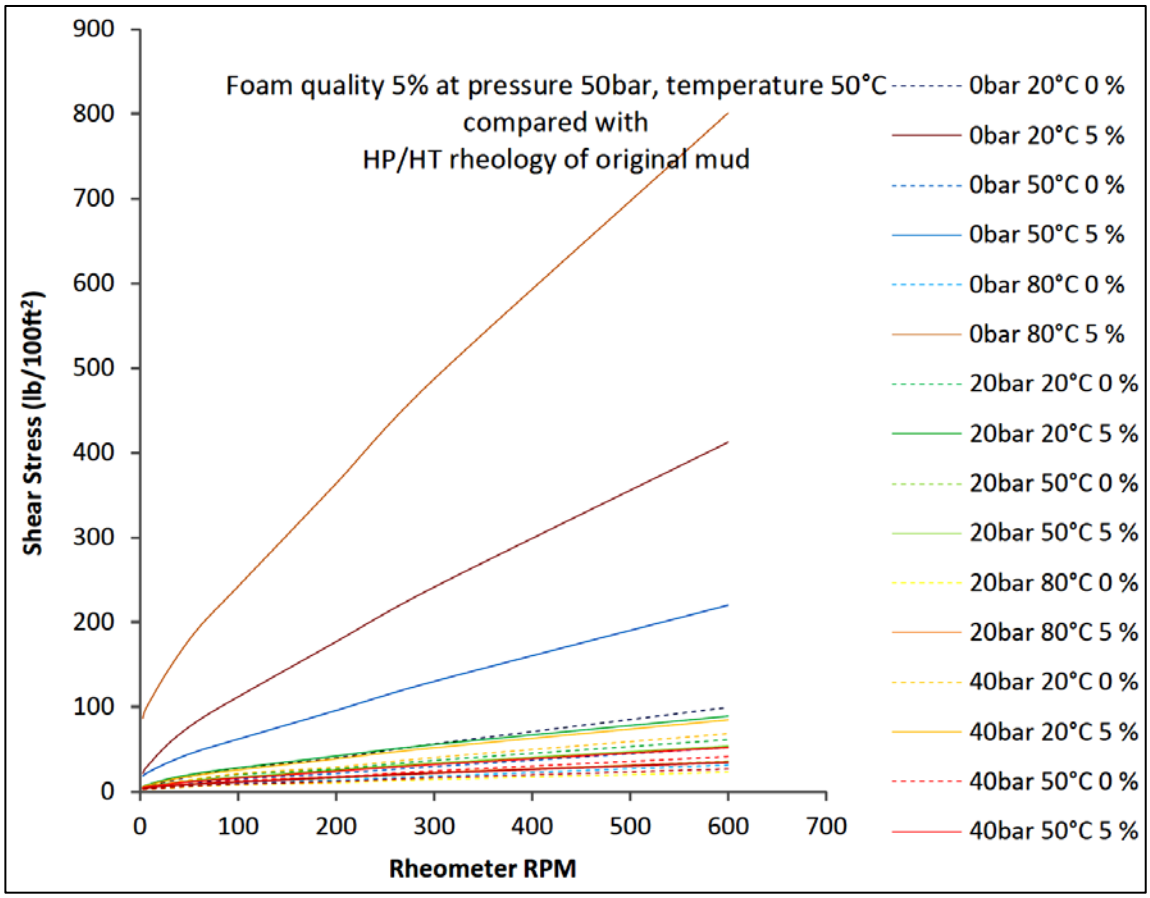

Figure 3.8: Rheology of drilling foam with 5% gas volume fraction at 50 bars and 50°C [23]

4 Drilling hydraulics

Drilling hydraulics is study of the hydraulic phenomena that occur in the wellbore during drilling. Ultimately, this is what relates mud density, rheology, cuttings bed formation etc. to the wellbore pressure. Determining pressure loss is generally a complicated matter. As discussed above, there are a number of uncertainties in the parameters of the mud itself, the content of solids and formation fluids. In addition there are large variations in flow area and wall friction, from the interior of the drillpipe, through the BHA components and the bit, and up the annulus with different diameters and drillstring eccentricity. Buildup of cuttings bed may occur in inclined parts of the well. In addition, the different flow regimes that will be experienced in a wellbore have considerably different properties, affecting the hydraulic as illustrated in Figure 4.1. Different flow regimes may be experienced at different stages during the course of a wellbore.

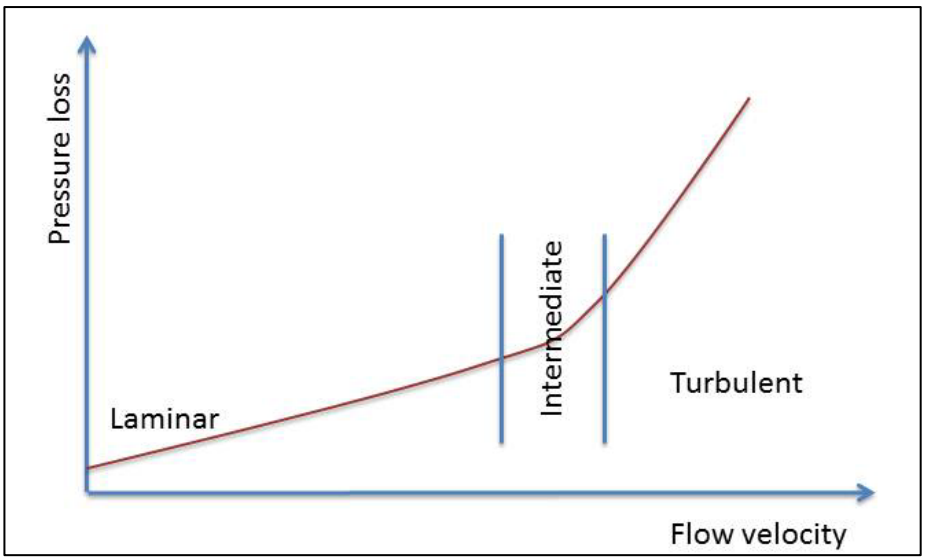

Figure 4.1: Different flow regimes and the effect on pressure loss

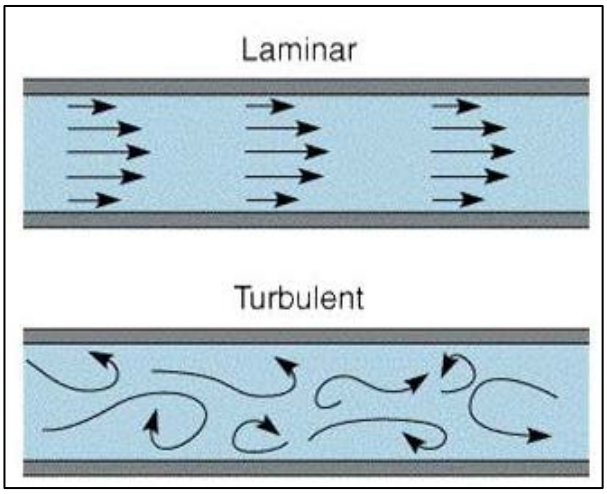

Figure 4.2: Laminar and turbulent flow profiles

Flow regimes are characterized as: laminar, intermediate and turbulent flow. Laminar flow is given by streamlines flowing in parallel layers with highest velocity in the middle and lowest at the boundaries (walls). Turbulent flow exhibit chaotic and stochastic streamlines also known as eddies. Intermediate flow is neither laminar nor fully developed turbulent flow. The different flow regimes can be determined by Reynolds number (Re):

$$Re = \frac{inertial\ force}{Viscous\ force} = \frac{\rho\ \bar{v} D}{\mu} \qquad \textbf{Equation 4.1}$$

Where D is the hydraulic diameter, $\bar{v}$ is the mean flow velocity, μ is the dynamic viscosity and ρ is the fluid density. The general perception is that the flow regimes will be established as laminar (Re < 2100), intermediate (2100 <Re< 4000) or turbulent (Re > 4000). However these values will vary as the fluid deviates from Newtonian behavior. To account for this, a critical Reynolds number as given by Ryan and Johnson [35] may be calculated to establish when transition occurs. Or as in this case utilize a modified Reynolds number to account for the fluid behavior. This is presented in the following section.

Pressure loss in laminar flow is directly related to the effective viscosity of the fluid i.e. the shear stress and shear rate. In turbulent flow pressure loss is mostly influenced by inertial properties and only indirectly by the viscous properties of the fluid. The pressure loss calculated will also be affected by the mathematical model used to characterize the flow. In section 3.5.1 some of the most common models were mentioned.

4.1 Pressure loss calculation model

In the following a principal descriptions of the flow model that will be used for pressure calculation will be presented. Some details are omitted due to confidentiality agreements.

Consider the model by Robertson and Stiff [27] given in general from in Equation 3.19, for pressure loss in laminar flow. As previously discussed, one of the advantages of the Robertson and Stiff model is the possibility to derive an explicit relationship between volumetric flow rate and shear rate in pipe flow:

$$\dot{\gamma} = \frac{3B+1}{4B} \times \frac{8\bar{v}}{d} + \frac{C}{3B} \qquad \textbf{Equation 4.2 [27]}$$

Where $\bar{v}$ is the bulk velocity and d is the pipe ID. The corresponding equation for flow in a concentric annulus with no pipe movement can be written as:

$$\dot{\gamma} = \frac{2B+1}{3B} \times \frac{12\bar{v}}{d_2 - d_1} + \frac{C}{2B} \qquad \textbf{Equation 4.3 [27]}$$

Where d_2 is the wellbore diameter and d_1 is the pipe OD.

The pressure loss in laminar flow (dp/ds) is determined by solving the following equations. Equation 4.4 represents flow inside drill pipe and Equation 4.5 represents flow in a concentric annulus.

$$\left(\frac{4AC^B}{d \times \frac{dp}{ds}}\right)^{3+\frac{1}{B}} - (3B+1)\left(\frac{4AC^B}{d \times \frac{dp}{ds}}\right)^{\frac{1}{B}}\left(1 + \frac{6\bar{v}}{dC}\right) + 3B = 0 \qquad \textbf{Equation 4.4 [36]}$$

Where d is the pipe inner diameter.

$$\frac{48\bar{v}AC^B}{d^2(1-\alpha)^2 \times \frac{dp}{ds}} = \frac{3B}{2B+1}\left(\frac{d(1-\alpha)\frac{dp}{ds}}{4AC^B}\right)^{\frac{1}{n}-1} - \frac{6AC^B}{d(1-\alpha)\frac{dp}{ds}} + \frac{3}{2(B+1)}\left(\frac{4AC^B}{d(1-\alpha)\frac{dp}{ds}}\right)^3$$

Equation 4.5 [36]

Where d = d_2 is wellbore diameter and α = d_1/d_2.

Pressure losses in turbulent flow can be defined by deriving a local power law model based on the Herschel-Bulkley rheology model (Equation 3.16) and a modified Reynolds number. The local power law rheology model is given as follows:

$$\tau_w = K'\dot{\gamma}_{Nw}^{n'}$$

Equation 4.6 [37]

Where τ_w represents the wall share stress. The other parameters of this equation are defined as follows, with n being the flow behavior index:

$$n' = \frac{n(1+\xi)(n\xi+n+1)}{1+n+2n\xi+2n^2\xi^2}$$

Equation 4.7 [37]

$$K' = \frac{\tau_0 + K\left(\frac{2n'+1}{3n'}\dot{\gamma}_{Nw}\right)^n}{\dot{\gamma}_{Nw}^{n'}}$$

Equation 4.8 [37]

$$\dot{\gamma}_{Nw} = \frac{12\bar{v}}{d_1 - d_2}$$

Equation 4.9 [37]

$$\xi = \frac{\tau_0}{\tau_w}$$

Equation 4.10 [37]

When all necessary parameters are calculated, Reynolds number can be determined as:

$$R_e = \frac{\rho \bar{v}^{2-n'}(d_2 - d_1)^{n'}}{K' 12^{n'-1}}$$ **Equation 4.11 [37]**

By Reynolds number it is possible to define if the flow is laminar, turbulent or neither, in which case the flow is characterized as intermediate. Laminar flow is defined by $\mathrm{R_e} < 3250 - 1150\mathrm{n}'$ and turbulent by $\mathrm{R_e} > 4150 - 1150\mathrm{n}'$.

If turbulent flow has been established, the friction factor (f) is calculated by solving the following equation given by Founargiotakis et al. [38]:

$$\frac{1}{\sqrt{f}} = \frac{4}{(n')^{0.75}} \log\left(R_e f^{1-\frac{n'}{2}}\right) - \frac{0.395}{(n')^{1.2}}$$ **Equation 4.12**

Pressure loss is then calculated according to fanning friction, where d_{hyd} is the hydraulic diameter and $\bar{v}$ is the mean flow velocity:

$$\frac{dp}{ds} = \frac{2f\rho\bar{v}^2}{d_{hyd}}$$ **Equation 4.13**

If the calculated Reynolds number indicates an intermediate flow regime, an interpolation is performed between the turbulent and the laminar pressure loss values in order to model a smooth transition.

The models listed above for both laminar and turbulent flow in annulus only considers a concentric annulus with no pipe rotation. To generate a more realistic result correction factors are applied. The following correction factor for eccentricity was derived by Haciislamoglu et al. [39] based on the Herschel-Bulkley law:

$$\left(\frac{dp}{ds}\right)_{ecc} = C_e \left(\frac{dp}{ds}\right)_{conc}$$ **Equation 4.14**

Where C_e is the correction factor for eccentricity given for laminar and turbulent flow respectively:

$$C_e = 1 - 0.072\left(\frac{e}{n}\right)\left(\frac{d_1}{d_2}\right)^{0.8454} - \frac{3}{2}\left(e^2\sqrt{n}\right)\left(\frac{d_1}{d_2}\right)^{0.1852} + 0.96e^3\sqrt{n}\left(\frac{d_1}{d_2}\right)^{0.2527}$$

Equation 4.15

$$C_e = 1 - 0.048\left(\frac{e}{n}\right)\left(\frac{d_1}{d_2}\right)^{0.8454} - \frac{2}{3}\left(e^2\sqrt{n}\right)\left(\frac{d_1}{d_2}\right)^{0.1852} + 0.285e^3\sqrt{n}\left(\frac{d_1}{d_2}\right)^{0.2527}$$

Equation 4.16

Where e is the eccentricity factor and n the flow index.

IRIS has developed a correction factor on the same form applied for pipe rotation. This cannot be given here due to confidentiality agreements. Interested readers can however review the work by Ramadan et. al [40] which takes into account pipe rotation.

5 Case studies

In this chapter, three case studies based on two wells will be performed. The objective is to investigate how wellbore position uncertainty will affect the uncertainty in the wellbore pressures at the bottom hole and at a critical depth, a distance far away from the pressure sensor. This will be performed according to the method described in chapter 1. In each case the bottomhole pressure will be recorded at various depths throughout the section in addition to the measurements taken by an annulus sensor placed just below the casing shoe of the previous casing. The effects of wellbore position uncertainty will be seen in connection with uncertainty in the mud density, the formation geothermal properties and the oil – water ratio of the drilling mud.

In section 3.4, a number of factors influencing the mud density were discussed. Given the number of influencing factors, it is reasonable to assume an uncertainty of a significant magnitude. The analysis of the mud density uncertainty will be performed for a wide range of mud weights, at various depths throughout the analyzed section. However, an accurate determination of the density uncertainty itself, will not be provided in this thesis.

The basic theory and physics of uncertainty in geothermal properties of formation rock was discussed in sections 3.1.2 - 3.1.5. Uncertainties in these parameters are acknowledged by the industry, however few analyses discussing the actual implications have been presented. The analysis will be performed by alternately changing the values for specific heat capacity and thermal conductivity. This is performed to enable isolation of the parameters and review which has the highest implication. The values used in the analysis are 900 and 1500 J/kg·K for specific heat capacity and 1,4 and 3 W/m·K for thermal conductivity. These values are identical to those used by Toft [18] in his analysis, discussed in section 3.1.5. In all the cases, the circulation will be simulated for 24 hours at both the top and TD of the section.

Local variations in the oil-water ratio of the drilling mud may be experienced in a downhole environment. These may occur as a result of influxes from hydrocarbon bearing formations or by exposing the phases of different compressibility to high pressures and temperatures. As the oil-water ratio change, so will the thermo-physical properties of the mud. Compared to oil, water has a higher capability to both store and transfer heat. The specific heat capacity and

thermal conductivity of the mud will accordingly decrease as the oil-water ratio increases. Rheological properties will also be affected. The analysis of the effects of uncertainty in oil – water ratio of mud will in each case be performed both at the top and TD of the section. The oil – water ratios used in the simulations will be altered about the original value of the mud used in the specific case. Similar to the analysis of formation geothermal properties, the circulation will be simulated for 24 hours.

5.1 Course of the analysis

A survey editor software will be used to calculate the related uncertainty for the given wellbore. A snapshot of the program is given in Figure 5.1. In this software the Wolff and de Wardt [2] uncertainty theory is implemented. This enables the calculation of the ellipsoids of uncertainty for a given survey station. These ellipsoids are displayed as ellipses on the horizontal projection and vertical section of the wellbore. This software has also implemented the derived method from chapter 1, enabling the calculation of the maximum and minimum TVD trajectory. These two trajectories can furthermore be exported for use in connection with a wellbore configuration software.

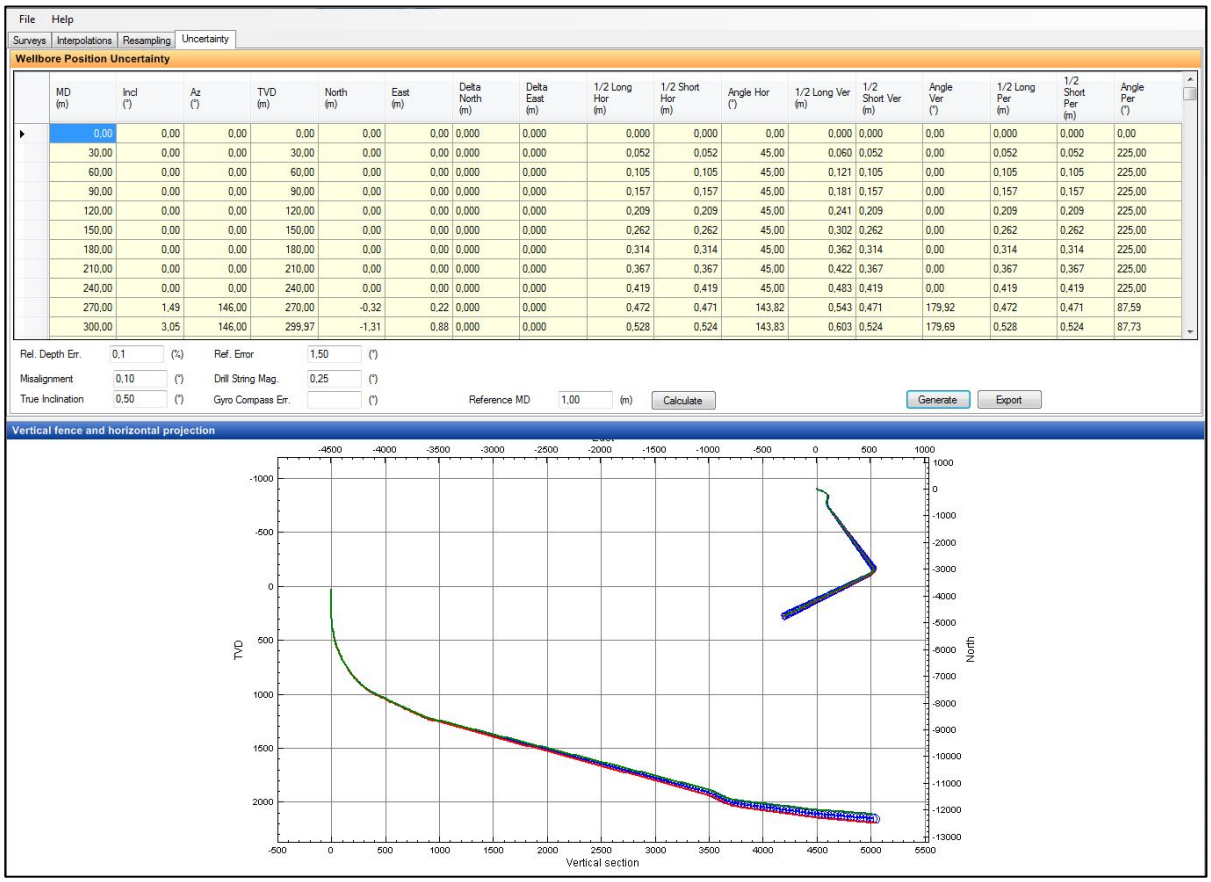

Figure 5.1: Survey editor software

In the wellbore configuration software, the specifications for the wellbore, casing setting depths, fluids, temperature profiles, geothermal properties, drillstring etc. are entered. These are specified for the given section that is the subject of the analysis. In Figure 5.2 some of the

specifications of case 1 are given. Here the analysis will focus on drilling of the 8½” x 9½” section. Accordingly, the last casing set in the specifications is the 9⅝”.

From the general specification, a number of modifications can be made to analyze the effects of altered mud properties and geothermal properties of formations for different trajectories. From here it is also possible to specify the location of an annulus sensor. This sensor is set at a certain depth and will give information regarding either the local pressure, temperature etc. In these cases the sensor is placed just below the last casing shoe and is set to monitor the pressure.

When all the specification for the well and drilling program is set in the wellbore configuration software, this program is exported and used as a base in the drilling calculator.

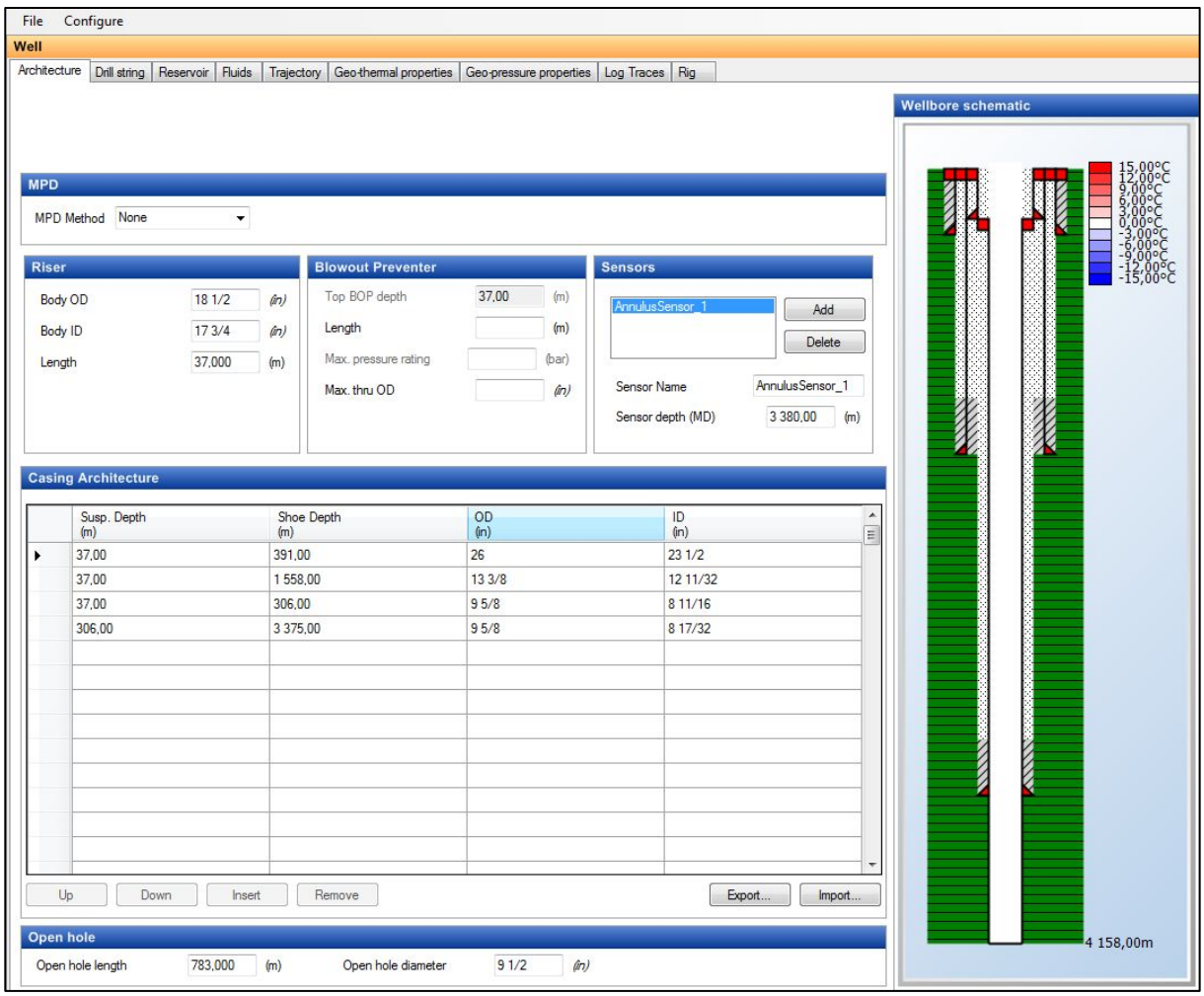

Figure 5.2: Wellbore configuration software

The drilling calculator, displayed in Figure 5.3, is the software performing the actual calculation of the wellbore pressure development as a function of time. A set of standard simulation parameters needs to be set. These include the bottomhole depth where the analysis takes place, the bit depth, the mud density corrected for temperature effects according to the given mud temperature. For the purpose of consistency in these analyses, the bit depth and bottomhole depth is always set equal. Thus, if the purpose is to analyze the pressure effects when circulating at 3400 m MD, both bit depth and bottomhole depth is set to this value, likewise for other depths. The pump flow rate and surface RPM is set according to the original values used when drilling, given in the daily drilling reports.

This software also allows for drilling and the study of transient cutting transportation by entering values for surface torque, ROP etc. However as the other simulations can be performed about 10x faster than real-time, the simulations of transient cuttings transportations are performed in real-time, and was therefore not possible to performed within the time-frame given for this project. Only the effect of circulation is studied together with the effects of pipe rotation. To study the pressure variations caused by mud density uncertainty due to cuttings transportation, the density value is instead altered for a wide range of solutions.

The pressure is given as a function of simulated time. For the basic simulations only reviewing the direct effects of wellbore position uncertainty or mud density uncertainty, the simulation is stopped after 1000 simulated seconds or so. When the purpose of the simulations was to review effects of uncertainty in geothermal properties of formation rock or thermo-physical properties of mud, the simulated time was set to 24 hours in order for pressure and temperature to stabilize. These simulations are time-consuming even if transient cuttings transportation is not considered, each needing about 2-3 hours of processing time to complete. For this reason, the number of data samples in these analyses had to be limited.

To study combined effects of uncertainty in multiple parameters, all the simulations were performed with basis in both the minimum and maximum TVD trajectory.

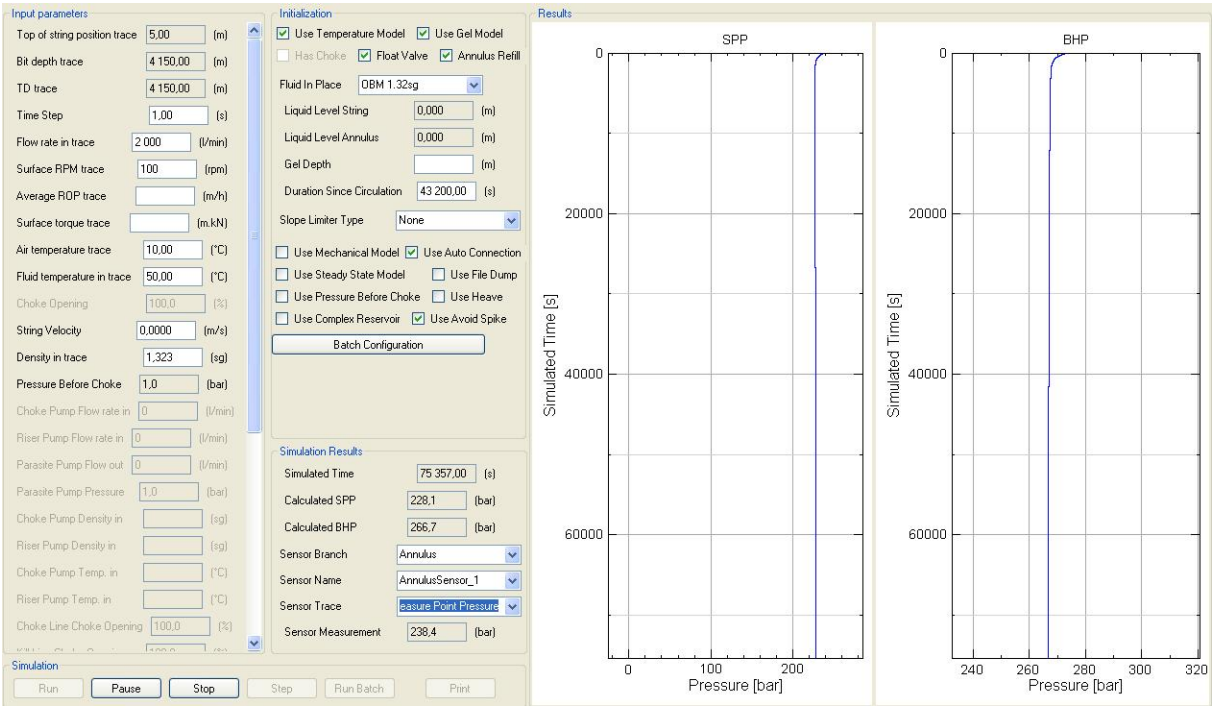

Figure 5.3: Drilling calculator software

5.2 About the cases

In the following three case studies will be presented. These three cases are based on two wells, named well A and well B. Case 1 will focus on analysis of the 8½" x 9½" section of well A. The size 8½" x 9½" implies that the well is drilled with an 8½" drill bit followed by a 9½" underreamer, which gives the resulting openhole size. Case 2 and 3 will focus on the 12¼" and 8½" section of well B respectively.

5.2.1 Well A

Well A is an ERD well with a length of 5934 m MD and 2151 m TVD. The trajectory is given in Figure 5.4, including both the horizontal projection and vertical unfolded section. The general configuration of hole sizes, casing setting depths etc. is given in Table 5.1. Well A has a long horizontal departure which incorporates a horizontal turn, building azimuth to 207° and inclination to 85° at TD.

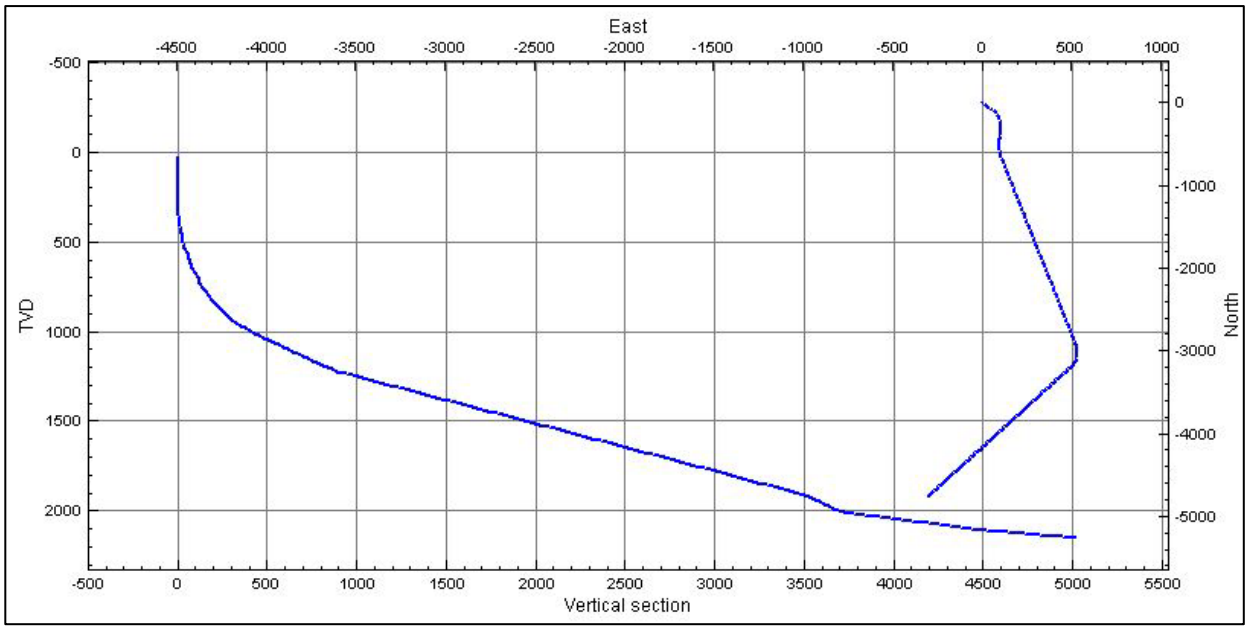

Figure 5.4: Vertical section and horizontal projection of well A

Table 5.1: General configuration of well A

Section	MD at TD [m]	TVD at TD [m]	Mud Weight [s.g.]	Incl. at TD [°]	Az. at TD [°]
32" (26" conductor)	396	395,2	1,03 – 1,07 WBM	7,5	146
17½" (13⅜" casing)	1561	1175	1,06 – 1,18 WBM	65,0	169,57
12¼" (9⅝" casing)	3384	1654	1,60 – 1,62 OBM	75,27	169,57
8½" x 9½" (7⅝" liner)	4150	1851	1,32 – 1,34 OBM	75,41	207
6½" Openhole	5934	2151	1,12 – 1,14 OBM	85	207

The first section on the well was drilled as a 17½" pilot hole followed by a 32" hole opener to a TD of 396m MD. This section builds inclination from 0° to 7,5° and has a 146° azimuth at section TD. A 26" conductor is set.

The following 17½" section has a length of 1170m drilled to a TD of 1561m MD and 1175m TVD. This section builds inclination from 7,5° to 65,0° and turns from 146° to 186° azimuth, before turning back to 169,57°. A 13⅜" casing is set.

The next section drilled is the 12¼" section. This is the longest section of the well with a span of 1828 m MD and 480 m TVD. TD of the section is at 3384m MD and 1654 m TVD. A 9⅝" casing is set at TD.

The following section is an 8½" x 9½" section drilled to 4162 m MD and 1854 m TVD. A 7⅝" liner is cemented at TD. Drilling of this section is the subject of investigation for this well. The operator have previously experienced problems with the formation at the depth where the 9⅝" shoe is located. Leak-off tests in previous well have fractured the shoe, resulting severe losses at lower ECD. The section itself is not particularly long with its 766m MD, however as the well exceeds 4 km during this section, substantial uncertainty in the wellbore position can be expected.

The final stage is a 6½" openhole section. The section reaches the total depth of 5934 m MD and 2151 m TVD. During drilling of this section, the inclination will drop from 75° to 61° and then build to 85° at TD. Azimuthal angle remains constant.

Figure 5.5 below displays the pore and fracture pressure gradients for well A. Margins appear to be adequate with no distinctive hazard zones. The pressure spike observed at 1800 m is approximately where the shoe of the 7⅝" liner is set. Figure 5.6 displays the geothermal gradient at this location. Accordingly, the temperature at TD of the 8½" x 9½" section is approximately 60°C.

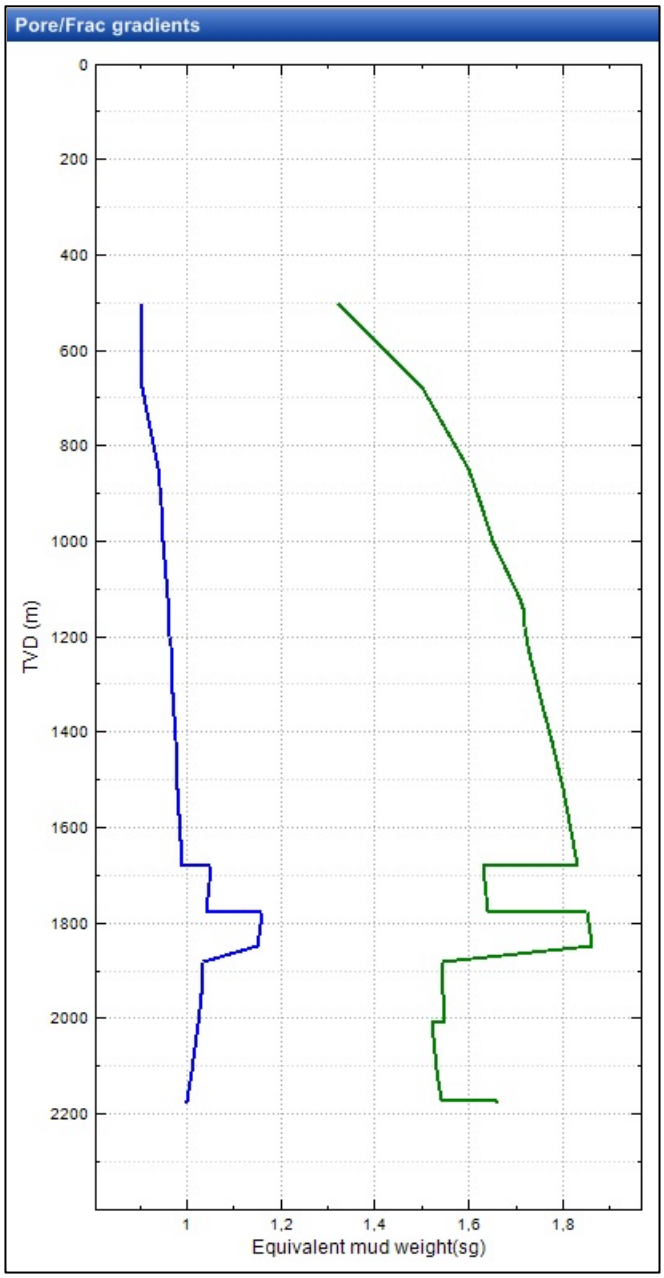

Figure 5.5: Well A – Pore- and fracture pressure gradient curves

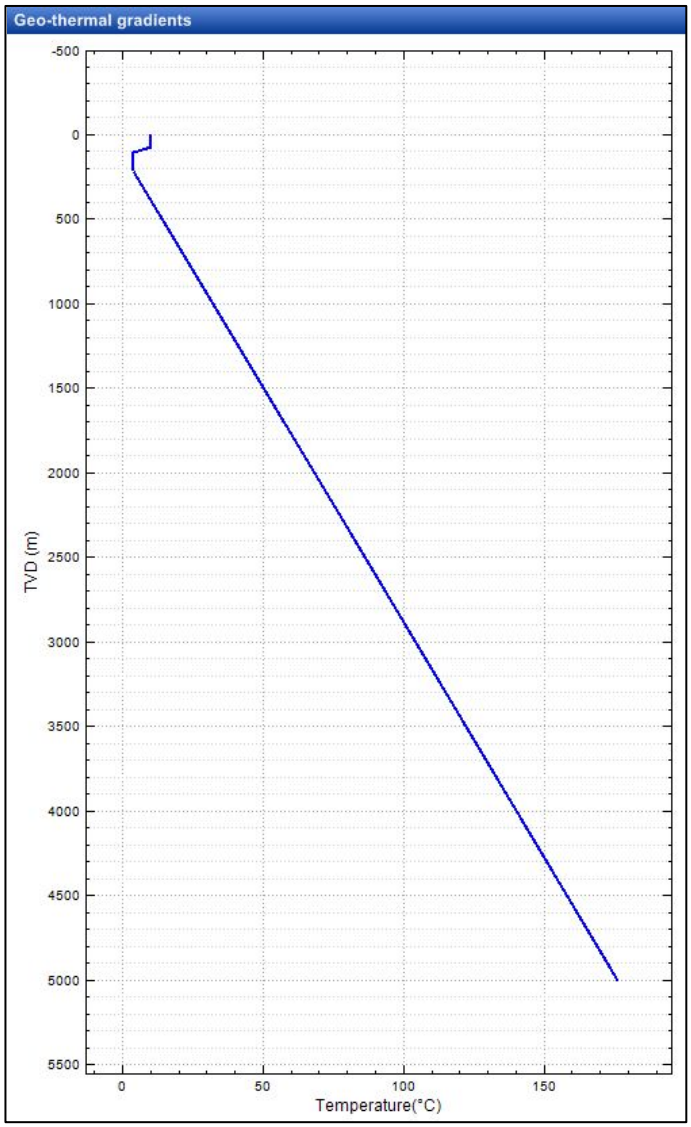

Figure 5.6: Geothermal profile - Well A

5.2.2 Well B

Well B is with its 8467m MD and 4146 m TVD, categorized [41] as an ultra-extended reach well. The well became the source of many problems for the operator and drilling contractor. However, wellbore pressures did not cause these problems. Instead they were caused by very high ratings of torque and drag. These high ratings were a result of the large sections with inclinations of above 35°. Inclinations in this range are unfavorable for cuttings transport when accompanied by inappropriate combinations of RPM and flow rate [42]. Large 6⅝" drill pipes had to be used in order to reduce pressure loss inside the pipe and support hole cleaning. In combination with the length – and depth of this well, high torque and drag ratings, low ROP and large stick-slip were experienced whenever weight was put on bit.

In Figure 5.7 the trajectory and also the complexity of well B is shown. Table 5.2 summarizes the general configuration with casing setting depths, mud weights, inclinations and azimuths.

The well started form a pre-drilled 32" slot with a 27" conductor set at 309 m MD and 309m TVD. Inclination started to build the last few meters of the section reaching 2,7° at the shoe. The section started off with an azimuth of 230,7° and gradually turned to reach 115,6° at TD.

The following 24" section was drilled to approximately 1192 m MD and 1130 m TVD. In this section the well starts by turning rapidly to 243° azimuth before turning eastwards to 220,5° at section TD. Inclination builds gradually to 25,4°. An 18⅝" casing is set and cemented to surface.

The 17½" section is with its 3085 m MD and 2070 m TVD the longest section of the well. Inclination increases changes to 50° in the start of this section and remains constant from 2000 m MD to the section TD of 4277 m MD. Azimuth remains constant throughout the section. A 13⅜" casing is set and cemented approximately 400m above the shoe.

In the 12¼" section the well starts by rapidly building inclination, reaching 84° after about 470 m of drilling. Azimuthal angle remains constant throughout the whole section. This is also a long section with a span of 2223 m MD and 371mTVD. A 9⅝" casing is set and cemented approximately 400 meters above the shoe

The following 8½” section proceeds from 6500m to 7625m with the same inclination as the previous section. After 7625 m the inclination start to drop, reaching 42,6° at 8250 m (section TD). Azimuth remains constant. The section length is 1750m MD with a vertical span of 409 m TVD. A 7” liner is set and cemented 600 m above the shoe.

The 6” reservoir section is the final stage of this well. Compared to the others, this is a short section drilled to the total depth of 8467 m MD and 4146 m TVD. Inclination drops to 40° in the start of the section and will otherwise remain constant along with the azimuth. A 4½” liner is set across the reservoir section.

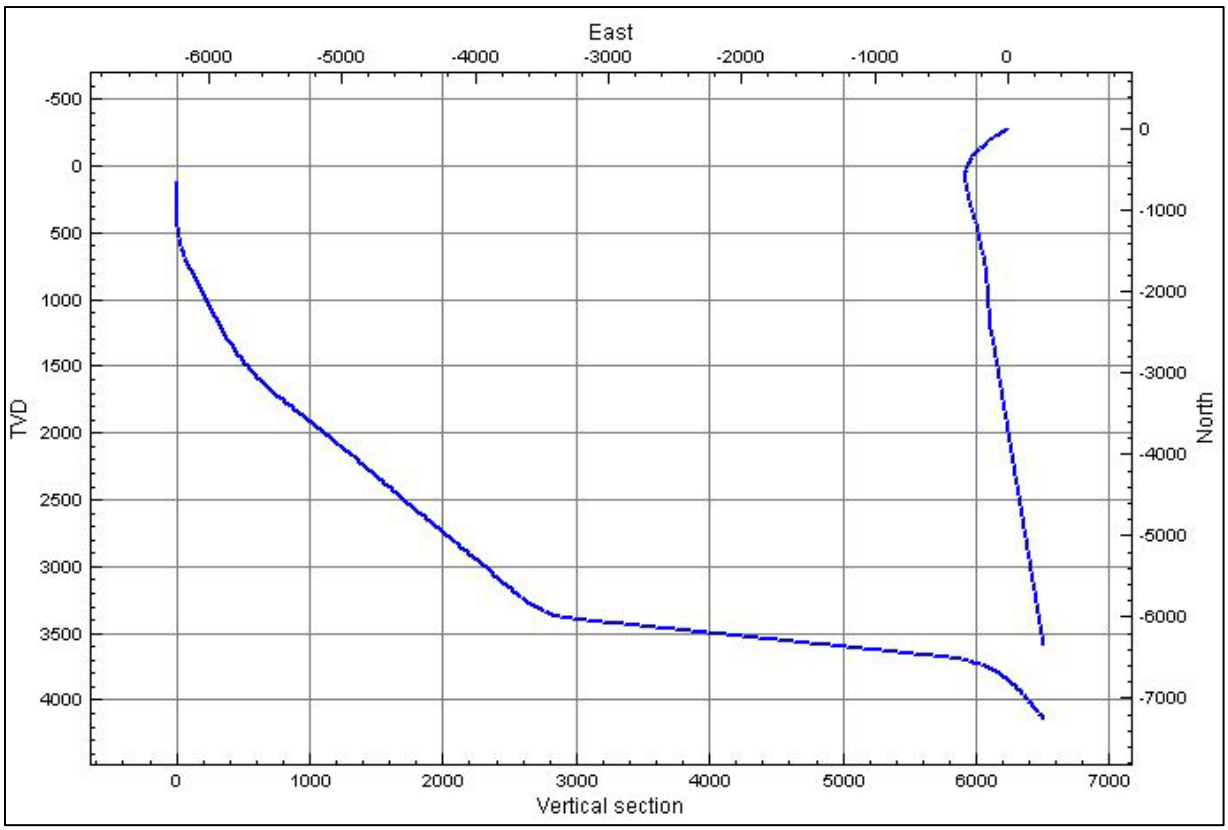

Figure 5.7: Vertical section and horizontal projection of well B

Table 5.2: General configuration of well B

Section	MD at TD [m]	TVD at TD [m]	Mud Weight [s.g.]	Incl. at TD [°]	Az. At TD [°]
32” (27” conductor)	309	309		2,7	115,6
24” (18⅝” casing)	1192	1130	1,03 – 1,30 WBM	25,4	220,5
17½” (13⅜” casing)	4277	3200	1,65 OBM	51,9	174,6
12¼” (9⅝” casing)	6500	3571	1,56-1,60 OBM	84,1	174,3
8½” (7” liner)	8250	3980	1,60-1,70 OBM	42,6	174,3
6” (4½” liner)	8467	4146	1,5-1,62 OBM	40	174,3

The 12¼” and 8½” sections were chosen for analysis to differ these from the 9½” section in the previous well. Adequate pressure margins are experienced in most of this well, including both the analyzed sections. However, the high flow rates, high RPM and ultra-extended reach provide good conditions for exploring the implication of uncertainty in parameters affecting the wellbore pressure. In Figure 5.8 the pressure gradients of well B is displayed. The blue, red and green lines represents pore, collapse and fracture pressure respectively. The black lines are calculated minimum and maximum wellbore pressure with no safety margin incorporated. Figure 5.9 displays the formation geothermal profile.

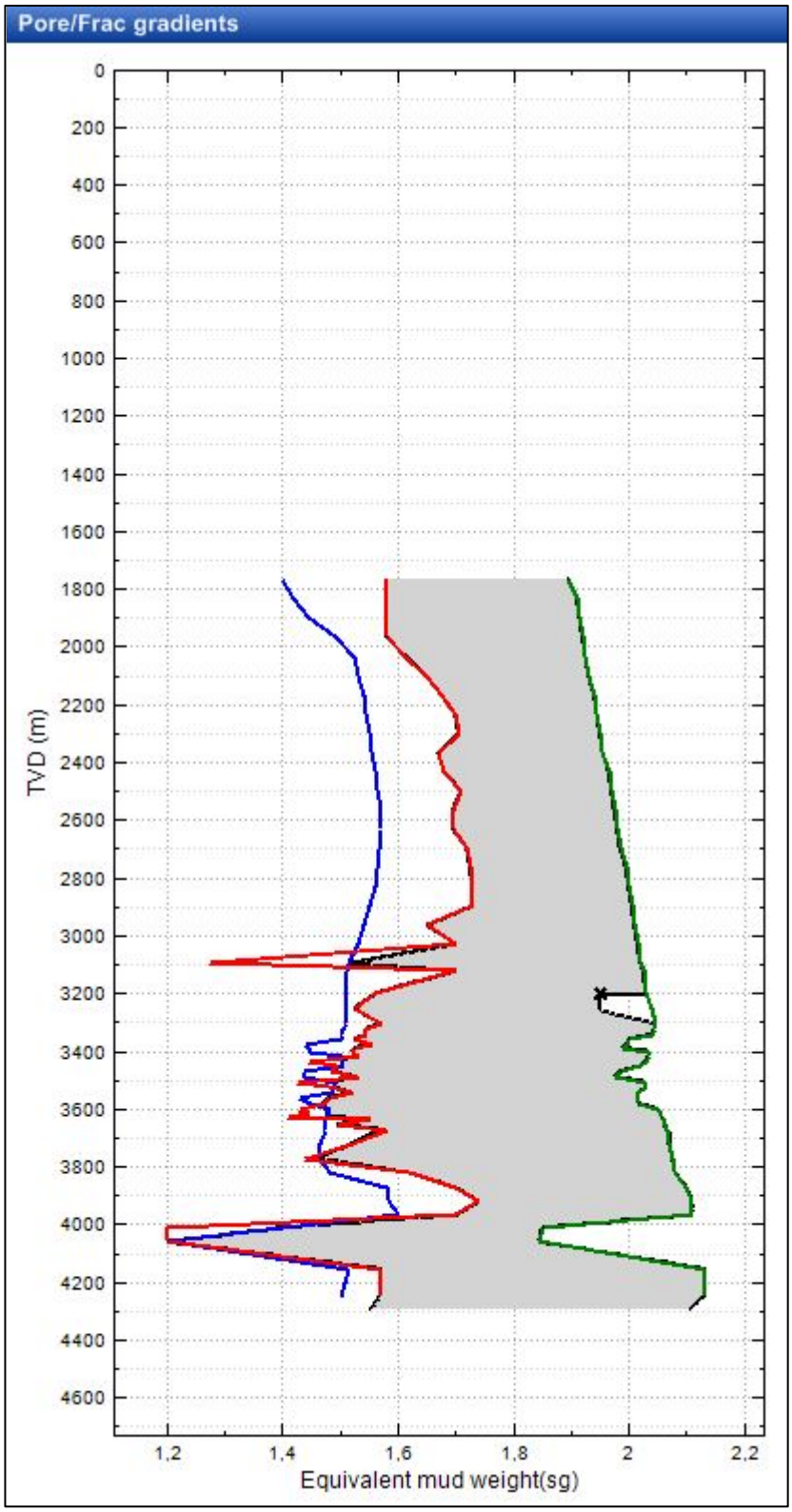

Figure 5.8: Pressure gradients of well B.

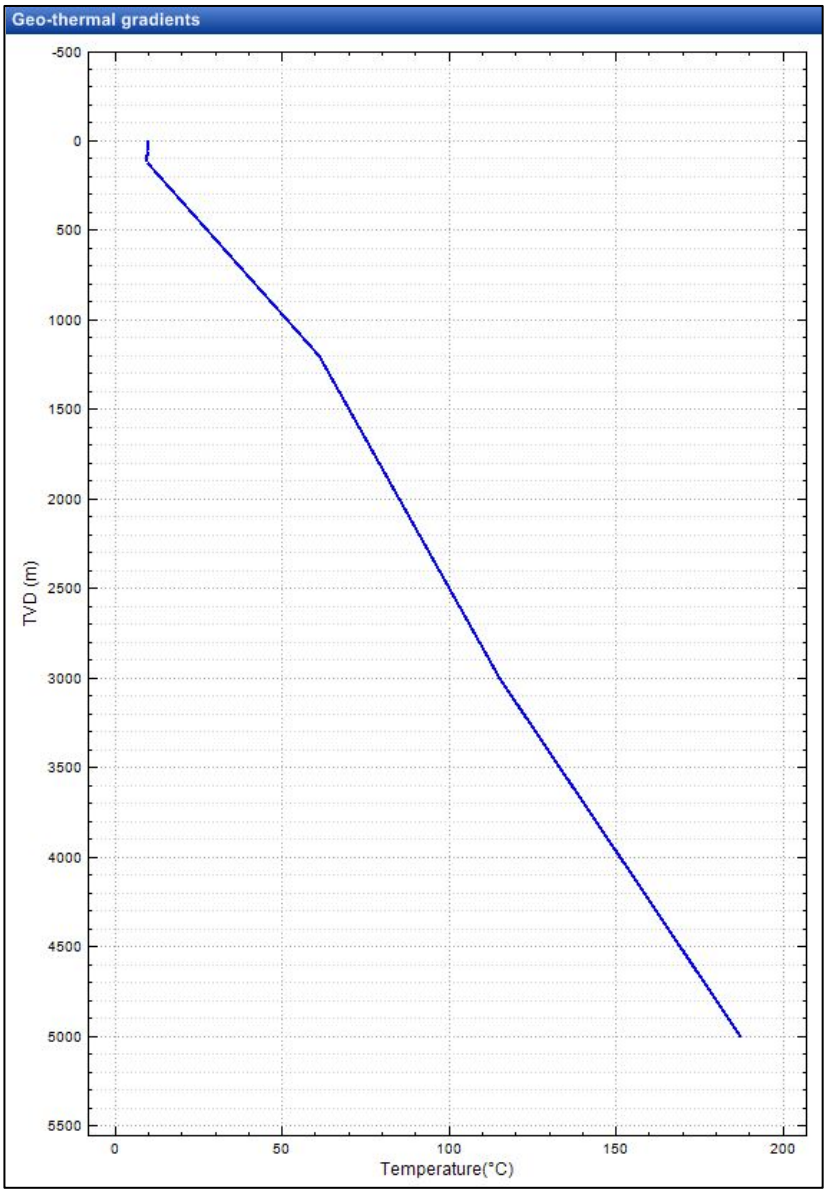

Figure 5.9: Geothermal profile – Well B

5.3 Wellbore position uncertainty

The basis of the analysis is the uncertainty in the wellbore position uncertainty and its effect on the annular pressure. To calculate the position uncertainty the trajectory of both wells is mounted into the survey editing software. This software implements the Wolff and de Wardt uncertainty theory to calculate the ellipsoids of uncertainty for all the survey stations of the well.

The next step is to calculate the trajectories associated with the minimum and maximum TVD of the last ellipsoid by implementing the method described in chapter 1. The calculation is performed in the survey editing software. The two trajectories will then be exported for use in drilling calculating software to perform the analysis. Note that for simplicity reasons, the two trajectories will only be calculated according to the last ellipsoid (at TD). Thus, the same trajectories will be used for analysis at both 3400m and 4150m instead of generating new trajectories exactly at the point of investigation. However, some analyses were conducted to justify the simplification and the results showed only small deviations between the calculated trajectories. These deviations were not seen as significant.

A summary of the calculated uncertainty values for both well A and B is tabulated in appendix 9.2.

5.3.1 Well A

Figure 5.10 shows the calculated uncertainty ellipses displayed together with the vertical section and horizontal projection of the wellbore. In Figure 5.11, the calculated minimum and maximum TVD trajectories are displayed as the green and red lines.

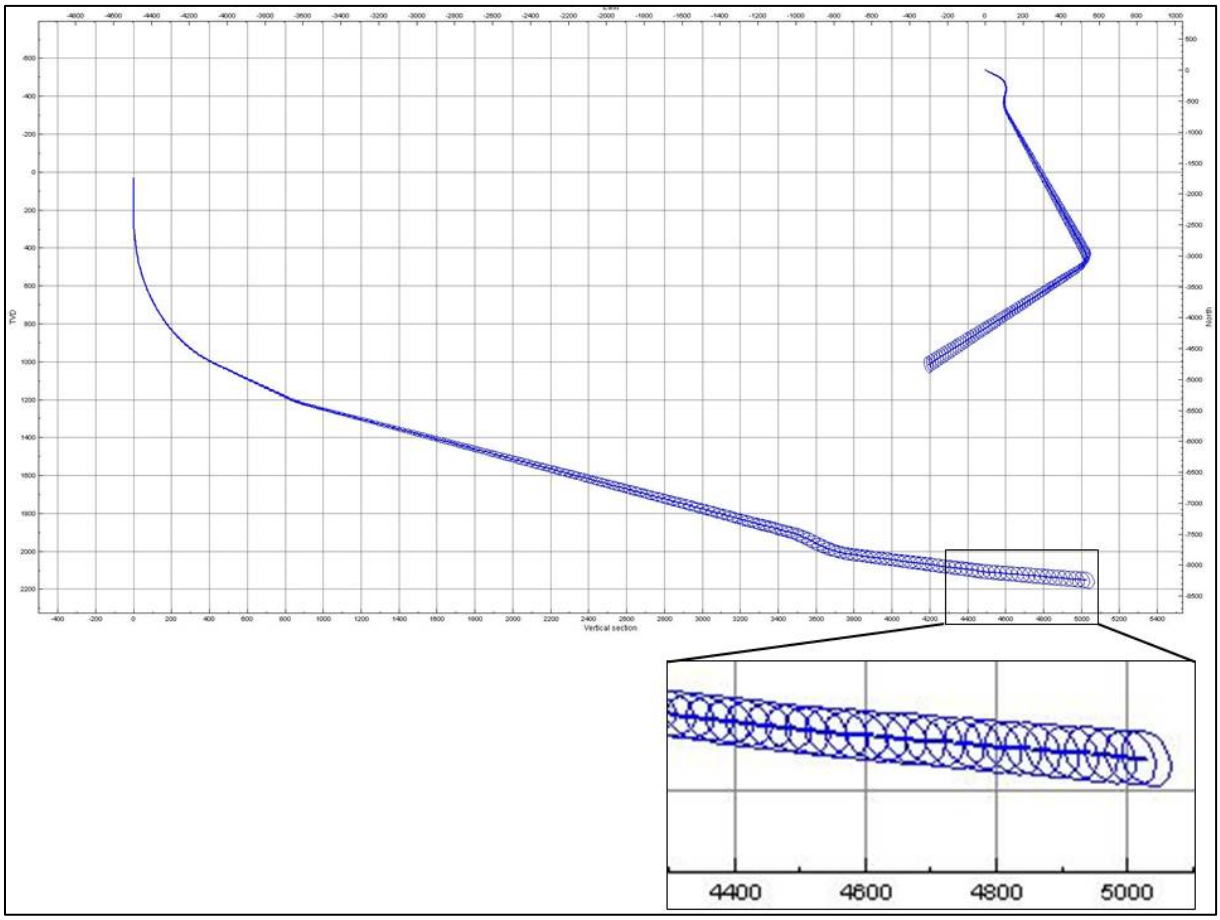

Figure 5.10: Trajectory for well A with uncertainty ellipses

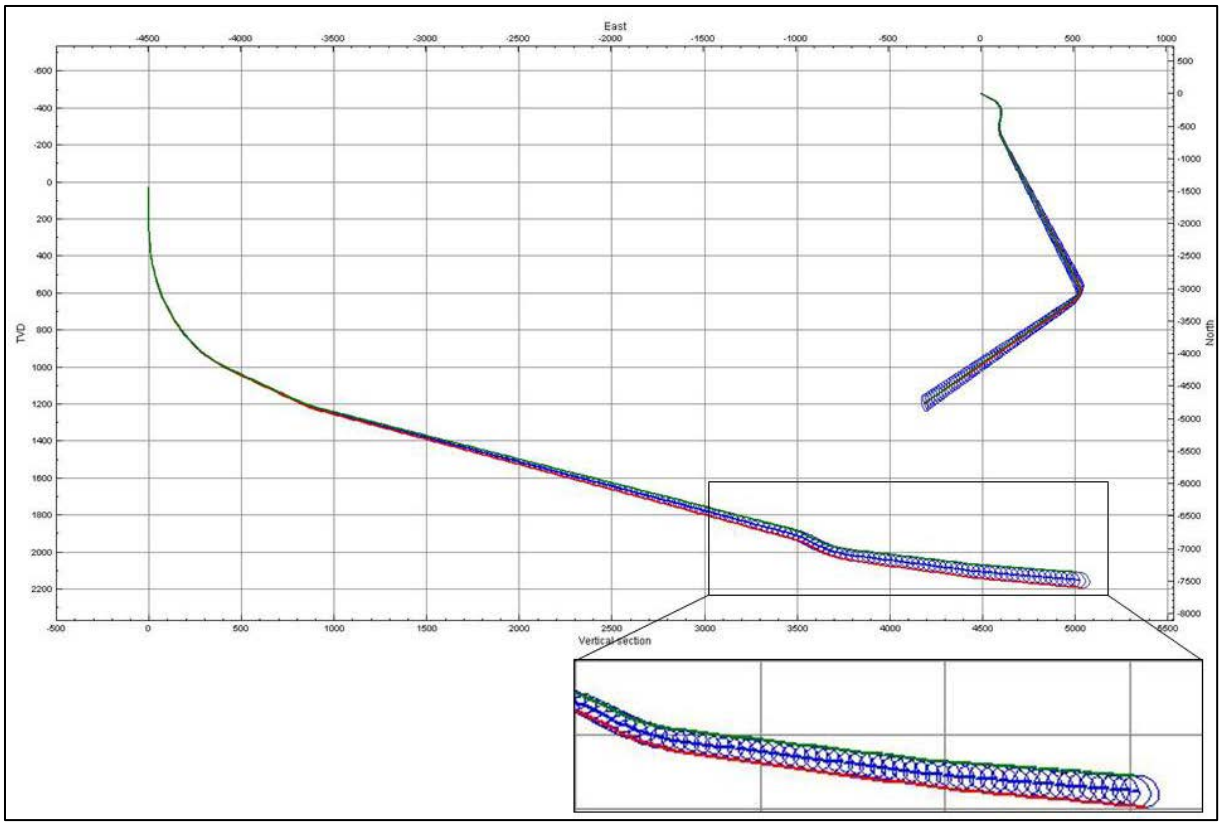

Figure 5.11: Wellbore position uncertainty of well A with minimum and maximum TVD trajectories

5.3.2 Well B

Figure 5.12 displays the calculated position uncertainty as ellipses together with original trajectory. The minimum and maximum TVD trajectories are included as the green and red lines.

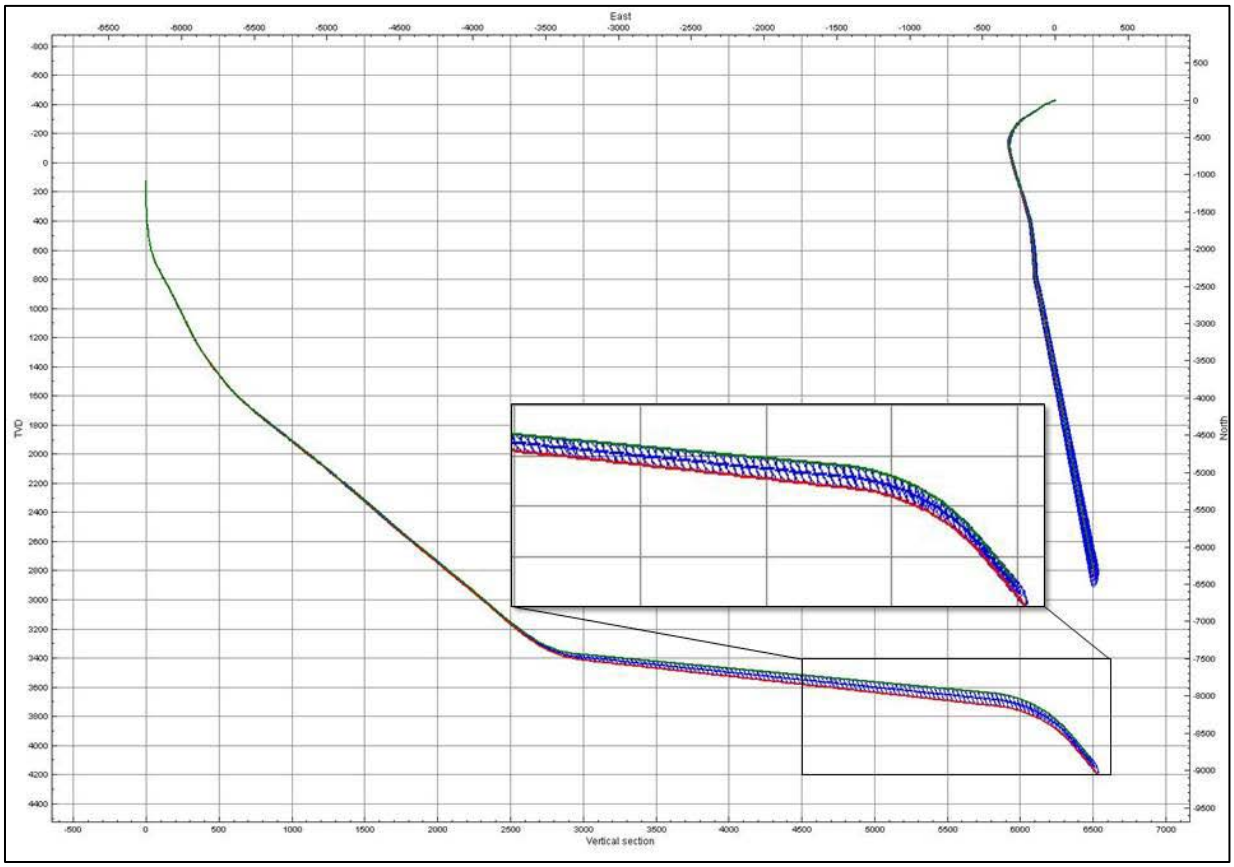

Figure 5.12: Wellbore position uncertainty of well B

5.4 Case 1 – Well A 8½" x 9½" section

To perform the analysis a set of base criteria as given in Table 5.3 were set. These parameters are according to those measured while drilling and given in the daily drilling reports. The mud density had to be corrected for thermal effects according to the temperature used in the simulation. The correction was performed according the chart given in Figure 5.13. Tabulated data for case 1 is presented in appendix 9.3

Table 5.3: Simulation parameters

9 ⅝" casing depth	3375	m
Sensor location	3380	m
Air temp	10	°C
Surface rotation	100	rpm
Simulated time	1000/86400	s
Flow rate	2000	l/min
Specific heat capacity of formation	900	J/kg·K
Thermal conductivity of formation	2	W/m·K
Geothermal Gradient	3,6	°C/100m
Mud temp	50	°C
Mud density at temperature	1,323	s.g.
Oil - Water ratio	3,17	
Specific heat capacity of mud	1554	J/kg·K
Thermal conductivity of mud	1,34	W/m·K

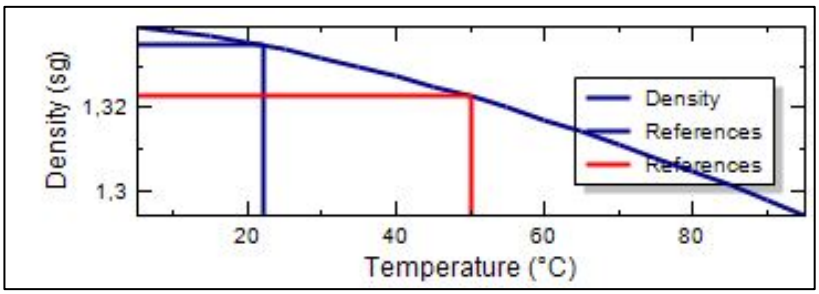

Figure 5.13: Thermal effects of mud used for drilling 8½" x 9½" section

5.4.1 Effect of wellbore position uncertainty isolated

In order to analyze the isolated effects by wellbore position uncertainty, the wellbore pressure of the original trajectory (without uncertainty) was compared to the pressures recorded from the trajectories representing maximum and minimum TVD. This was performed at various depths throughout the section. For each point of measurement the bottomhole pressure was recorded. In addition, the pressure measurement of a sensor placed 5 m below the 9⅝" casing shoe was recorded. For this analysis, the simulation was conducted for approximately 1000 simulated seconds. This duration was considered as adequate because the pressure now had stabilized from the initial fluctuating effect and the results were consistent.

Figure 5.14 displays the recorded bottomhole pressures for all three trajectories as function of depth (TVD). These are displayed together with the formation pore and fracture pressure gradients. All graphs display a linear relationship between equivalent mud weights and depth. A slight increase in pressure variances is observed with increasing depth. At the lowermost point (section TD) a difference of approximately ±3 bars is recorded. In comparison, the pressure difference at 3400 m is ±2,2 bars. Pressure differences throughout the section are evenly distributed between the trajectories.

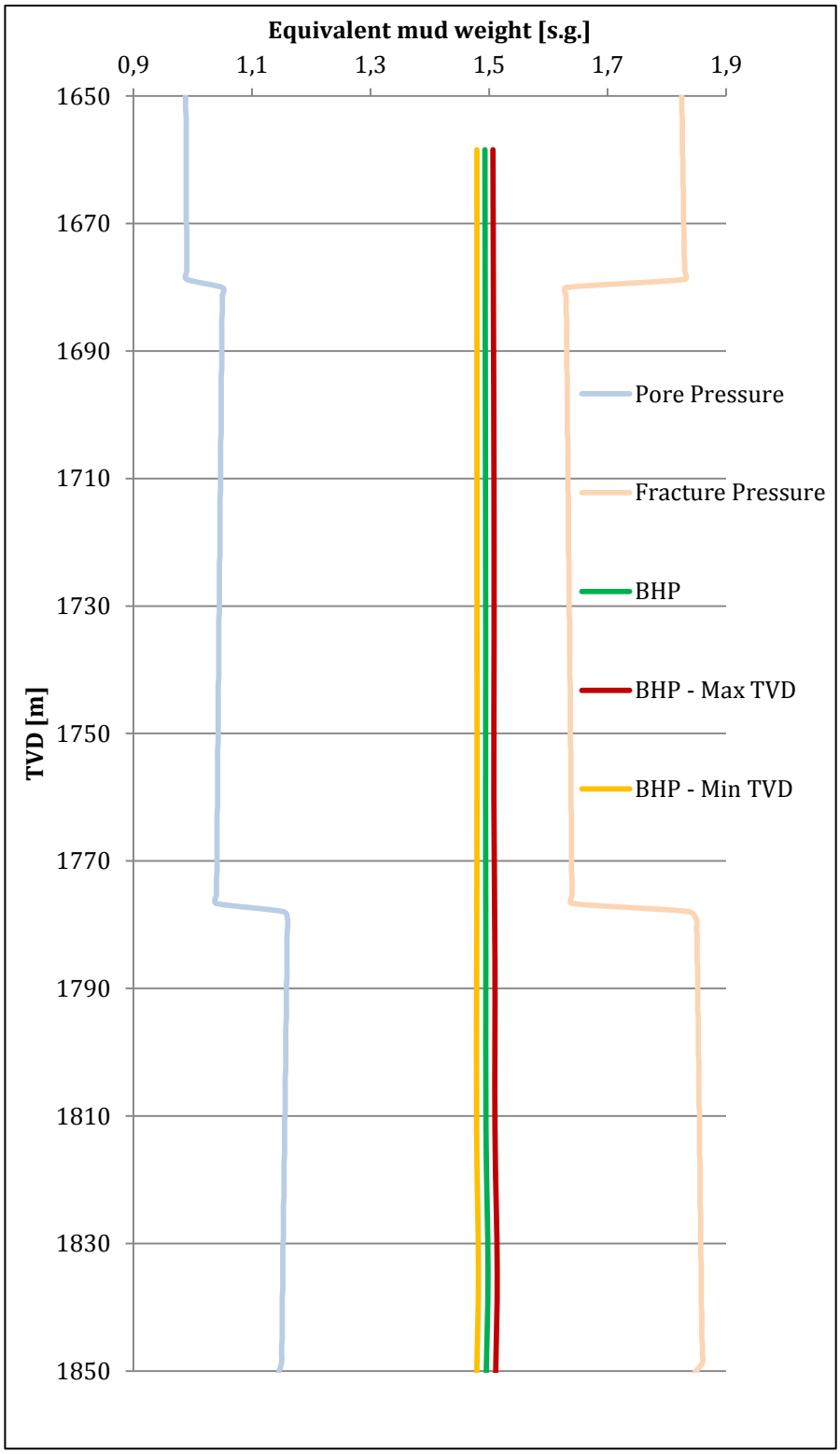

Figure 5.14: Effects of wellbore position uncertainty on BHP

In Figure 5.15 the development of the pressure below the 9⅝" casing shoe is displayed. The green dots represent the pressures recorded from the original trajectory and the yellow and red lines display the pressures recorded from the minimum and maximum TVD trajectories respectively. The bit depths on the x-axis are the bottomhole depths at the time when the pressure was recorded. The casing shoe pressure seems to be affected by well position uncertainty, but unaffected by the bottomhole depth. A pressure difference of approximately ±2,2 bare is experienced at the shoe. This difference is relatively consistent throughout the section, only small deviations occur.

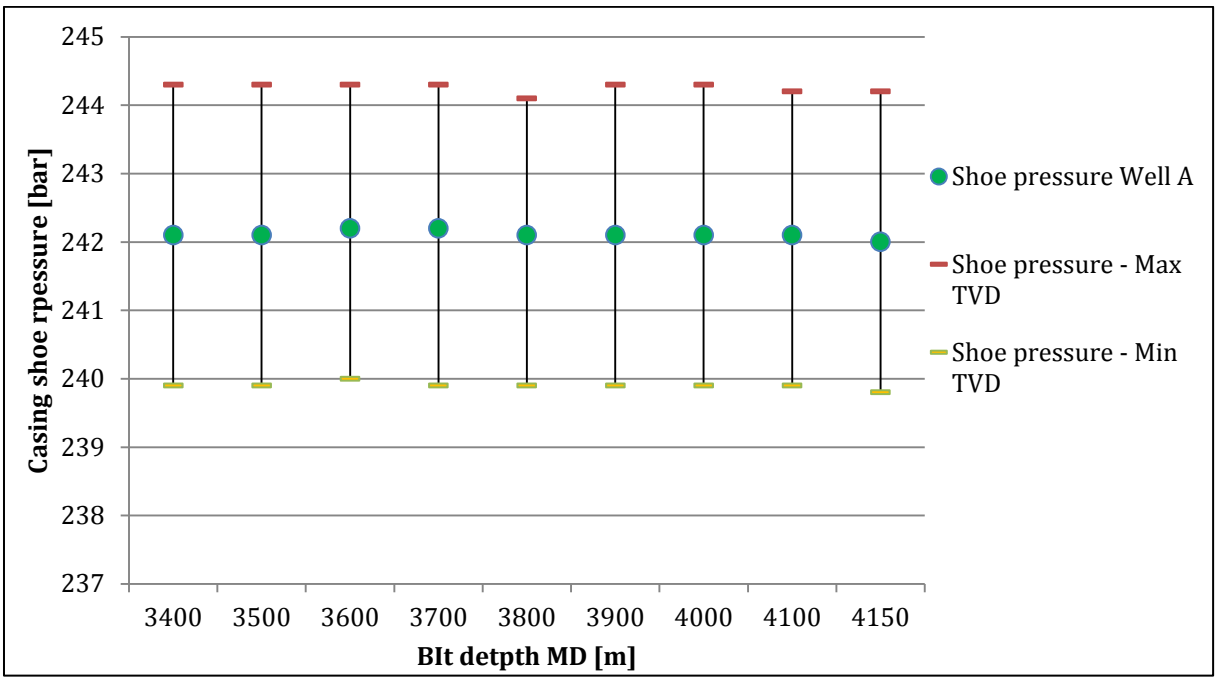

Figure 5.15: Development of 9⅝" casing shoe pressure

5.4.2 Effect of mud density uncertainty

In this section the combined effect of mud density uncertainty and wellbore position uncertainty will be analyzed. The analysis is performed by simulating the wellbore pressures for various mud densities related to the original, the maximum TVD and the minimum TVD trajectory. This simulation is repeated at three different circulation depths; 3400 m, 3700 m and 4150 m MD. Density is varied between 1,3 and 1,4 s.g, the original density at 50°C was 1,323 s.g. The other simulation parameters are as given in Table 5.3.

Figure 5.16 displays the casing shoe pressure as function of mud density. This figure only displays the casing shoe pressures recorded when circulating at 4150m, due to the small variance in casing shoe pressure as function of depth. Graphs representing values recorded at 3400 m and 3700 m will more or less overlap the ones given.

As expected, the mud density has a large influence on the wellbore pressure. The relationship between pressure and density also appears to be linear for all six data points between 1,3 and 1,4 s.g. A density increase by 0,02 s.g. corresponds to a pressure increase of approximately 3,3 bars. This increase is consistent for all mud weights at all three trajectories. The pressure effect by position uncertainty is only slightly affected by increasing mud density. At 1,3 s.g. position uncertainty accounts for a pressure uncertainty of ±2,2 bars, whereas at 1,4 s.g. the variance is ±2,3 bars.

To review the combined effects of both position and density uncertainty, assume the density uncertainty to be 0,02 s.g. and the position uncertainty as given. On the casing shoe pressure, this accounts for a maximum pressure uncertainty of ±5,6 bars. However, these uncertainties could compensate each other.

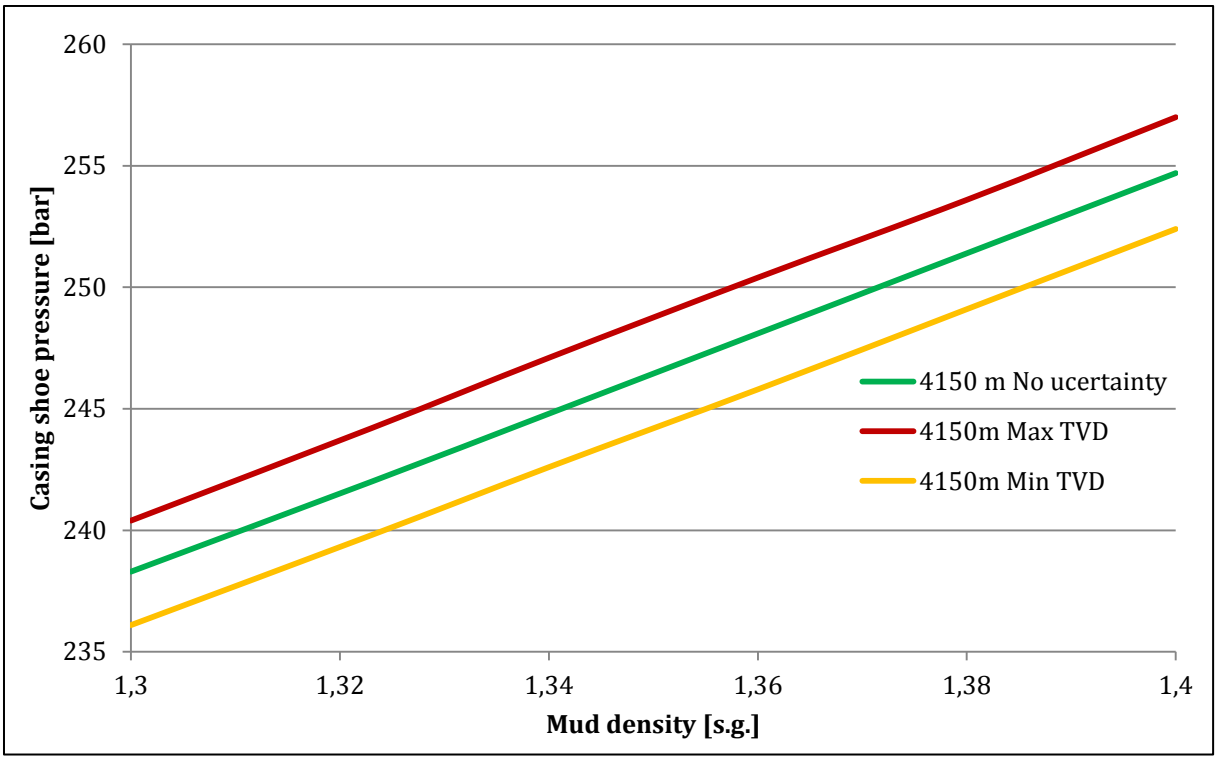

Figure 5.16: Casing shoe pressure as function of mud density. Circulation at 4150m MD

Figure 5.17 displays development of bottomhole pressure for various mud weights and circulation depths. The same linear relationship is observed here. The trend discussed above is emphasized in this figure. The effect of position uncertainty on bottomhole pressure increases both with depth and mud weight. At 3400m and 1,3 s.g. the pressure variance resulting from position uncertainty is ±2,2 bars. The corresponding variance at 4150m and 1,4 s.g is ±3,1 bars. The effect of density uncertainty increases with depth, but the slopes of all graphs are consistent. Effects of density uncertainty are accordingly not affected by the density itself.

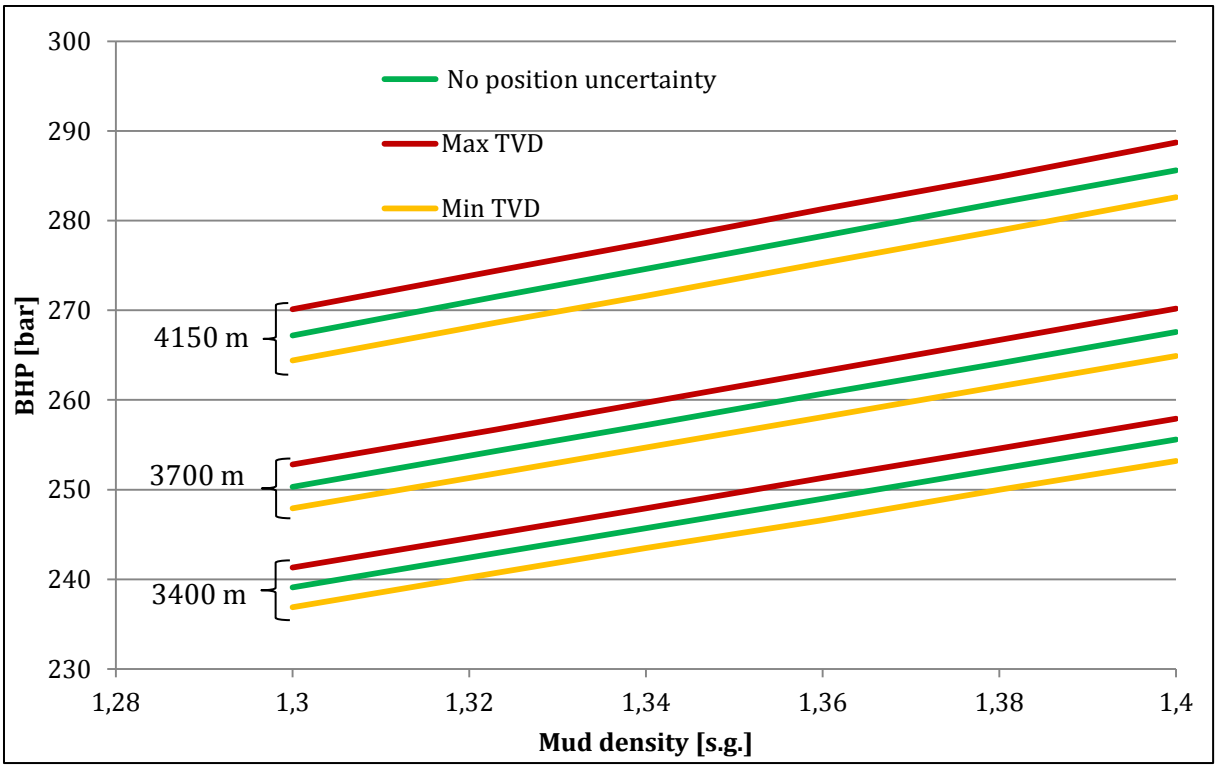

Figure 5.17: Effects of mud density- and wellbore position uncertainty on BHP

5.4.3 Effect of uncertainty in geo-thermal properties of formation rock

In this analysis, values of the specific heat capacity and the thermal conductivity of the formation were changed alternately. All the values were tested against both the minimum and maximum TVD trajectories. The other simulation parameters remain similar to the previous analyses.

Figure 5.18 shows the casing shoe pressure as function of formation properties. The red and green line represents the casing shoe pressures recorded with bottomhole depths of 4150m and 3400 m with maximum TVD. Similarly, the yellow and blue lines represent the minimum TVD trajectory. Once again the analysis shows that when all else equals, the shoe pressure is close to unaffected by the bit depth. It is also seen that the wellbore pressure to some degree is affected by the formation properties, however the extent does not appear to be great. When reviewing the graphs for the largest openhole section (4150 m), the variance between the two extremities is 0,8 bar for both trajectories. This value is only 0,1 bar larger than at 3400m.

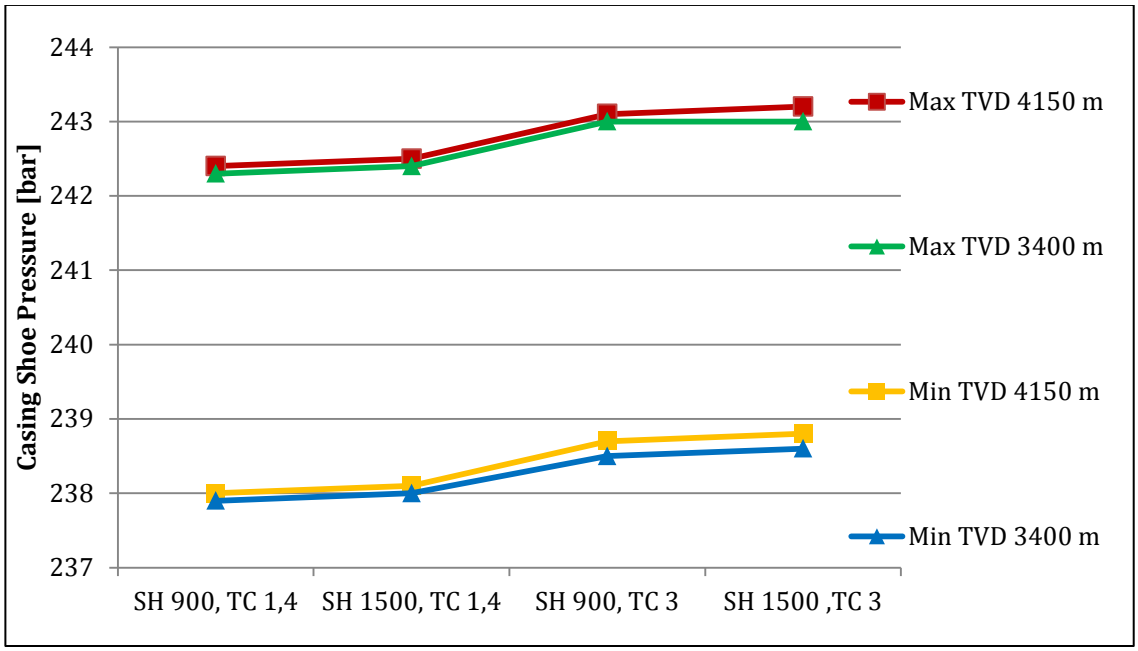

Figure 5.18: Casing shoe pressure as function of geothermal properties

Figure 5.19 and Figure 5.20 illustrates the change in bottomhole pressure as function of formation properties at depths of 3400m and 4150m respectively. Both cases show similar pressure variations as experienced on the casing shoe pressure. The variation between the highest and lowest point of a graph is approximately ±0,45 bars. This variation is consistent for both trajectories, at both depths. Most of the experienced pressure variations results from changing the thermal conductivity. Altering the specific heat capacity seems to hardly have any pressure effects at all. This result appears to be consistent both for high and low values of thermal conductivity, regardless of well depth.

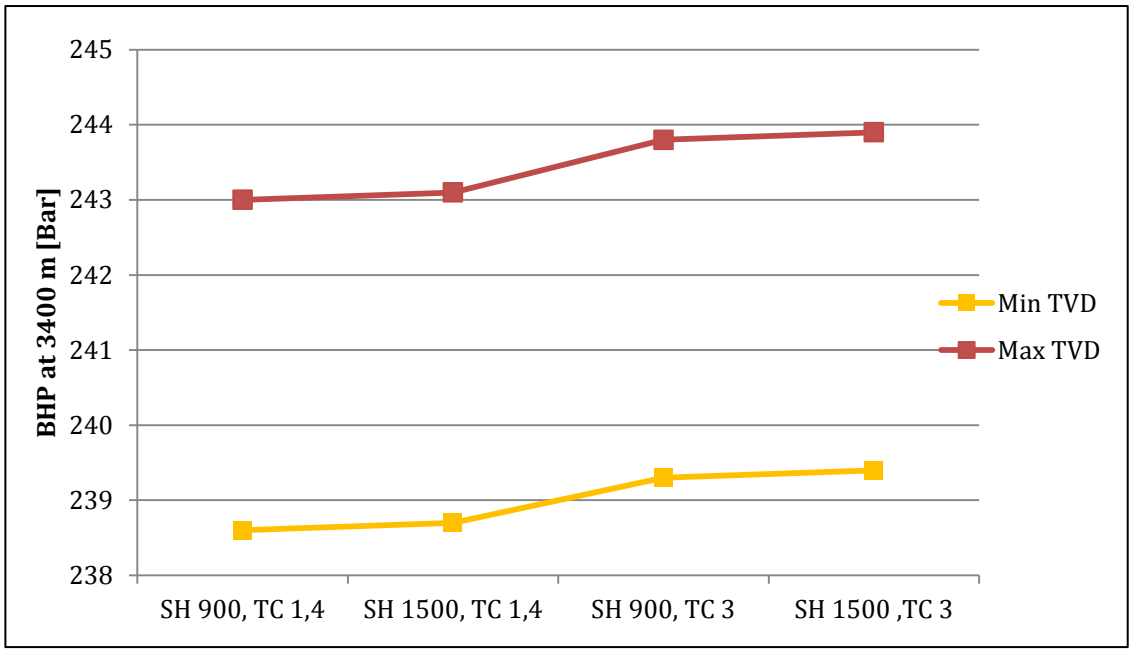

Figure 5.19: BHP as a function of geothermal properties at 3400m

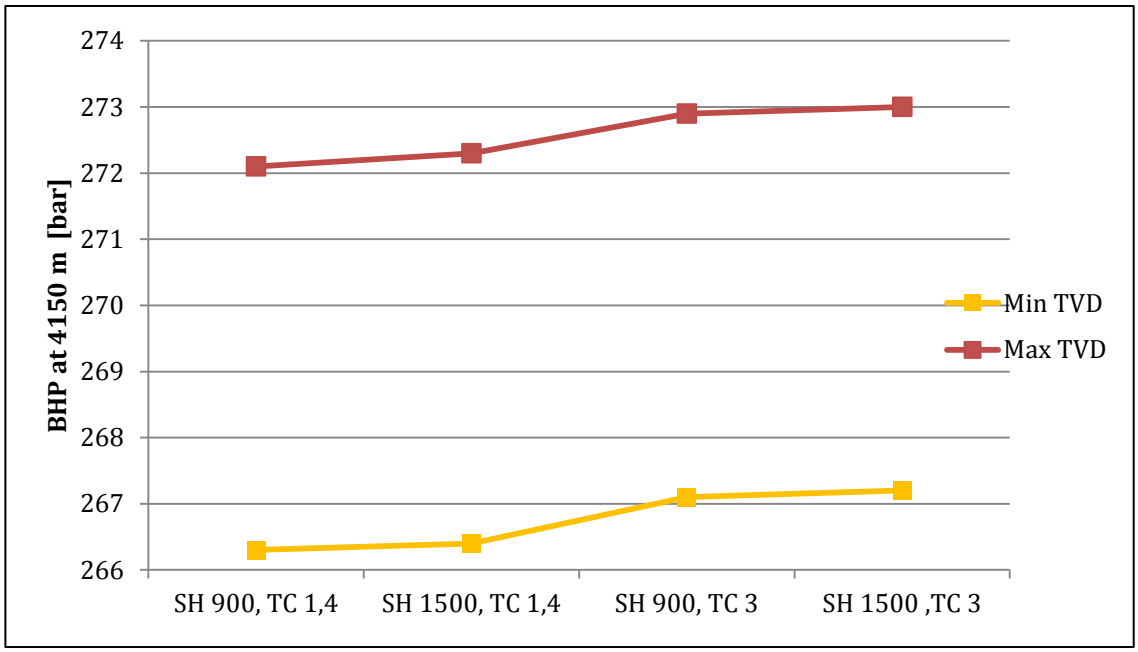

Figure 5.20: BHP as function of geothermal properties at 4150m

Figure 5.21 presents the BHP development as a function of time simulated time with SH = 1500J/kg·K and TC = 3 W/m·K. Graph a) and b) represents the minimum TVD trajectory when circulating at 3400m and 4150m respectively. Graph c) and d) represents the equivalent for the maximum TVD trajectory. Graphs obtained from simulations with other thermo-physical parameters are similar in appearance with small changes in the values.

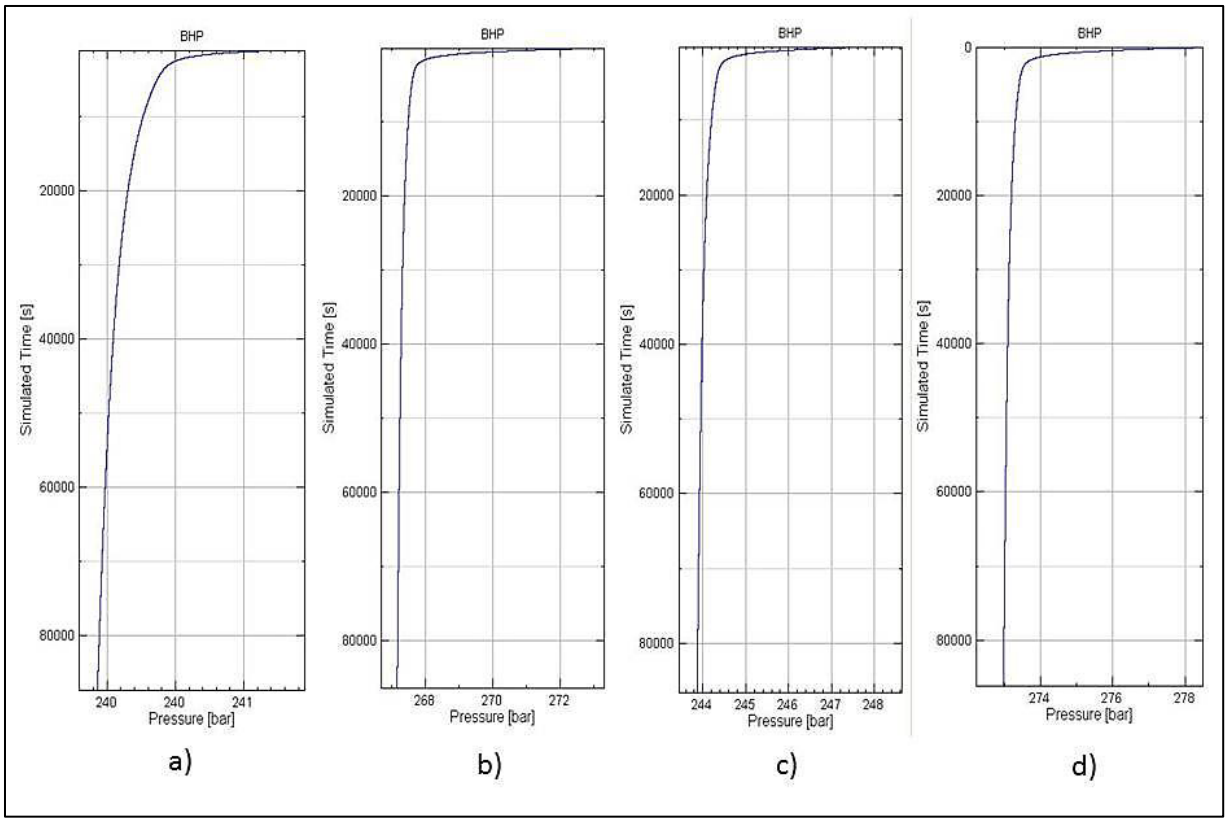

Figure 5.21: BHP development as a function of simulated time. SH = 1500 J/kg·K and TC = 3 W/m·K.

5.4.4 Effect of uncertainty in oil-water ratio of mud

In this analysis, the minimum and maximum TVD trajectories were simulated with oil-water ratios of 1, 3 and 5. The original value was 3,17. The other simulation parameters are as given in Table 5.3 and the results are displayed graphically below. Figure 5.22 presents the experienced variations on the casing shoe pressure. The red and green lines represents casing shoe pressures recorded at maximum TVD with bottomhole depths of 4150 m and 3400 m respectively. The yellow and blue lines are the equivalent for the minimum TVD trajectory. All graphs show that increasing the oil - water ratio from 3 to 5, have very little or no effects on pressure. However, when decreasing the oil-water ratio from 3 to 1 a pressure decrease of more than 1 bar is observed at minimum TVD. A slight pressure increase at maximum TVD is observed on the same interval. This is a peculiar result, but it is consistent for all the simulations performed. An additional simulation was also performed with the minimum TVD trajectory at 4150 m with oil – water ratio of 1, to verify if these results were consistent or only random noise experienced from the simulator. The second simulation showed the exact same result, with accuracy within one tenth of a bar.

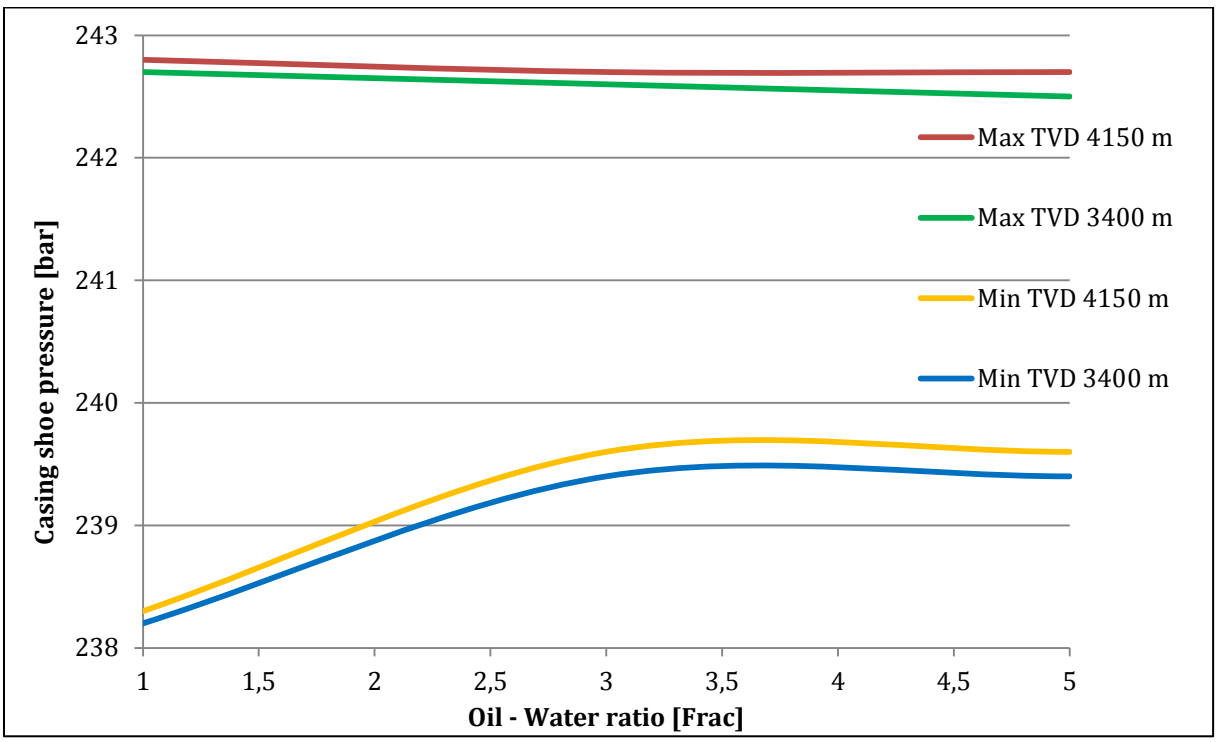

Figure 5.22: Casing shoe pressure as function of oil-water ratio

Figure 5.23 and Figure 5.24 displays the variation in bottomhole pressure as function of oil – water ratio at 3400m and 4150m respectively. The red and yellow lines represent the maximum and minimum TVD trajectory. The results are similar as discussed above. The effect of position uncertainty increase as the oil – water ratio decreases from 3 to 1, but remains unaffected by an increase from 3 to 5. This is consistent at both the simulated well depths.

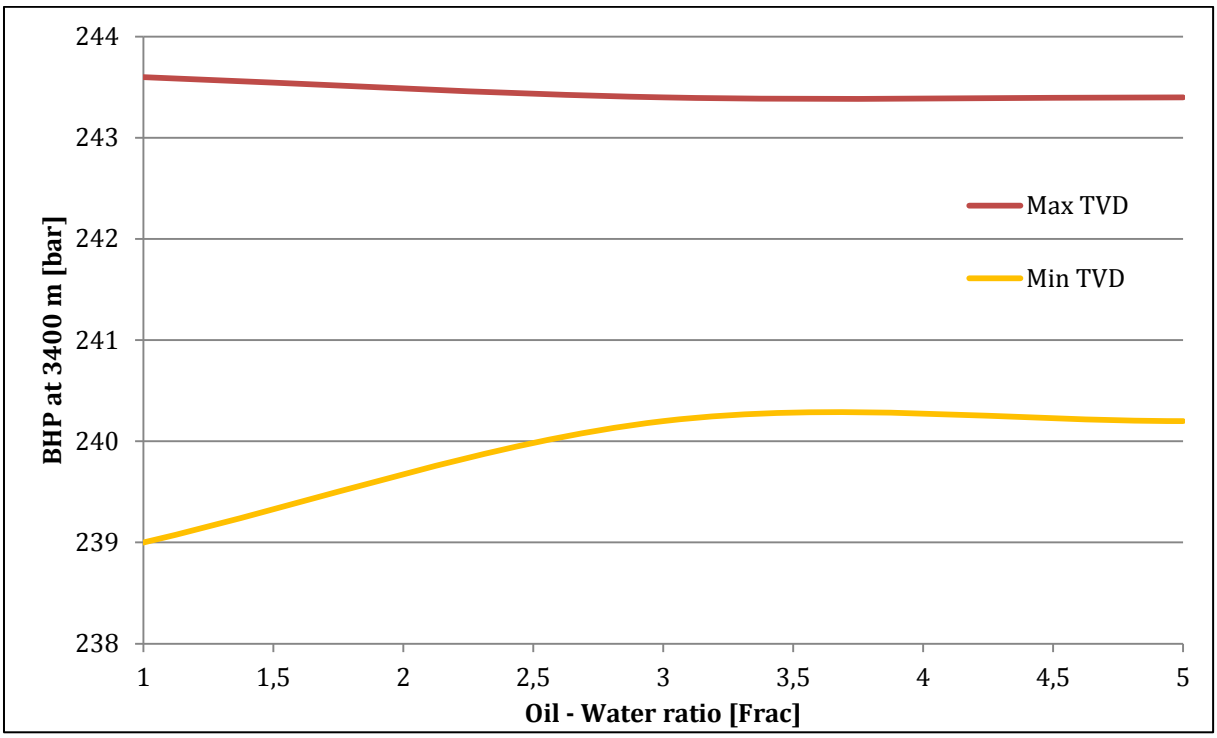

Figure 5.23: BHP as function of oil-water ratio at 3400m

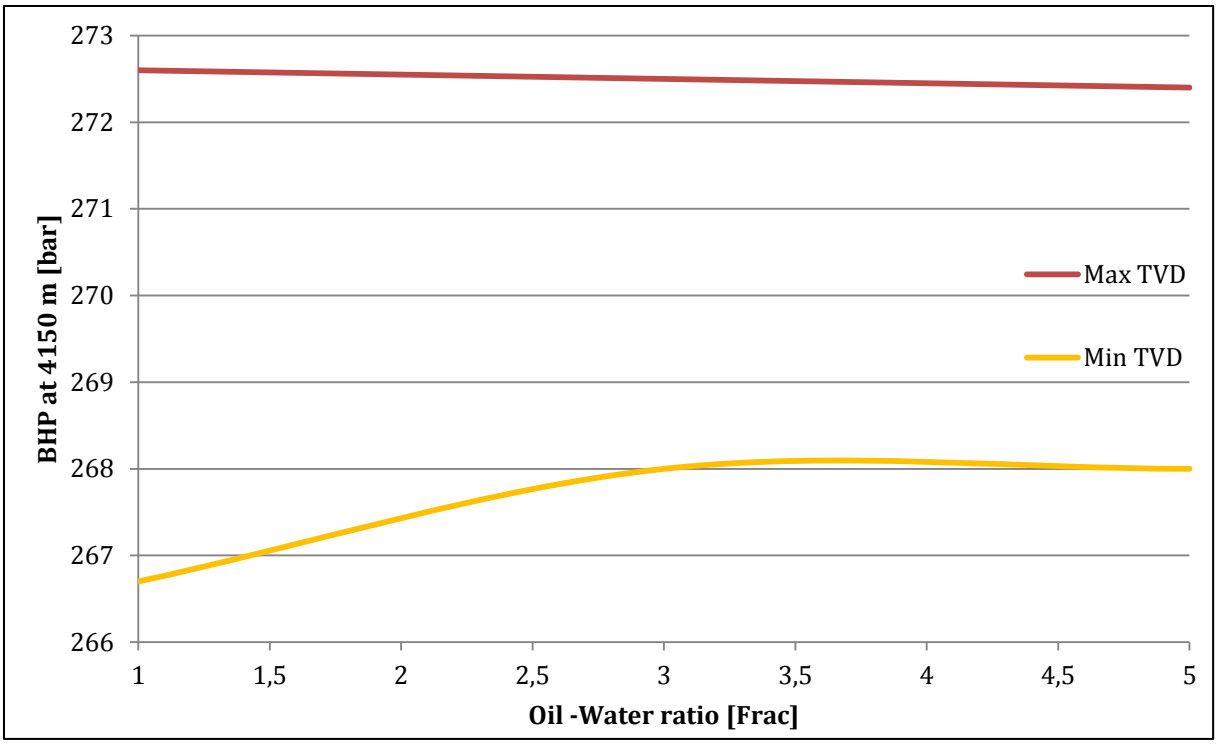

Figure 5.24: BHP as function of oil-water ratio at 4150m

5.5 Case 2 – Well B 12¼" section

Table 5.4 displays the simulation parameters for the 12¼" section of well B. When possible these data are taken directly from the operators drilling program and from the daily drilling reports (DDR), provided by the drilling contractor. Notice the high flow rates and high surface rotation used in this well. High flow rates were necessary to ensure sufficient hole cleaning. The high surface rotation speed was chosen to have an acceptable ROP. Low gear and lower rotation speed with higher WOB was attempted, but this only resulted in large stick-slip which is very unfortunate for downhole equipment. Tabulated data for case 2 is presented in appendix 9.4.

Table 5.4: Simulation parameters for well B - 12¼" section

13⅜" casing depth	4277	m
Sensor location	4280	m
Air temp	5	°C
Surface rotation	180	rpm
Simulated time	1000/86400	s
Flow rate	3300	l/min
Specific heat capacity of formation	900	J/kg·K
Thermal conductivity of formation	2	W/m·K
Geothermal Gradient	3,6	°C/100m
Mud temp	50	°C
Mud density at temperature	1,56	s.g.
Oil – Water ratio	1,564	
Specific heat capacity of mud	1526,4	J/kg·K
Thermal conductivity of mud	0,51	W/m·K

5.5.1 Effect of wellbore position uncertainty isolated

Analysis of the pressure effects experienced by isolating wellbore position uncertainty was performed in steps of 200 m for all three trajectories. In Figure 5.25 the bottomhole pressures are shown together with the pore, fracture and collapse pressure gradients. At the start of the section only a small variance of ±0,06 bar is experienced. However this consistently increases with depth, reaching ±4,9 bars at 6500m. The margins in the well are large, however around 3000 m the minimum bottomhole pressure comes fairly close to the collapse pressure. The estimated margin at this point is 0,01 s.g or 3,6 bars.

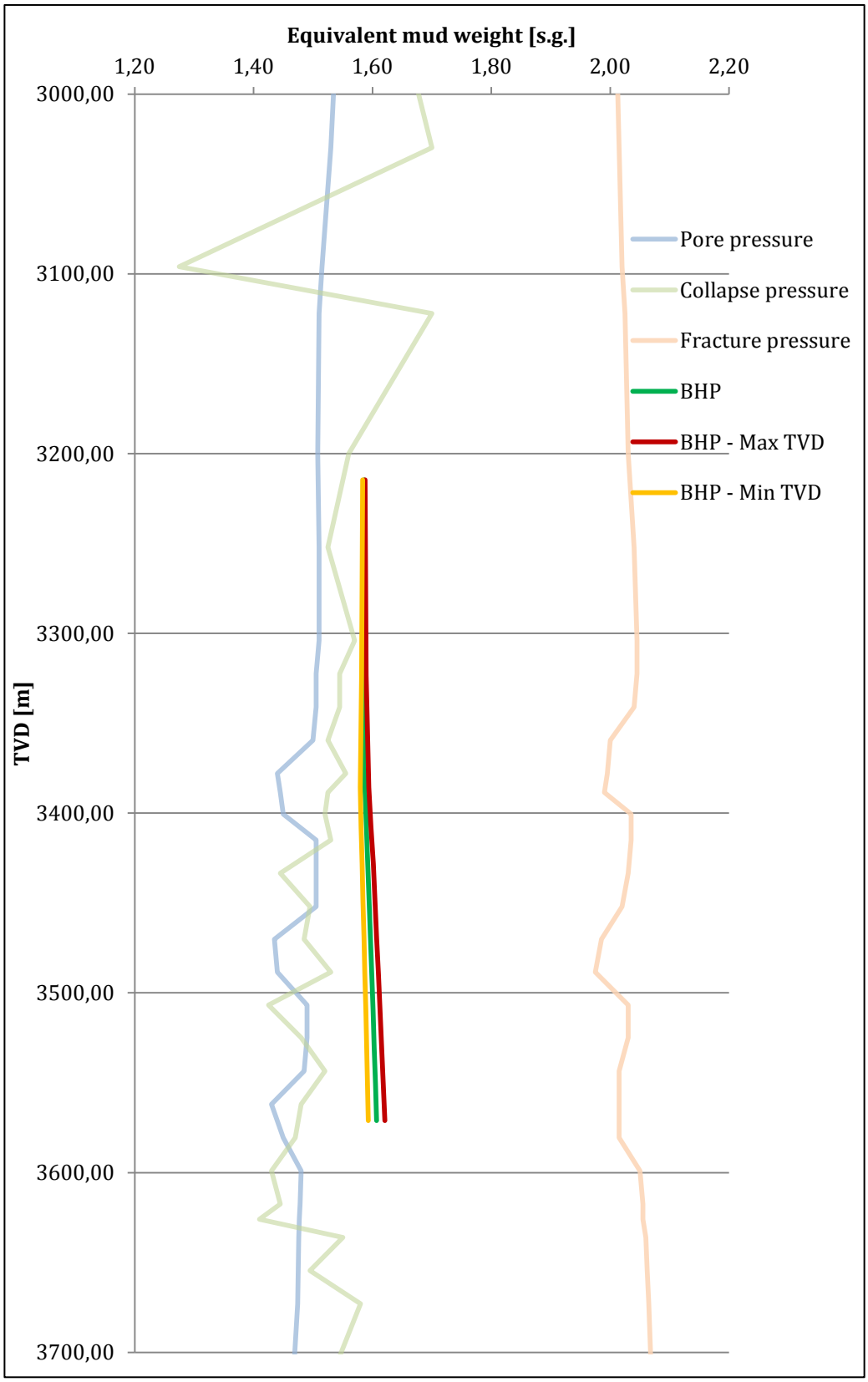

Figure 5.25: BHP displayed together with pressure gradients as function of depth

Figure 5.26 displays the development of the pressure just below the 13⅜" casing shoe as the well depth increases progressively. Compared to the results of well A, there is a significant pressure increase with depth. Within the same trajectory a difference of 3,6 bars is experienced between the values recorded at 4300 and 6500 m. Position uncertainty accounts for an additional minor difference of ±0,5 bar throughout the section.

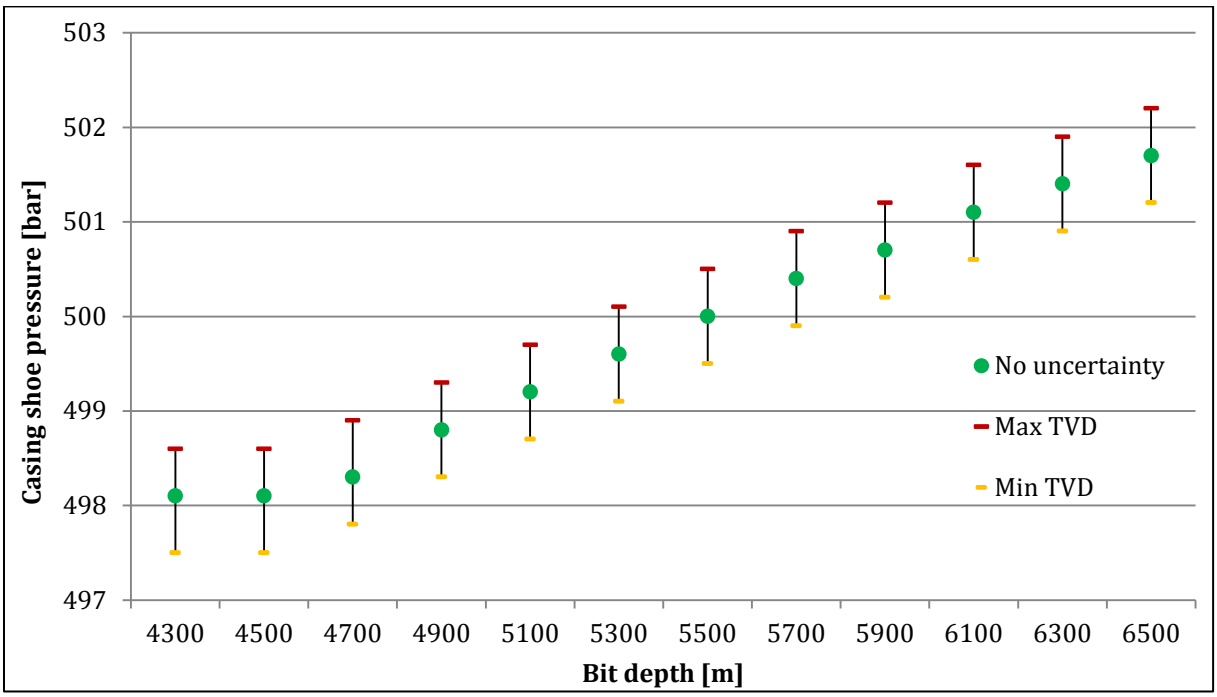

Figure 5.26: Development of 13⅜" casing shoe pressure

5.5.2 Effect of mud density uncertainty

Analysis of mud density uncertainty as a result of formation influxes, cuttings transport etc. was performed by varying the simulated density between 1,5 and 1,6 s.g. All other simulation parameters remain constant during the analysis. The analysis was performed with four different depth settings throughout this section; 4300, 5000, 5700 and 6500 m.

Figure 5.27 displays how the bottomhole pressure is affected by uncertainties in mud density. The red, yellow and green lines represent the maximum TVD, minimum TVD and original trajectories. The bottomhole pressure is displayed in four groups regarding at what depth it is recorded. Given the depth at which these pressures are recorded, the mud density is bound to have a large impact. The results are otherwise similar to those experienced from well A. For a given trajectory, the mud density variation has a linear relationship with pressure. It is also observed that the effect of wellbore position uncertainty gets progressively larger both with increasing mud weight and depth. A density increase of 0,02s.g corresponds to a consistent pressure increase of 6,4 bars at 4300 m and 7,2 bars at 6500 m.

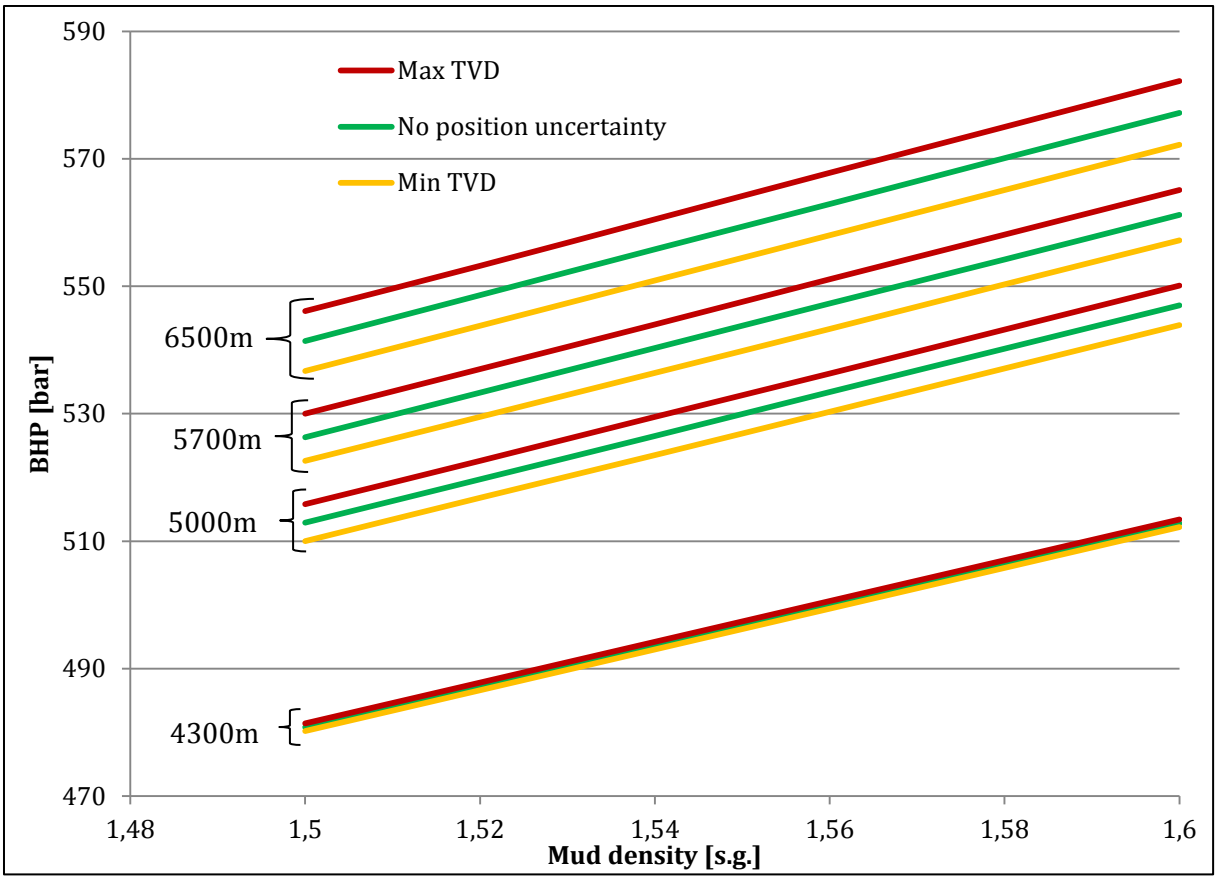

Figure 5.27: Effects of mud density- and wellbore position uncertainty on BHP

Figure 5.28 displays the variation in the casing shoe pressure as function of mud weight and wellbore position uncertainty for bottomhole depths of 4300 m and 6500 m. For illustrational purposes, this figure does not include graphs recorded from the intermediate depth settings. These would be located in-between the two displayed groups.

The graphs show the same characteristics as above. Mud weight appears to have a near perfect linear relationship with pressure. It is however noticed that in this case neither mud weight nor bit depth influences on the effects of wellbore position uncertainty. A 0,02 s.g. pressure increase results in a consistent 6,4 bar pressure increase.

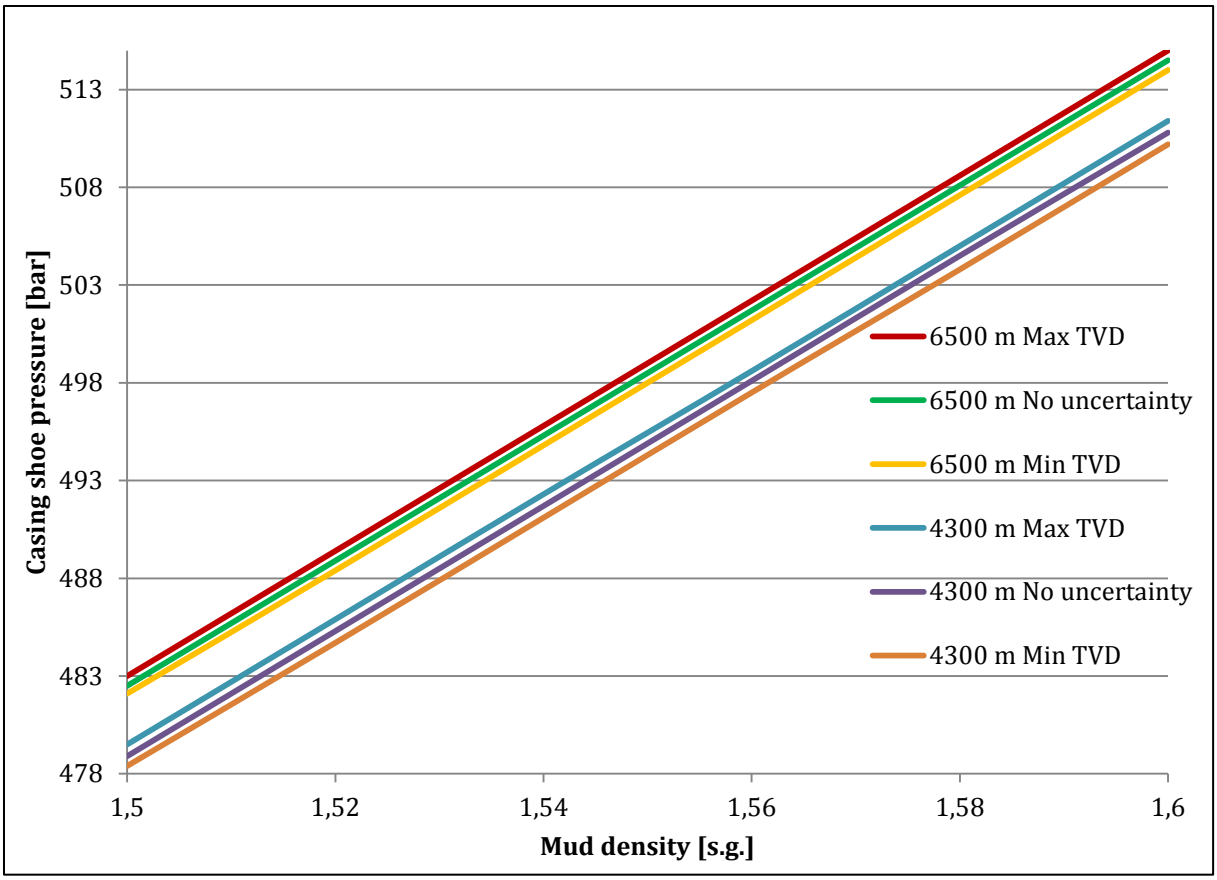

Figure 5.28: Effects of mud density- and wellbore position uncertainty on casing shoe pressure

5.5.3 Effect of uncertainty in geothermal properties of formation rock

The analysis of uncertainty in geothermal properties of formation rocks was conducted with the same values for specific heat capacity and thermal conductivity as for well A. The other simulation parameters are as given in Table 5.4, with 24 hours of simulated time.

Graphical displays of the data are given below. Figure 5.29 shows the variation in casing shoe pressure. At first sight the variations seems to be larger in this case compared to well A. There are also larger separations between all graphs, however this is mostly due to the depth and depth uncertainty of the well. All graphs displays a variance of approximately 1,2 bars. In comparison, this is 0,4 bars more than what was observed in well A. The overall effect on casing shoe pressure is not affected by depth, however the influence by formation specific heat capacity increases. At 4300 m changes in specific heat capacity has hardly any influence, whereas at 6500 m, larger influences are experienced. Assumingly, this should result in a larger overall pressure variation, but at this depth the influence of thermal conductivity has decreased giving identical results.

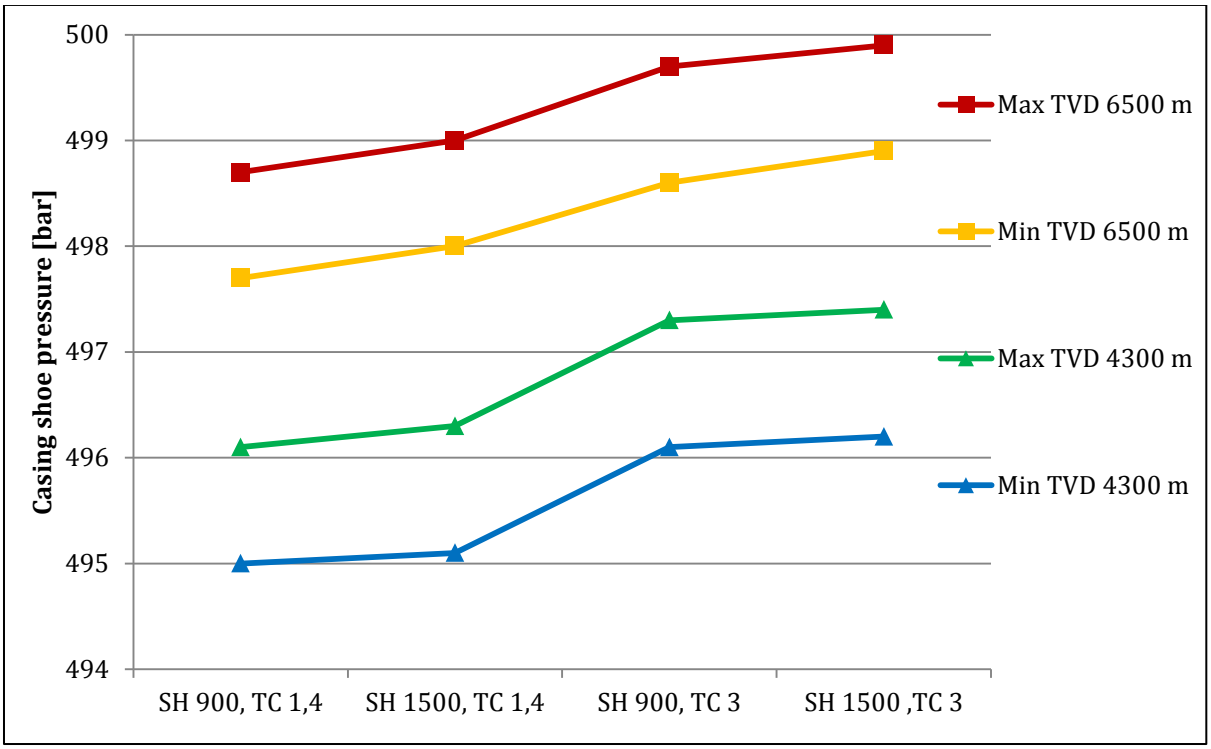

Figure 5.29: Casing shoe pressure

Figure 5.30 and Figure 5.31 displays the variation in bottomhole pressure at 4300 and 6500 m respectively. A distinctive difference is observed between these two diagrams. At 4300 m thermal conductivity is dominating. The total pressure variance is 1,3 bars regardless of position uncertainty. At 6500 the effect of alterations in specific heat capacity has increased while influence by thermal conductivity has decreased. This supports the findings above and results in a linear approximation of the data samples. As reasonably expected, the pressure variation is larger at 6500 m that at 4300 m. However, at 6500 m the pressure variation is 0,3 bars larger at minimum TVD. This is an unexpected result. As an absolute value this is not a lot, but significant when considering the otherwise small variations. With logical reasoning it is expected to obtain the largest variation on the deepest trajectory. Such result could suggest a bias in the simulator.

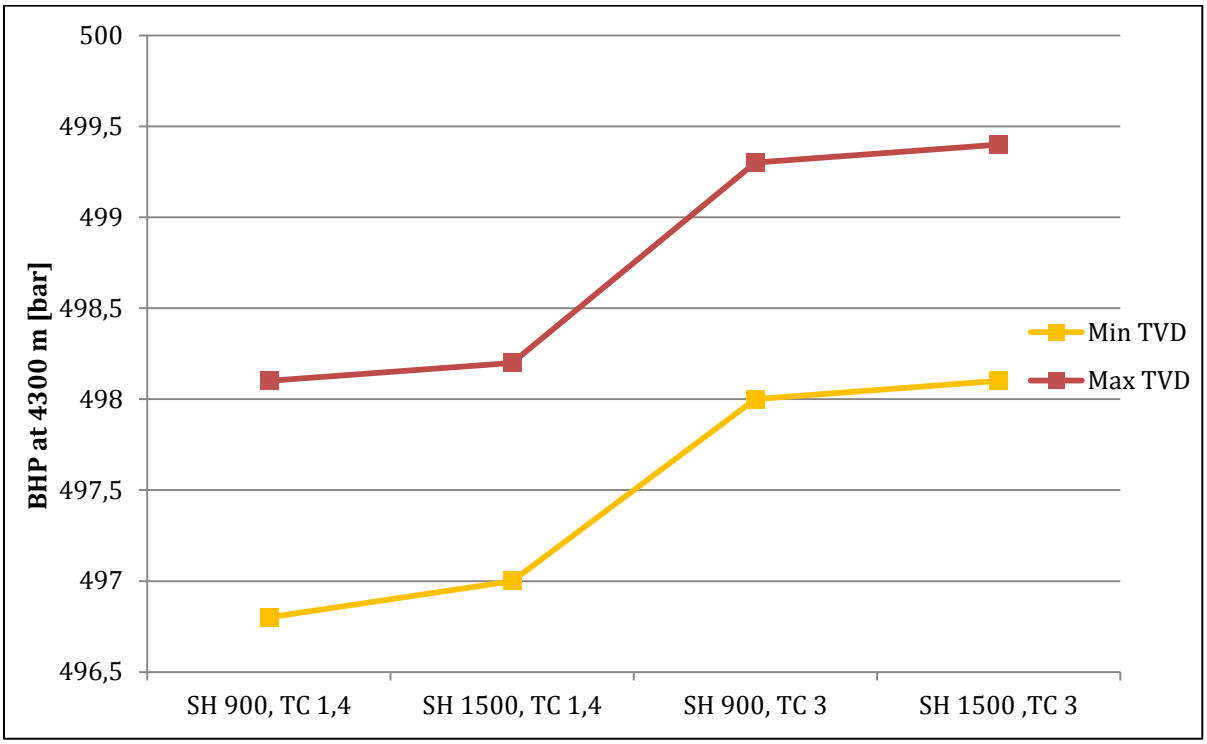

Figure 5.30: Bottomhole pressure at 4300 m MD

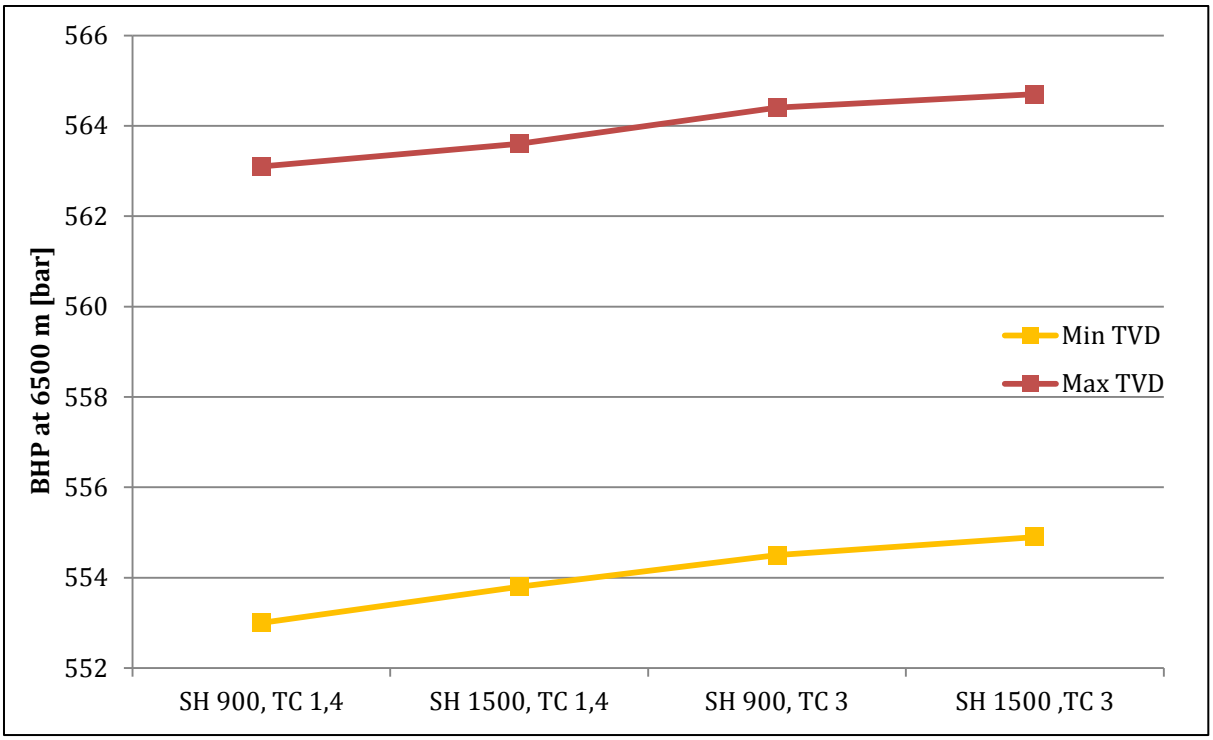

Figure 5.31: Bottomhole pressure at 6500 m MD

5.5.4 Effect of uncertainty in oil-water ratio of mud

Analysis of uncertainty in the oil-water ratio was performed for the minimum and maximum TVD trajectory at both 4300 m and 6500 m. The oil – water ratio was alternated between 1, 2 and 3. The original value was 1,564.

Figure 5.32 displays casing shoe pressure as function of oil – water ratio. Some pressure variations are observed, however these appear to be non-consistent. At 4300 m, a decrease in the oil – water ratio from 1,5 to 1 results in a pressure increase on both trajectories. At 6500 m a slight decrease is observed on the same interval. Increasing the ratio past 1,5 have different results on all graphs.

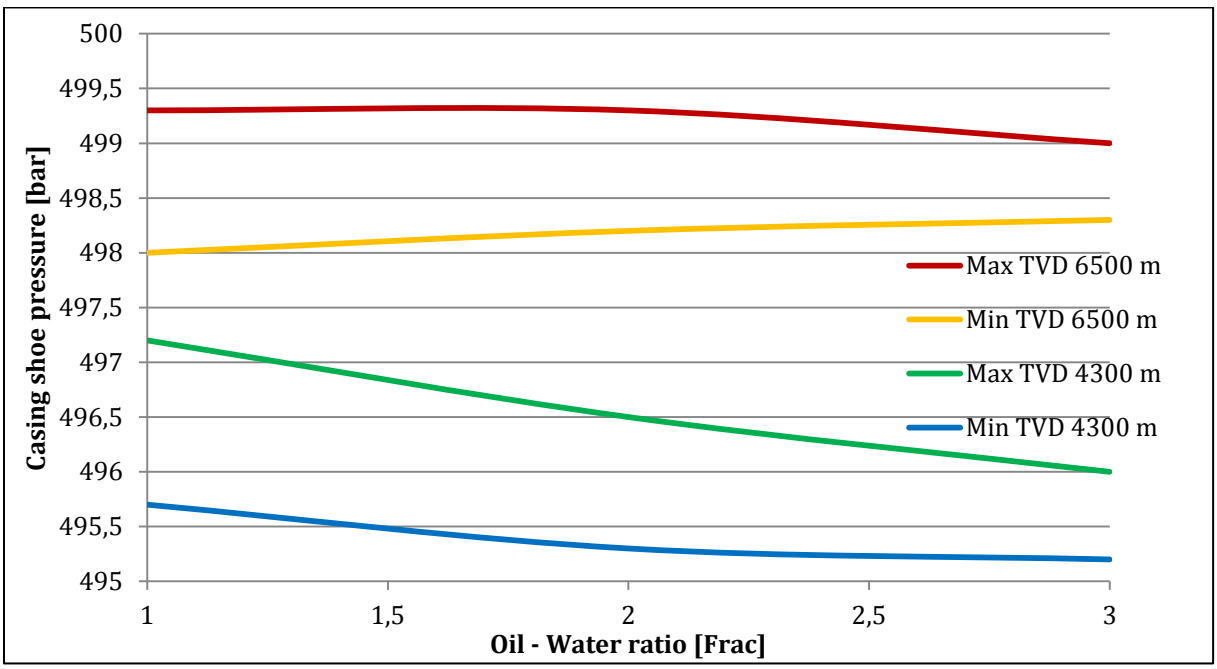

Figure 5.32: Casing shoe pressure as function of oil-water ratio

Inconsistent variations are also observed on the bottomhole pressure displayed in Figure 5.33 and Figure 5.34. The trend at 4300 m suggests that a decrease in the oil – water ratio, increases the pressure and vice versa. The same trend does not apply at 6500, where the opposite is observed at minimum TVD. Any change at this depth is either way dominated by the effect of position uncertainty.

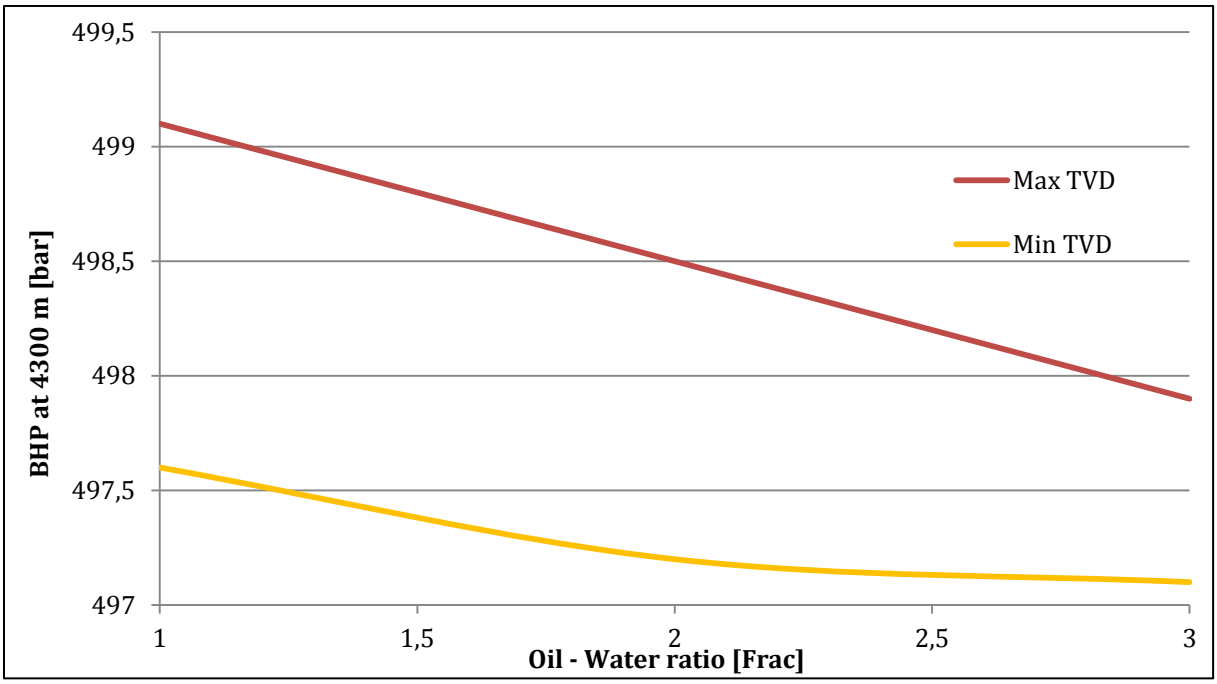

Figure 5.33: BHP as function of oil-water ratio at 4300m

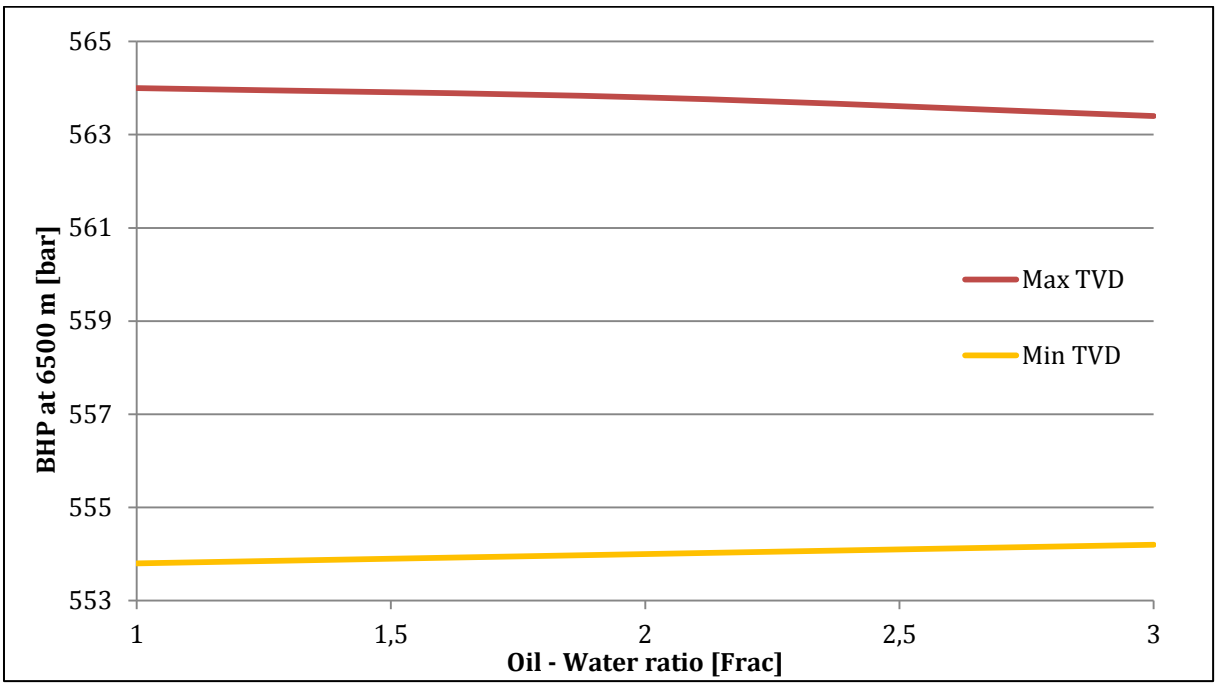

Figure 5.34: BHP as function of oil-water ratio at 6500m

5.6 Case 3 – Well B 8½" section

Case 3 presents the analysis of the 8½" or second to last section of well B. There are a number of changes to the simulation parameters from the previous case. The flow rate is reduced to 2000 l/min and the surface rotation speed is reduced to 120 rpm. A new mud is used with a density of 1,68 s.g. at 60°C, which is the recorded mud temperature. The remaining simulation parameters are given in Table 5.5 below. Results are tabulated in appendix 9.5.

Table 5.5: Simulation parameters - case 3

9⅝" casing depth	6500	m
Sensor location	6500	m
Air temp	10	°C
Surface rotation	120	rpm
Simulated time	1000/86400	s
Flow rate	2000	l/min
Specific heat capacity of formation	900	J/kg·K
Thermal conductivity of formation	2	W/m·K
Geothermal Gradient	3,6	°C/100m
Mud temp	60	°C
Mud density at temperature	1,68	s.g.
Oil - Water ratio	5,25	
Specific heat capacity of mud	1061	J/kg·K
Thermal conductivity of mud	0,39	W/m·K

5.6.1 Effect of wellbore position uncertainty isolated

Analysis of the pressure effects by wellbore position uncertainty was performed similarly as for the previous cases. Values were recorded from all three trajectories in steps of 200 m, starting at 6600 m and ending at 8250 m.

In Figure 5.35 the bottomhole pressure gradients in s.g. are plotted as function of depth, along with the pore, collapse and fracture pressure gradients. The graph display how the variance in bottomhole pressure first increases up to 3700m before it decreases until TD. The maximum recorded pressure variance of 7,1 bars was observed at 7600 m MD, between the original and minimum TVD trajectory. The corresponding variance between the original and maximum TVD trajectory was 6,6 bars. This non-uniform variance is observed throughout the whole section.

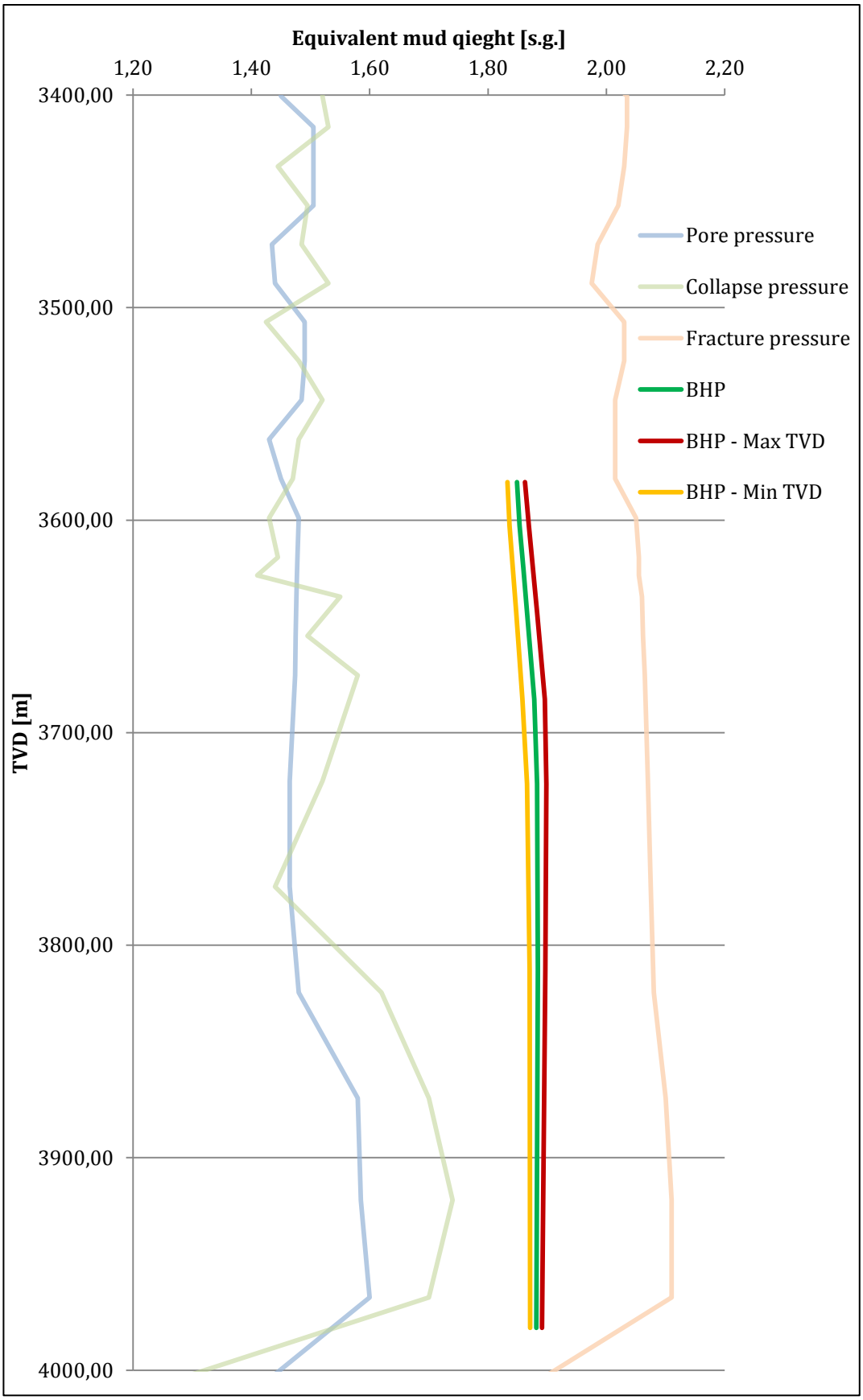

Figure 5.35: BHP displayed together with pressure gradients as function of depth

In Figure 5.36 the development of the 9⅝” casing shoe pressure is presented. The same non-uniform measurments are experienced here, however the pressure variance exeeds ±5 bars when only position uncertainty is considered. This is consistent for all measurements. Larger variances resulting from circulation depth is also experienced. A 5,7 bar pressure difference is experienced between the deepest and shallowest point of the same trajectory. Combining this with the position uncertainty, gives variances approaching ±8 bars.

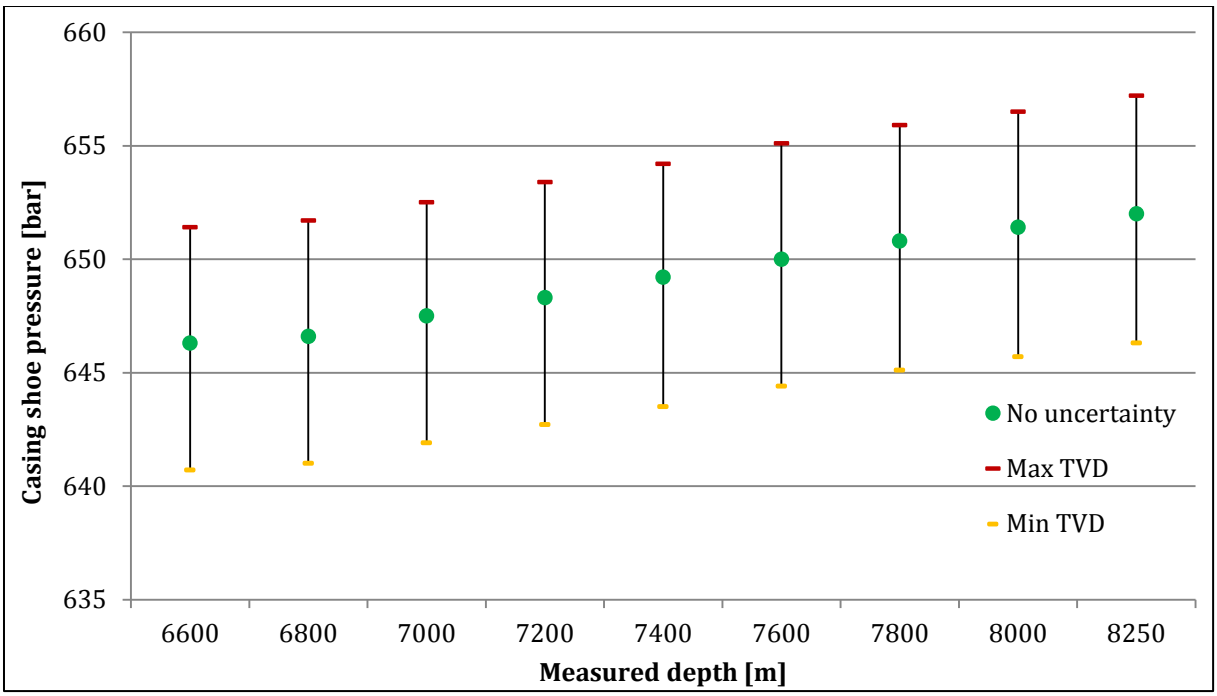

Figure 5.36: Development of 9⅝” casing shoe pressure

5.6.2 Effect of mud density uncertainty

Analysis of pressure effects by mud density uncertainty was performed with mud densities ranging from 1,64 to 1,72 s.g. about the original density of 1,68 s.g. Simulations were perform at three different depth settings; 6600, 7400 and 8250 m.

In Figure 5.37 the bottomhole pressure is shown as function of mud density for all three trajectories at the three different depths settings. Similar to the other cases, the mud density has a linear relationship with bottomhole pressure with no significant deviation. Slope of the graphs is slightly increasing with depth. A 0,02 s.g. density increase corresponds to a pressure increase of 7,7 bars at 6600 m. At 8250 the pressure equivalent increase is 8,7 bars. The effect of position uncertainty increases from 6600 to 7400 m, but then decreases to 8250m. Mud density does not affect the influence by position uncertainty.

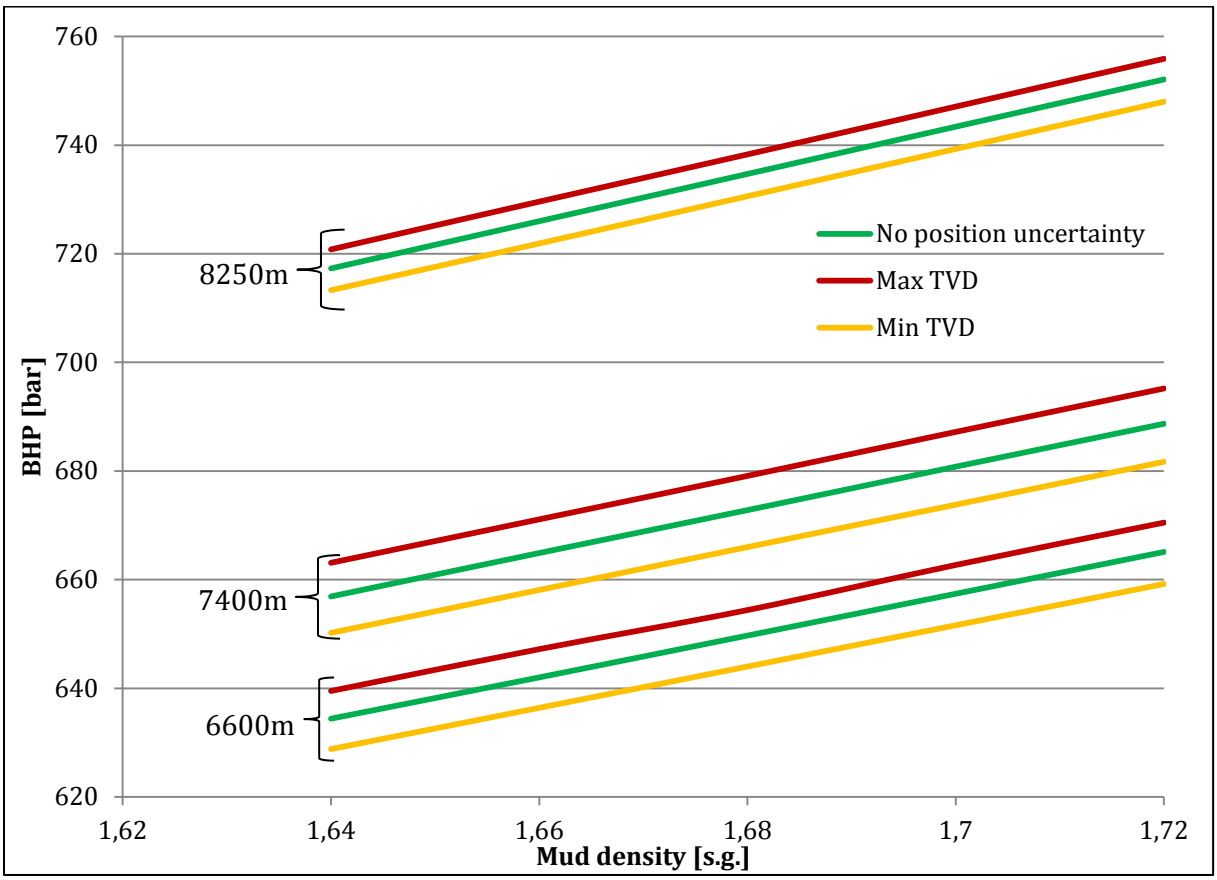

Figure 5.37: Effects of mud density- and wellbore position uncertainty on BHP

In Figure 5.38 the 9⅝” casing shoe pressure is displayed as function of mud density. The red, green and yellow lines represent the maximum TVD, original and minimum TVD trajectory with bottomhole depth of 8250m. The grey, purple and brown lines are the equivalent for bottomhole depth of 6600 m. Increasing the mud density by 0,02 s.g. corresponds to an increase of approximately 7,7 bars on the casing shoe pressure. This increase is consistent for all trajectories, depths and mud weights.

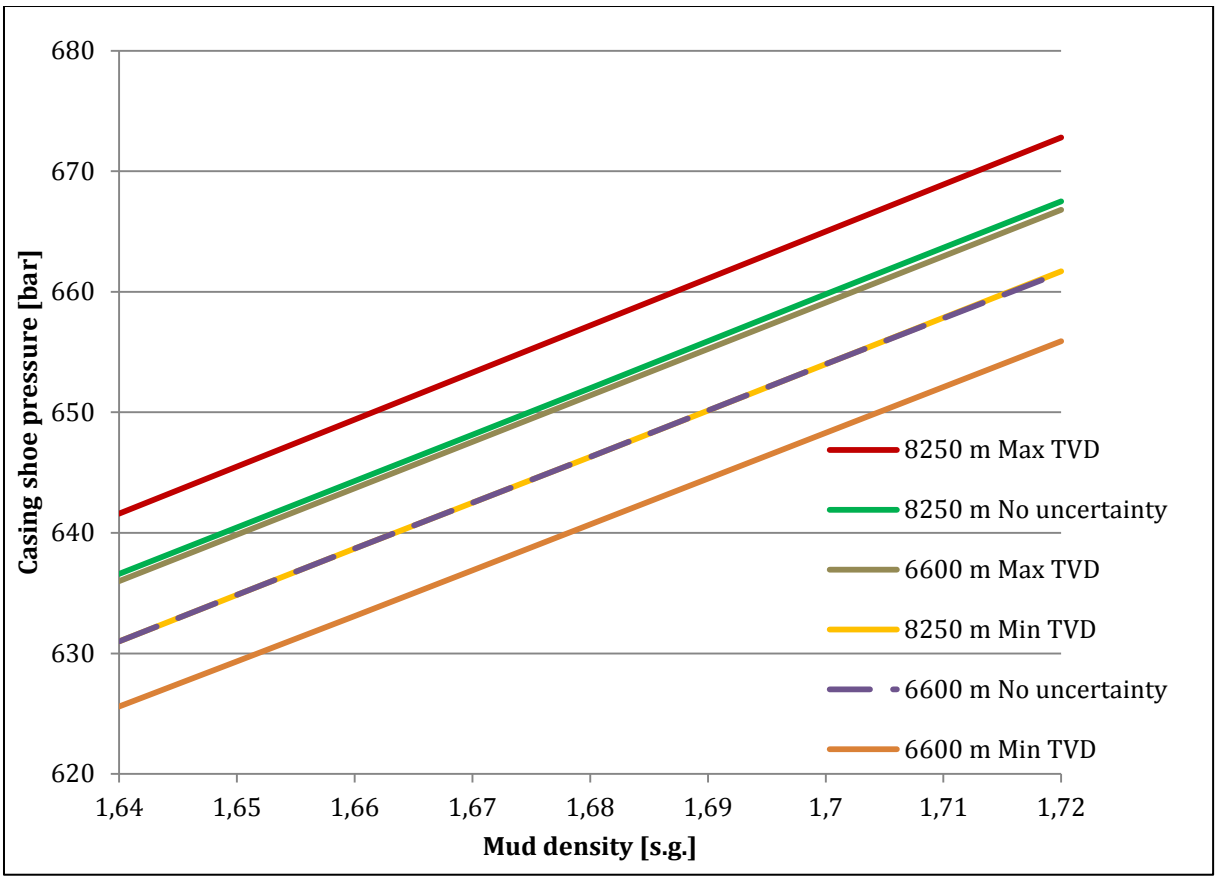

Figure 5.38: Effects of mud density- and wellbore position uncertainty on casing shoe pressure

5.6.3 Effect of uncertainty in geothermal properties of formation rock

Analysis of uncertainty in geothermal properties was performed with the same values for specific heat capacity and thermal conductivity as the previous cases. The two depth settings used in these simulations were 6600 and 8250 m.

Figure 5.39 displays the variation in casing shoe pressure. The red and yellow lines represent the maximum and minimum TVD trajectory with bottomhole depth of 8250m. The green and blue lines are the equivalent for bottomhole depth of 6600m. The pressure variations experienced as a result of geothermal properties are relatively small, only averaging ±0,5 bars. The graphs now display a linear approximation, not dominated by thermal conductivity. This coincides with the trend observed from case 2.

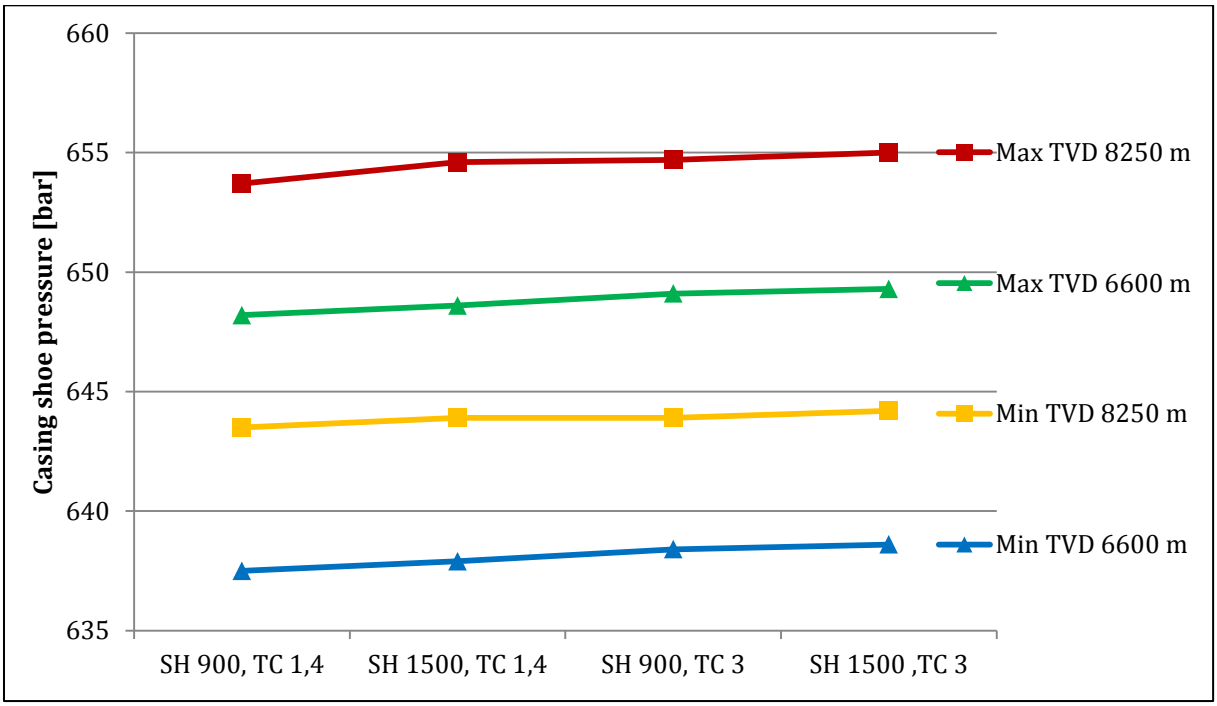

Figure 5.39: Casing shoe pressure

Figure 5.40 and Figure 5.41 displays the variation on bottomhole pressure at 6600 and 8250 m respectively. The pressure variations are small, but consistent. Only small deviations from linearity occur. The average variance experienced on bottomhole pressure is ±0,9 bar at 8250m and ±0,5 bar at 6600m.

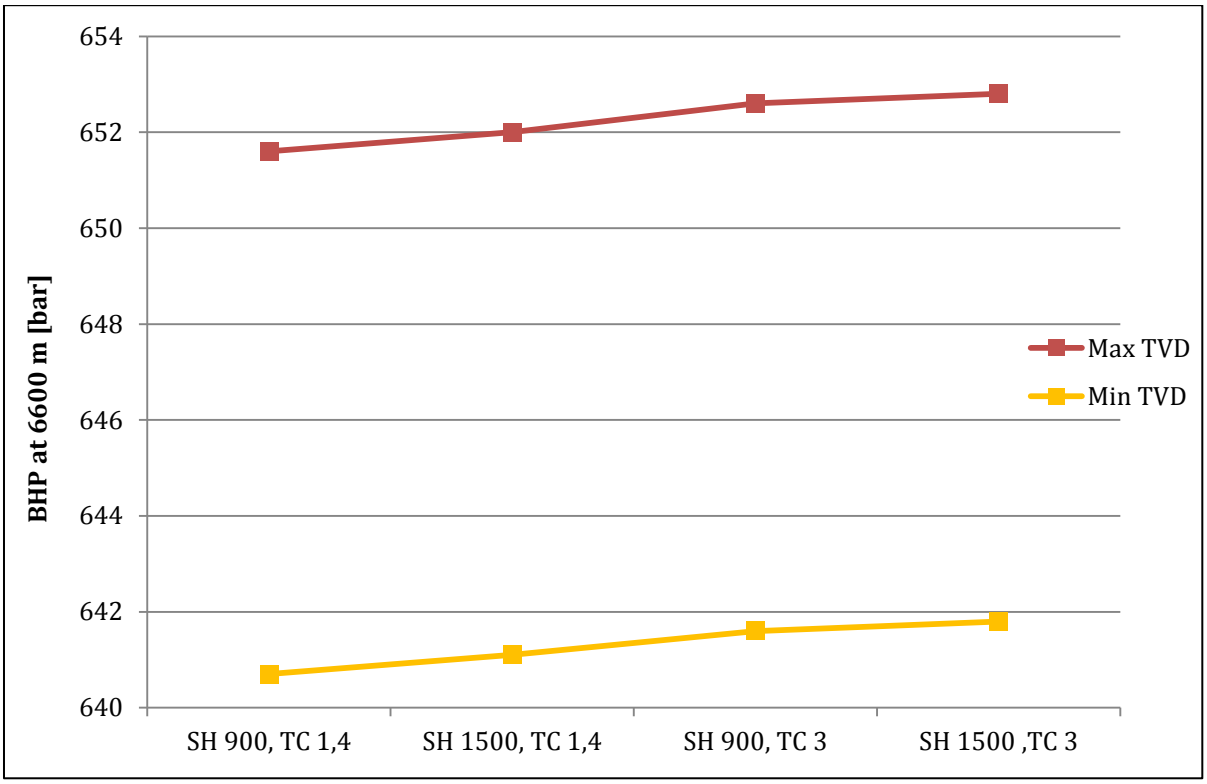

Figure 5.40: Bottomhole pressure at 6600 m MD

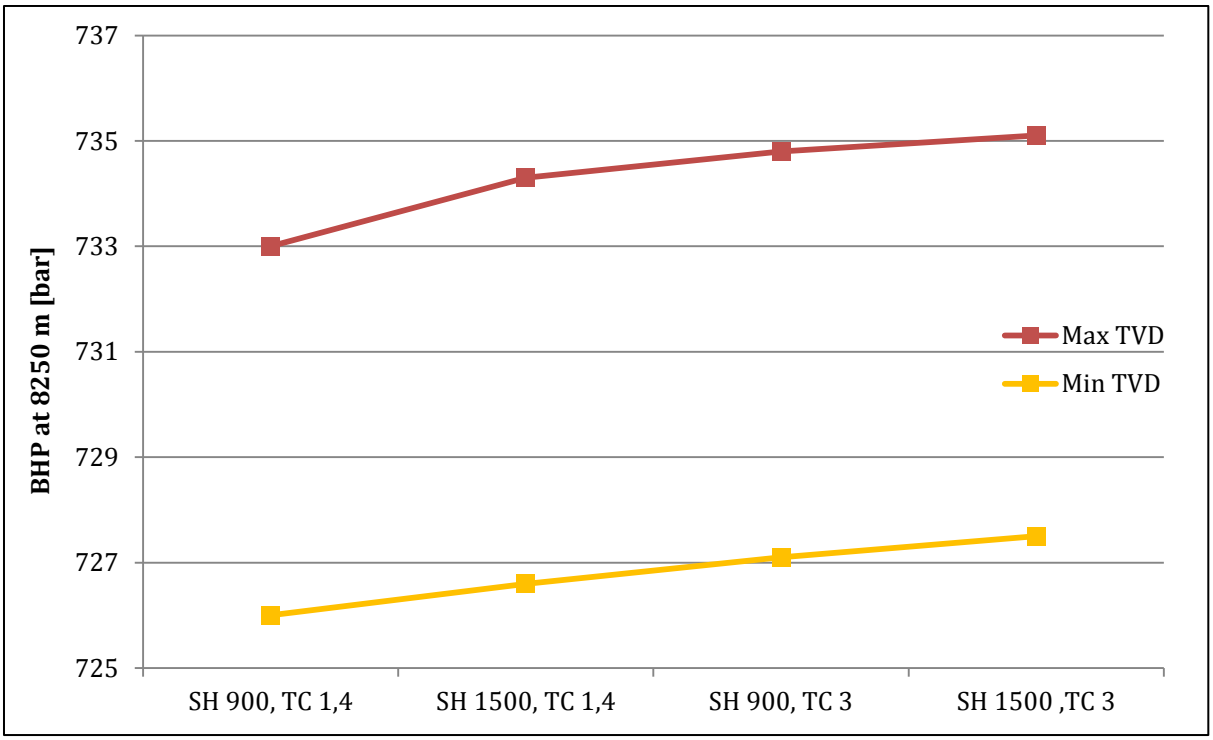

Figure 5.41: Bottomhole pressure at 8250 m MD

5.6.4 Effect of uncertainty in oil-water ratio of mud

The mud used for drilling this section had an original high oil – water ratio of 5,25. The simulations were performed with values between 3 and 7. Figure 5.42 shows how only small, but consistent variations occur on the casing shoe pressure. All simulations show that decreasing the oil-water ratio from 5 to 3 results in a small decrease in pressure. Increasing the ratio from 5 to 7 has hardly any influence.

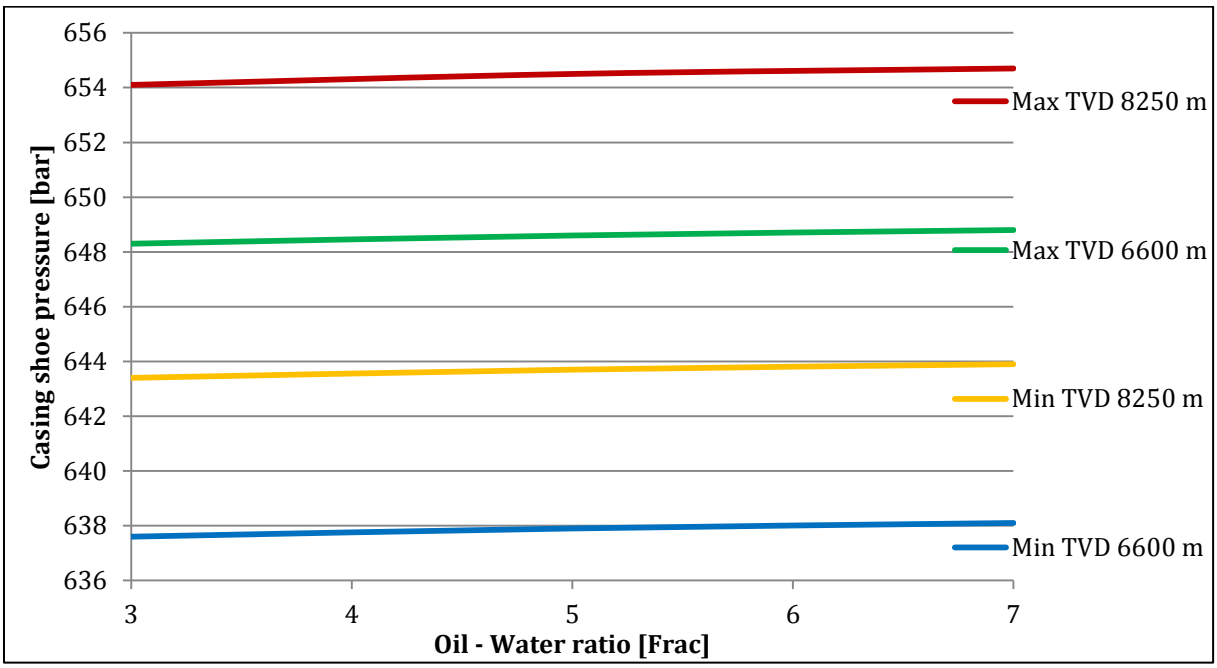

Figure 5.42: Casing shoe pressure as function of oil-water ratio

Figure 5.43 and Figure 5.44 displays the bottomhole pressure as function of oil – water ratio. At 8250 m the effects are similar as experienced on the casing shoe pressure above. Decreasing the ratio from 5 to 3 gives a 0,6 bar pressure decrease at maximum TVD. Increasing from 5 to 7 gives only a 0,2 bar pressure increase. At 6600 the effects have a more linear approximation, however the resulting pressure variation is no greater than ±0,3 bar.

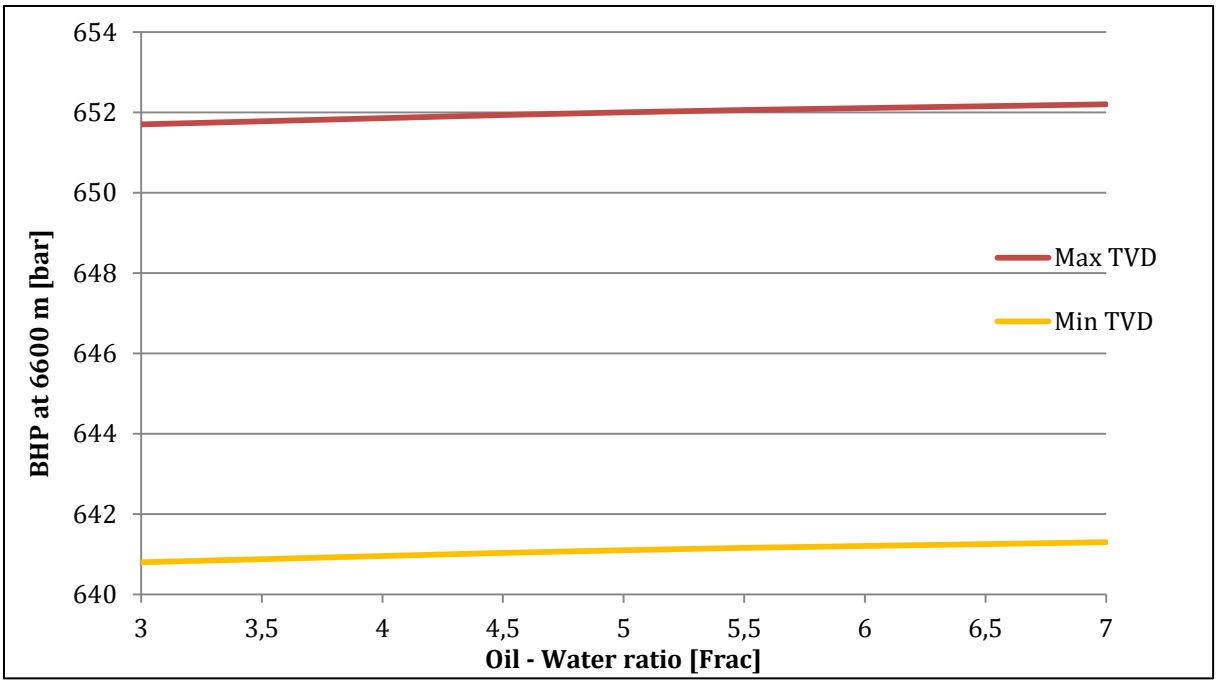

Figure 5.43: BHP as function of oil-water ratio at 6600m

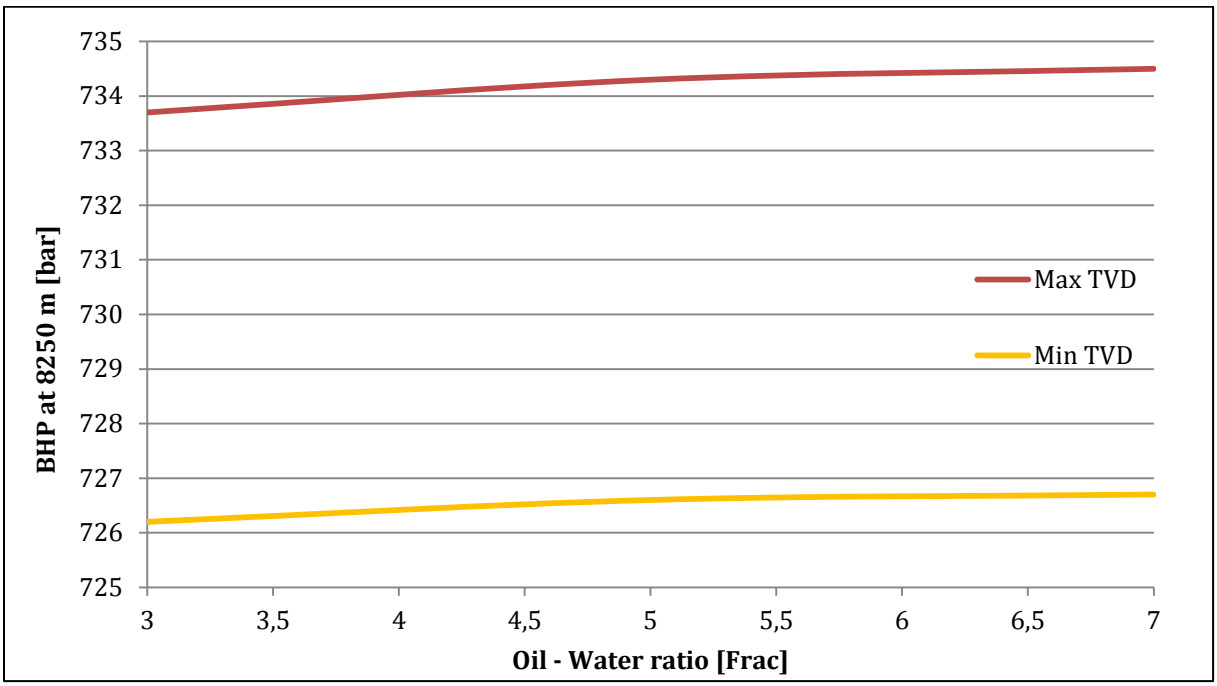

Figure 5.44: BHP as function of oil-water ratio at 8250m

6 Discussion of results

This chapter presents discussions based on the findings from the analyses. Each of the reviewed uncertainty variables, their effect and influencing factors will be discussed separately. Discussions regarding the credibility of the analysis including simulator biases and other effects that may produce misleading results will be presented.

6.1 Wellbore position uncertainty

Wellbore position uncertainty produces significant pressure variation in all three cases. An overview of the experienced variations on both bottomhole and casing shoe pressure is given in Table 6.1. Pressure variances are influenced by both well depth and position uncertainty, but mostly the latter.

Table 6.1: Pressure variations due to position uncertainty

	BHP [bar]	Shoe [bar]	Depth MD [m]
Case 1	±2,2	±2,2	3400
	±3	±2,2	4150
Case 2	±0,6	±0,5	4300
	±4,7	±0,5	6500
Case 3	±5	±5,1	6600
	±6,6	±5,1	7600
	±3,6	±5,2	8250

The variations are consistent and systematically increasing with depth uncertainty. The overall position uncertainty and the size of ellipsoids and projected ellipses are systematic and cumulative and will therefor increase with depth. However, this does not necessary imply that the depth (TVD) uncertainty will be equal for ellipsoids of the same size. The depth uncertainty is also influenced by the orientation of the ellipsoid. This is basically illustrated in Figure 6.1 explaining why the pressure difference at 4300 m in case 2 is ±0,6 bar whereas a ±3 bar difference is observed at a more shallow point (both TVD and MD) in case 1.

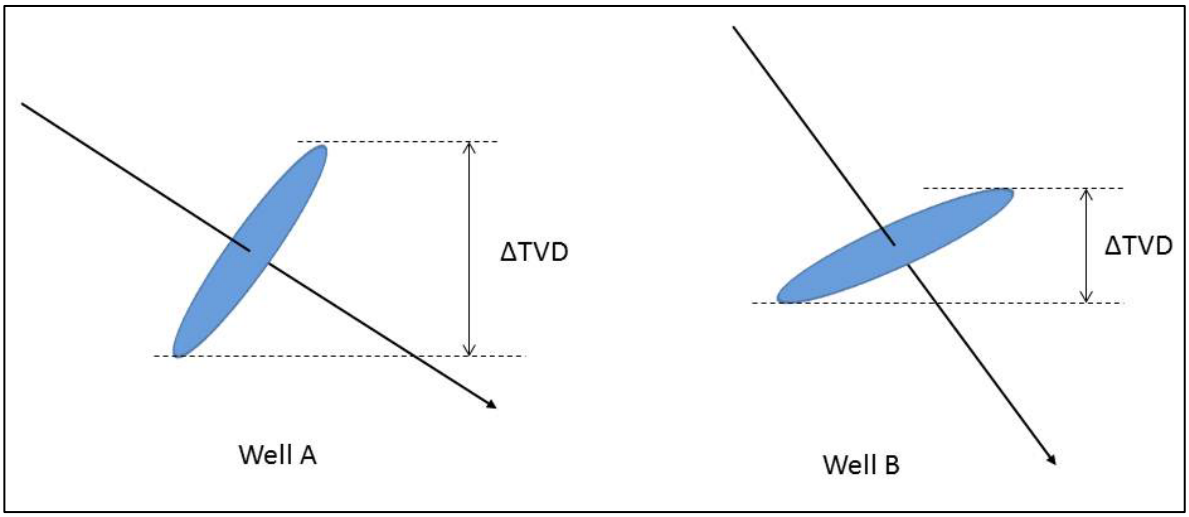

Figure 6.1: Depth uncertainty for equal ellipsoid sizes

Wellbore position uncertainty has another characteristic property, which effect is experienced in case 3. When the wellbore change orientation, there will be a delay before the ellipsoids do the same. This fact is acknowledged by the industry and may in some cases by used for the advantage of reducing the position uncertainty in a favorable direction before reaching a narrow target. The absolute magnitude of the position uncertainty is still cumulative and systematic, but will be differently oriented for a certain distance. This effect is displayed in Figure 6.2, where the depth uncertainty of well B decreases as the inclination drops. This explain why pressure variations decreases after 7600 m.

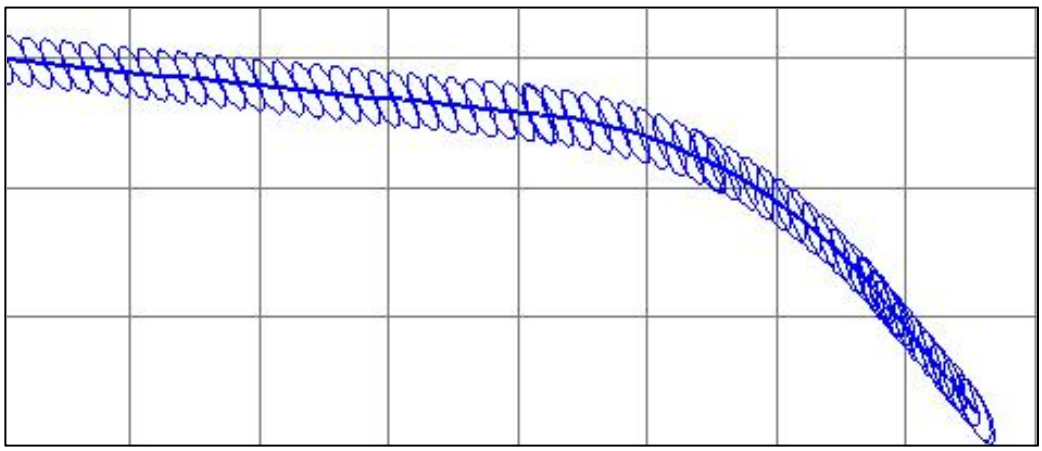

Figure 6.2: Change in ellipsoid orientation

6.2 Mud density uncertainty

Pressure variations due to mud density uncertainty are significant as expected. The effect of a 0,02 s.g. density increase for all cases at various depths is given in Table 6.2. All cases show similar and consistent results. The effect of density uncertainty increases with length and depth of the well, both within the same well and between different wells. This is reasonable to assume since the hydrostatic well pressure is directly linked to the mud density. Increasing mud weight also increases the casing shoe pressure. This increase is only affected by the setting depth of the shoe and not the length of the section. This is also reasonable to assume given that the hydrostatic pressure at a certain depth is only affected by the true vertical depth of the overlaying fluid column. However, it is important to notice that in these simulations, *only* the density of the mud was varied. When density changes occur in a downhole environment as a result of pressure, temperature, influxes and cuttings transport, other parameters such as rheology is likely to change as well. This will influence the downhole hydraulics and possibly give additional changes.

Table 6.2: Pressure variations resulting from 0,02 s.g. density increase

	BHP [bar]	Shoe [bar]	Depth MD [m]
Case 1	3,3	3,3	3400
	3,7	3,4	4150
Case 2	6,4	6,4	4300
	7,1	6,4	6500
Case 3	7,7	7,7	6600
	8,7	7,7	8250

6.3 Uncertainty in geothermal properties of formation rock

Pressure variations as a result of uncertainty in geothermal properties of formation rock are generally. Table 6.3 - Table 6.5 display the recorded pressure variations for case 1,2 and 3 respectively. The values displayed are the recorded maximum variations of a graph i.e. variation between the value recorded at SH = 900, TC = 1,4 and SH = 1500, TC = 3. Even with the large spectrum of input parameters, the largest variation recorded was 2,1 bars (± 1 bar).

The results are to some degree consistent, at least in well A and in the shallow parts of well B. The general trend is that an increase in either specific heat capacity or thermal conductivity will increase the pressure. However, at the more shallow depths, conductivity is clearly dominating.

There are some interesting observations made. The length of the openhole section does not seem to have a large influence on the recorded pressure variations. There are some reasons that may explain such result. The relationship between heat transfer in the formation and the wellbore pressure is the mud temperature. If more heat is transferred from the formation, the mud temperature will increase and this will affect rheological properties and most importantly, the density. In case 1, the formation temperature at TD is barely exceeding 60°C. With the recorded fluid temperature of 50°C already used in the simulation, the room for changes is small. In well B the temperature is significantly higher than in well A, pressure differences here are noticeable – but still small. The length of the openhole section in all cases is also considerably shorter than the casing length. Most of the heat transfer will accordingly take place inside the casing and not in the openhole section. The small variations experienced in well B would also be influenced by the high wellbore pressures. All pressure recordings were above 500 bars in case 2 (except one) and above 600 bars in case 3. Pressure has compressional effect on the mud and will thereby counteract some of the effects of thermal expansion. It is possible that other results could have been obtained from a more shallow well with high formation temperature.

Flow rate appear to have some effect on the recorded pressure variations. Higher pressure variations are generally experienced in case 2 (3300 l/min) than in the deeper and warmer

section of case 3 (2000 l/min). However the magnitude appear to be only in the range of ±0,1 bar and will therefore only be within the accuracy level of the simulator.

Table 6.3: Pressure variances - Case 1

Case 1		
	Var. BHP	**Var. Casing shoe pressure**
	[bar]	**[bar]**
3400 m		
Min TVD	0,8	0,7
Max TVD	0,9	0,7
4150 m		
Min TVD	0,9	0,8
Max TVD	0,9	0,8

Table 6.4: Pressure variances - Case 2

Case 2		
	Var. BHP	**Var. Casing shoe pressure**
	[bar]	**[bar]**
4300 m		
Min TVD	1,3	1,2
Max TVD	1,3	1,3
6500 m		
Min TVD	1,9	1,2
Max TVD	1,6	1,2

Table 6.5: Pressure variances - Case 3

Case 3		
	Var. BHP	**Var. Casing shoe pressure**
	[bar]	**[bar]**
6600 m		
Min TVD	1,1	1,1
Max TVD	1,2	1,1
8250 m		
Min TVD	1,5	0,7
Max TVD	2,1	1,3

Some fluctuations and non-physical variations occur. These may result from a bias or random noise in the simulator or from faulty input parameters. The presented results have too few data samples to conclude on this, it was therefore necessary to gather more information.

Figure 6.3 displays the additional data samples gathered at maximum TVD, 4300m in case 2. The red line represents the original graph with 4 measurements. The blue line shows the effects of adding additional measurements and the yellow line displays the data gathered from a second run of the same simulations. All data is tabulated and presented below the graph. There appear to be no random noise experienced in the simulator. The blue and yellow lines almost completely overlap, except for two points of measurement where the deviation is no more than 0,1 bar. These lines also coincide with the existing data. The new samples also show the same physical interpretation; any significant pressure increase results from a change in thermal conductivity. This is observed between measurements 3 and 4 - and 6 and 7. The experienced deviation from the original graph with fewer samples is only as expected when the measurements depend on two separate parameters and one is strictly dominating.

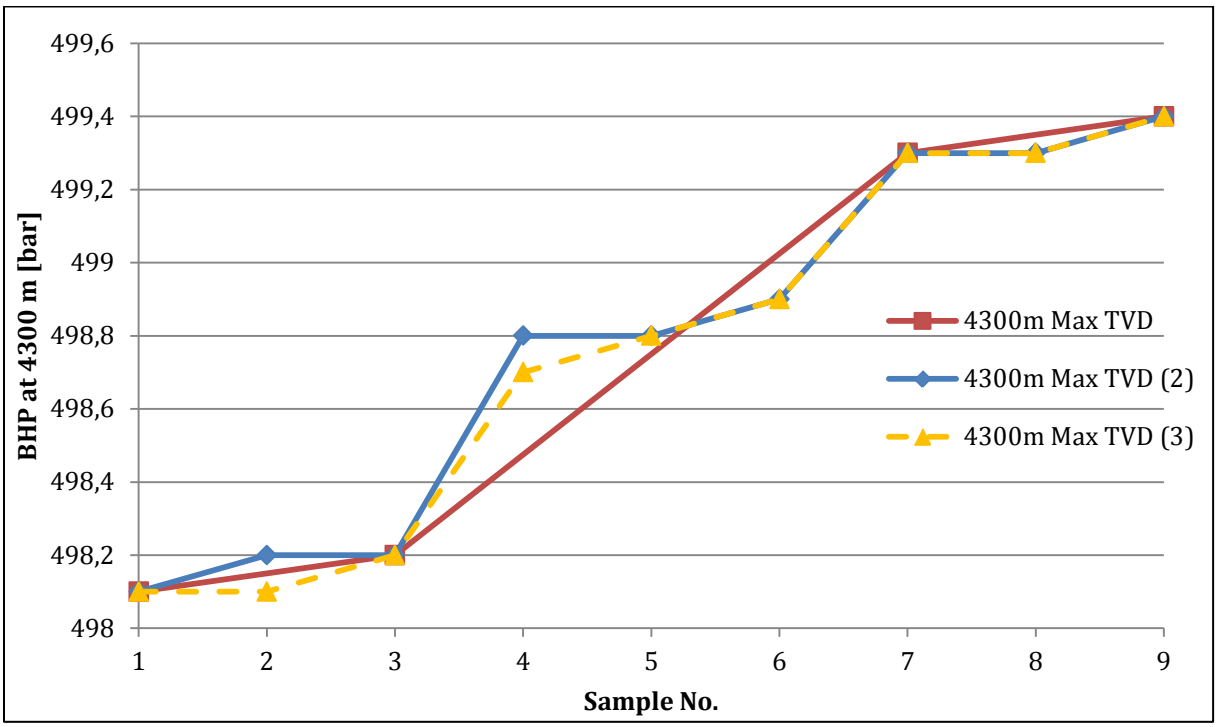

Figure 6.3: BHP at 4300 m, maximum TVD, case 2

Table 6.6: BHP and casing shoe pressure at 4300m, maximum TVD, case 2

BHP	Shoe	BHP(2)	Shoe(2)	BHP(3)	Shoe(3)	SH	TC	
[Bar]	[Bar]	[Bar]	[Bar]	[Bar]	[Bar]	[J/kg·K]	[W/m·K]	Sample No.
498,1	496,1	498,1	496,1	498,1	496,1	900	1,4	1
		498,2	496,2	498,1	496,2	1200	1,4	2
498,2	496,3	498,2	496,3	498,2	496,3	1500	1,4	3
		498,8	496,8	498,7	496,8	900	2,2	4
		498,8	496,9	498,8	496,9	1200	2,2	5
		498,9	496,9	498,9	496,9	1500	2,2	6
499,3	497,3	499,3	497,3	499,3	497,3	900	3	7
		499,3	497,4	499,3	497,4	1200	3	8
499,4	497,4	499,4	497,4	499,4	497,4	1500	3	9

The same consistency is observed in Figure 6.4, displaying the same case and trajectory at 6500m, the data is given in Table 6.7. The original graph here had a more linear approach and the additional samples only show slight deviations from this, no larger than 0,1 bar.

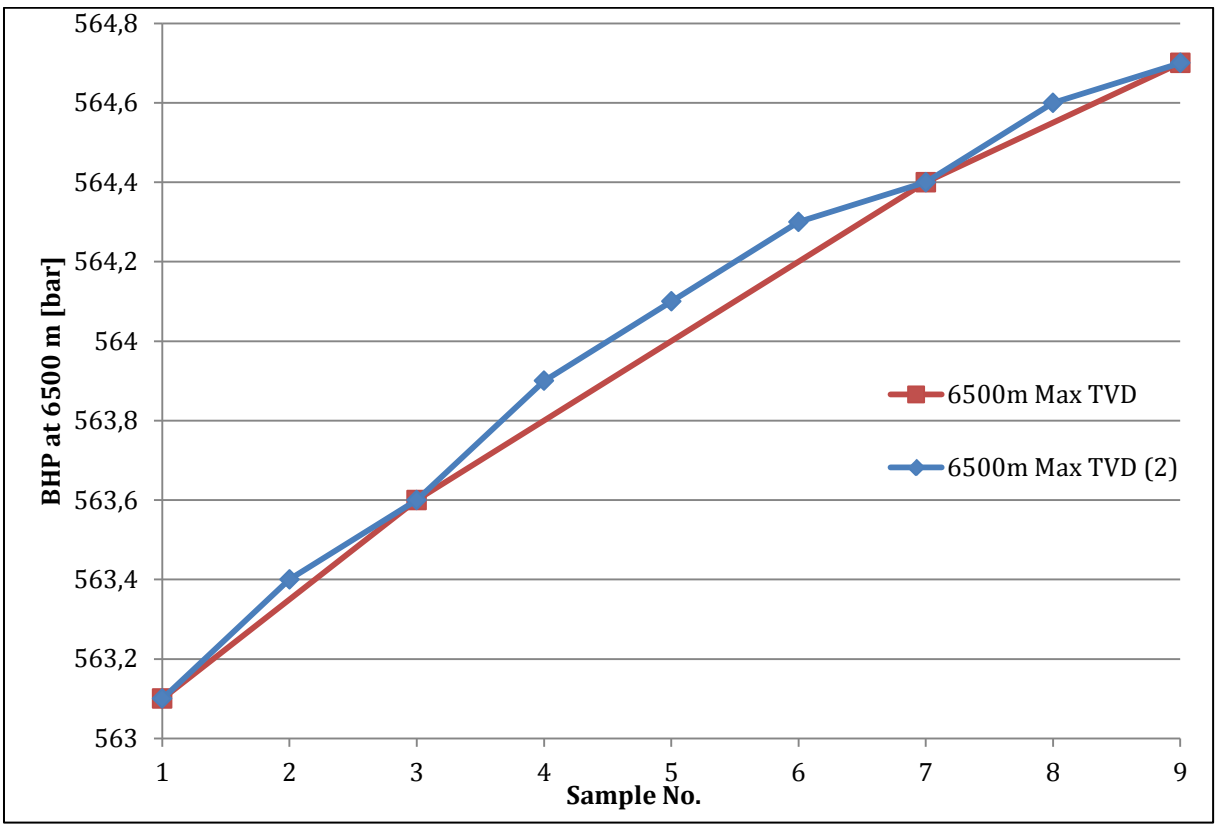

Figure 6.4: BHP at 6500 m, maximum TVD, case 2

Table 6.7: BHP and casing shoe pressure at 6500m, maximum TVD, case 2

BHP	Shoe	BHP(2)	Shoe(2)	SH	TC	
[Bar]	[Bar]	[Bar]	[Bar]	[J/kg·K]	[W/m·K]	Sample No.
563,1	498,7	563,1	498,7	900	1,4	1
		563,4	498,9	1200	1,4	2
498,2	496,3	563,6	499	1500	1,4	3
		563,9	499,3	900	2,2	4
		564,1	499,5	1200	2,2	5
		564,3	499,6	1500	2,2	6
499,3	497,3	564,4	499,7	900	3	7
		564,6	499,8	1200	3	8
564,7	499,9	564,7	499,9	1500	3	9

6.4 Uncertainty in oil – water ratio of mud

Analyses of the wellbore pressure effects exerted from uncertainty in the oil – water ratio of the drilling mud showed only small and inconsistent results. In case 1 and 2 there are no conclusive trends to be drawn from the results, neither within one case nor between the cases. In case 3 all data sets show that an increase in oil – water ratio gave a small increase on the wellbore pressure and vice versa. However, the variations were hardly visible when comparing to wellbore position uncertainty.

Additional data sampling to uncover biases or noise from the simulator was performed for two separate cases. Figure 6.5 presents bottomhole pressure as function of oil – water ratio for the maximum TVD trajectory at 4300 m – case 2. The same case as used above. The original data set is displayed as the linear red. The yellow and blue lines display the effect of adding additional samples in steps of 0,5 and 0,2 respectively. The recorded data is given in Table 6.8.

Neither in this case is any random noise experienced. All samples gathered at the same ratio are identical to one tenth of a bar. This coincides with previous observations. When more samples are added, the deviation from linearity increases, but the tendency suggests that in this case the pressure decreases as the oil – water ratio increases.

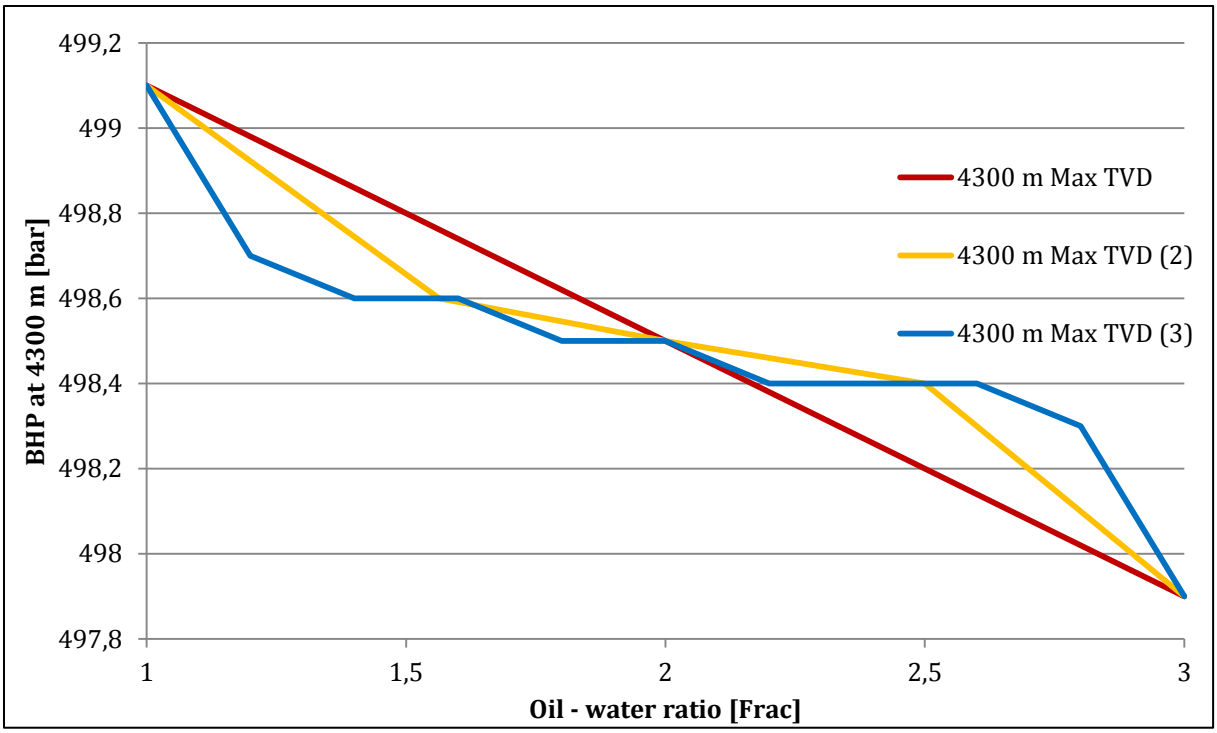

Figure 6.5: BHP at 4300 m, maximum TVD, case 2

Table 6.8: BHP and casing shoe pressure at 4300m, maximum TVD, case 2

	BHP	Shoe	BHP (2)	Shoe (2)	BHP (3)	Shoe (3)	SH	TC
OWR	[Bar]	[Bar]	[Bar]	[Bar]	[Bar]	[Bar]	[J/kg·K]	[W/m·K]
1	499,1	497,2	499,1	497,2	499,1	497,2	***1693***	***0,57***
1,2					498,7	496,8	1617	0,54
1,4					498,6	496,7	1554	0,52
1,564			498,6	496,7	498,6	496,7	*1526*	*0,51*
1,6					498,6	496,6	1501	0,5
1,8					498,5	496,5	1456	0,48
2	498,5	496,5	498,5	496,5	498,5	496,5	***1417***	***0,47***
2,2					498,4	496,5	1383	0,46
2,4					498,4	496,5	1353	0,44
2,5			498,4	496,4	498,4	496,4	*1340*	*0,44*
2,6					498,4	496,4	1327	0,43
2,8					498,3	496,4	1303	0,43
3	497,9	496	497,9	496	497,9	496	***1282***	***0,42***

Case 1 showed some peculiar results in which the bottomhole pressure decreased as the oil – water ratio decreased below 3. This was only experienced at minimum TVD. At maximum TVD a slight increase was experienced on the same interval. In Figure 6.6 the original and re-sampled data series of bottomhole pressure at 4150m, minimum TVD, are displayed as the yellow and red lines. Tabulated results are presented below. Large fluctuations with an amplitude of approximately 1,4 bar is experienced, but no indication of random noise. However as the amplitude value is larger than the actual experienced pressure variations, any results in this case would have to be discarded.

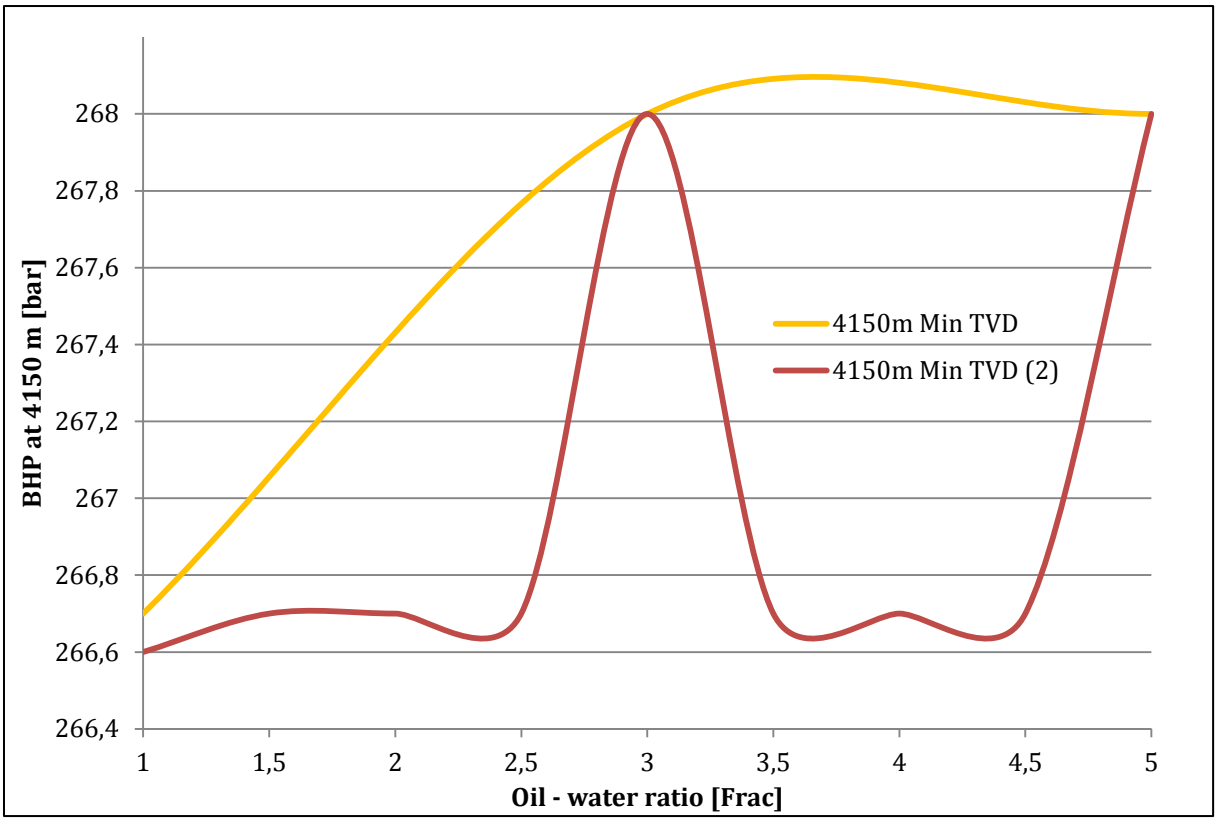

Figure 6.6: BHP at 4150 m, minimum TVD, case 1

Table 6.9: BHP and casing shoe pressure at 4150m, minimum TVD, case 1

	BHP	Shoe	BHP (2)	Shoe (2)	SH	TC
OWR	[Bar]	[Bar]	[Bar]	[Bar]	[J/kg·K]	[W/m·K]
1	266,7	238,3	266,6	238,3	***2053***	***0,49***
1,5			266,7	238,3	1846	0,44
2			266,7	238,3	1710	0,4
2,5			266,7	238,3	1613	0,37
3	268	239,6	268	239,6	***1541***	***0,35***
3,5			266,7	238,4	1485	0,34
4			266,7	238,4	1440	0,32
4,5			266,7	238,4	1404	0,31
5	268	239,6	268	239,6	***1374***	***0,31***

7 Conclusions

This thesis has provided a new view to the effects of wellbore position uncertainty. It has been shown quantitatively how these effects together with uncertainty in other drilling parameters will influence wellbore pressures. The extent of the influence is related to the uncertainties in the individual parameters themselves along with the length and depth of the well.

Wellbore position uncertainty has been shown to have significant impact on the wellbore pressure, at least in longer wells. Magnitude of the experienced variations is systematic and a direct result of depth (TVD) uncertainty of the wellbore. Significance of pressure variations in shorter wells have not been discussed, however in longer and more complex wells with narrow pressure margins, these uncertainties will have to be considered.

Uncertainties in mud density can generate significant pressure variations both at the bottomhole depth and at another critical depth, a distance far away from the downhole measurements. The magnitude of the pressure uncertainty is systematic and cumulative, depending on the depth uncertainty of the wellbore at the point of measurement and the density uncertainty itself. Many uncertainty parameters have been discussed, giving reasonable credibility to assumptions of significant density uncertainty. However it was not the topic of this thesis to determine this uncertainty explicitly.

Uncertainties in formation geothermal properties gave relatively consistent results where an increase in either the specific heat capacity or thermal conductivity will increase the wellbore pressure and vice versa. However at more shallow depth the uncertainty in thermal conductivity is strongly dominating. The resulting pressure variations are effected by both well depth and length of the openhole section, however the latter appear only to apply for long sections where high temperatures are experienced. Some indications of influence by flow rate, pressure and temperature have also been observed, however the amount of data in these analyses is not sufficient to conclude on this. The magnitude of the experienced pressure variations are relatively small compared to the large spectrum used in input parameters. Due to the time-consuming work of gathering these data, only a limited number of samples are gathered in each case. Some uncertainty in the results will therefore have to be considered.

Analysis of uncertainty in oil – water ratio of mud gave only inconclusive results. Large fluctuations and unphysical variations were experienced. No particular trend was seen in the analyses, neither between different cases nor within the same case. The source of these fluctuations was not uncovered, however it is most likely due to a numerical calculation bias within the drilling calculator used to perform the simulations.

8 Future work

The work presented in this thesis is a different approach to the effect on wellbore position uncertainty. It has been shown that such effects along with uncertainty in other drilling parameter including mud density and formation geothermal properties can – and will affect wellbore pressures. The pressure variations resulting from wellbore position uncertainty, mud density uncertainty and to some extent also formation geothermal properties have a systematic nature, similar to the position uncertainty itself. Future work on this topic would include analysis of more cases, for different well geometries and formation properties including the effects of transient cuttings transportation. More simulations could also be run in all cases for different configurations of mud type, flow rate and surface rotation to isolate the individual effect. Eventually, the cumulative pressure uncertainty could be established for each survey station of a wellbore. This would include deriving a method for calculating a standard deviation including all the uncertainty parameters. Calculation of the standard deviation would have to be based on the actual values recorded while drilling and could also be included in drilling software operating with real-time data. Knowing the actual pressure uncertainties of a wellbore could be a great advantage when drilling highly complex well, such as presented in this thesis.

Analytical approaches to the calculation of a standard deviation could be attempted. However these are highly complex calculations and may not be possible to perform analytically. A different approach is to do calculation numerically. In this case a Monte Carlo simulation is suggested. In this simulation random values randomly sampled from probability distributions to generate numerical results. Repeating simulations multiple times will eventually generate sufficient amounts of data to create a new probability distribution, representing the expected pressure value along with the variance or standard deviation.

9 Appendix

9.1 Derivation of inverse covariance matrix

The inverse covariance matrix will be derived according to Cramer's rule given in Equation 9.1.

$$A^{-1} = \frac{adj\ A}{|A|} \qquad \textbf{Equation 9.1}$$

In which adj A is the adjoint matrix of A and |A| is the determinant of A. The adjoint matrix of A can be found as the transpose of the cofactor matrix [A_{ij}].

The symmetric covariance matrix is given as in Equation 2.9 with the elements now denoted as h_{ij} for calculation purposes.

$$COV = \begin{bmatrix} h_{11} & h_{12} & h_{13} \\ h_{12} & h_{22} & h_{23} \\ h_{13} & h_{23} & h_{33} \end{bmatrix} \qquad \textbf{Equation 9.2}$$

The elements of the cofactor matrix computed from the covariance matrix are denoted as A_{ij} and given as follows:

$$A_{11} = \begin{vmatrix} h_{22} & h_{23} \\ h_{23} & h_{33} \end{vmatrix} \qquad \textbf{Equation 9.3}$$

$$A_{12} = -\begin{vmatrix} h_{12} & h_{23} \\ h_{13} & h_{33} \end{vmatrix} \qquad \textbf{Equation 9.4}$$

The other elements of A_{ij} are given similarly.

The determinant of the covariance matrix is given as:

$$|COV| = h_{11}h_{22}h_{33} - h_{11}h_{23}^2 - h_{12}^2h_{33} + 2h_{12}h_{13}h_{23} - h_{13}^2h_{22} \qquad \textbf{Equation 9.5}$$

Accordingly the inverse covariance matrix is given in Equation 9.6.

$$COV^{-1} = \frac{\begin{bmatrix} h_{22}h_{33} - h_{23}^2 & h_{13}h_{23} - h_{12}h_{33} & h_{12}h_{23} - h_{13}h_{22} \\ h_{13}h_{23} - h_{12}h_{33} & h_{11}h_{33} - h_{13}^2 & h_{12}h_{13} - h_{11}h_{23} \\ h_{12}h_{23} - h_{13}h_{22} & h_{12}h_{13} - h_{11}h_{23} & h_{11}h_{22} - h_{12}^2 \end{bmatrix}}{h_{11}h_{22}h_{33} - h_{11}h_{23}^2 - h_{12}^2h_{33} + 2h_{12}h_{13}h_{23} - h_{13}^2h_{22}} \quad \textbf{Equation 9.6}$$

Note that also the inverse covariance matrix is a symmetric matrix.

9.2 Wellbore position uncertainty

A summary of the calculation tables for well A and well B is presented in the following. The columns 1-3 are the measured data. The ½ long and ½ short values represent the semi-long and semi-short axis of the ellipses resulting from projection of the ellipsoid onto the horizontal, vertical and perpendicular plane. The horizontal, vertical and perpendicular angles give the orientations of the projected ellipses in the respective planes. The horizontal angle is given between north the semi-long axis of the horizontal ellipse. The vertical angle is given between vertical and the semi-long axis of the vertical ellipsoid. The perpendicular angle is given between the cross-axial borehole axis and the semi-long axis of the perpendicular ellipsoid. These angles are modular to 180°.

9.2.1 Well A

Table 9.1: Summary of calculation table for well position uncertainty - Well A

MD	Incl.	Az.	TVD	North	East	1/2 Long Hor	1/2 short Hor	Ang Hor	1/2 Long Ver	1/2 Short Ver	Ang Ver	1/2 Long Per	1/2 Short Per	Ang per
[m]	[°]	[°]	[m]	[m]	[m]	[m]	[m]	[°]	[m]	[m]	[°]	[m]	[m]	[°]
0	0	0	0	0,0	0	0	0	0	0	0	0	0	0	0
30	0	0	30	0,0	0	0,052	0,052	45	0,06	0,052	0	0,1	0,052	225
60	0	0	60	0,0	0	0,105	0,105	45	0,121	0,105	0	0,1	0,105	225
90	0	0	90	0,0	0	0,157	0,157	45	0,181	0,157	0	0,2	0,157	225
120	0	0	120	0,0	0	0,209	0,209	45	0,241	0,209	0	0,2	0,209	225
630	22,88	146	620,7	-59,5	40,14	2,375	1,124	144,01	2,714	1,267	90,93	2,4	1,118	88,7
660	24,87	146	648,1	-69,6	46,92	2,705	1,182	144,04	3,105	1,33	90,91	2,7	1,171	88,8
690	26,86	146	675,1	-80,4	54,24	3,061	1,242	144,08	3,528	1,396	90,89	3,1	1,224	89
720	28,85	146,2	701,7	-92,1	62,06	3,444	1,302	144,13	3,979	1,463	90,89	3,4	1,275	89
750	30,66	151	727,7	-104,8	69,81	3,847	1,368	144,68	4,406	1,533	91,03	3,8	1,327	85,4
780	32,63	155,3	753,2	-118,8	76,9	4,271	1,441	145,56	4,832	1,607	91,19	4,2	1,38	82,7
1530	65	169,6	1163	-725,3	120	19,81	4,357	169,73	13,26	5,456	97,38	20	3,927	91,2
1560	65	169,6	1176	-752,1	125	20,53	4,459	169,7	13,74	5,662	97,35	21	4,075	91,2
1590	65	169,9	1188	-778,8	129,8	21,24	4,561	169,69	14,19	5,867	97,37	21	4,224	91
1620	67,26	169,9	1200	-805,8	134,6	21,97	4,658	169,68	14,67	6,081	97,33	22	4,574	91,1
1650	70,25	169,8	1211	-833,3	139,6	22,71	4,746	169,67	15,17	6,306	97,27	23	5,009	91,2
3210	75,27	169,6	1610	-2316,5	412,5	62,39	8,677	169,42	41,36	19,02	95,49	62	17,02	91,3
3240	75,27	169,6	1618	-2345,0	417,7	63,16	8,755	169,42	41,86	19,27	95,48	63	17,24	91,3
3270	75,27	169,6	1625	-2373,6	423	63,92	8,833	169,42	42,37	19,51	95,46	64	17,47	91,3
3300	75,27	169,6	1633	-2402,1	428,2	64,68	8,911	169,42	42,87	19,76	95,45	65	17,7	91,3
3330	75,27	169,6	1641	-2430,6	433,5	65,45	8,989	169,42	43,38	20,01	95,43	65	17,93	91,3
3360	75,27	169,6	1648	-2459,2	438,7	66,21	9,067	169,41	43,89	20,26	95,42	66	18,15	91,3
3390	75,27	169,6	1656	-2487,7	444	66,97	9,145	169,41	44,39	20,5	95,4	67	18,38	91,3
4020	74,57	189,5	1817	-3088,2	530	82,89	10,88	169,93	53,4	25,5	96,62	78	22,79	84,9
4050	74,64	193,7	1825	-3116,6	524,2	83,58	10,99	170,14	55,02	25,76	96,36	77	22,92	83,4
4080	74,8	197,8	1833	-3144,4	516,3	84,24	11,1	170,39	57,08	26,03	95,96	76	23,04	82
4110	75,02	202	1841	-3171,6	506,5	84,88	11,21	170,66	59,51	26,32	95,49	74	23,14	80,4
4140	75,33	206,1	1849	-3198,1	494,7	85,49	11,32	170,97	62,25	26,62	94,98	71	23,22	78,8
4170	75,41	207,1	1856	-3224,1	481,7	86,1	11,43	171,27	62,79	26,87	94,94	71	23,41	78,5
5790	85,24	207,1	2140	-4635,9	-239	122,2	15,48	3,14	45,67	36,07	134,3	112	39,73	86,2
5820	85,24	207,1	2142	-4662,5	-252,6	123	15,52	3,3	45,5	35,79	137,2	113	39,99	86,2
5850	85,24	207,1	2145	-4689,1	-266,2	123,7	15,57	3,45	45,36	35,43	140,1	114	40,25	86,2
5880	85,24	207,1	2147	-4715,7	-279,8	124,4	15,61	3,6	45,27	35,02	142,9	114	40,51	86,2
5910	85,24	207,1	2150	-4742,3	-293,5	125,1	15,66	3,75	45,22	34,54	145,5	115	40,77	86,3
5934,4	85,24	207,1	2152	-4763,9	-304,5	125,7	15,69	3,87	45,2	34,11	147,6	116	40,98	86,3

9.2.2 Well B

Table 9.2: Summary of calculation table for well position uncertainty – Well B

MD	Inc.	Az.	TVD	North	East	1/2 Long Hor.	1/2 short Hor.	Ang. Hor.	1/2 Long Ver.	1/2 Short Ver.	Ang. Ver.	1/2 Long Per.	1/2 Short Per.	Ang. Per.
[m]	[°]	[°]	[m]	[m]	[m]	[m]	[m]	[°]	[m]	[m]	[°]	[m]	[m]	[°]
259,9	0,51	208,0	259,9	-0,8	-0,9	0,5	0,5	137,1	0,5	0,5	179,8	0,5	0,5	109,2
269,9	0,55	200,6	269,9	-0,9	-0,9	0,5	0,5	135,5	0,5	0,5	179,8	0,5	0,5	115,0
279,9	0,52	197,6	279,9	-1,0	-0,9	0,5	0,5	44,1	0,6	0,5	179,8	0,5	0,5	116,5
292,4	1,14	123,8	292,4	-1,1	-0,9	0,5	0,5	35,0	0,6	0,5	0,0	0,5	0,5	180,8
309,0	2,74	115,6	309,0	-1,4	-0,4	0,5	0,5	1,9	0,6	0,5	180,0	0,5	0,5	158,7
1121,6	26,1	218,5	1066,6	-186,8	-170,3	7,3	2,0	43,0	2,4	2,0	157,7	7,2	1,9	93,2
1150,0	26,1	219,1	1092,2	-196,6	-178,1	7,6	2,0	42,9	2,5	2,0	158,5	7,6	2,0	92,5
1178,3	25,5	219,7	1117,6	-206,1	-185,9	7,9	2,1	42,8	2,6	2,0	159,1	7,9	2,0	91,9
1190,8	25,0	220,5	1128,9	-210,2	-189,4	8,1	2,1	42,8	2,6	2,0	160,1	8,1	2,0	91,2
1199,0	25,4	220,3	1136,3	-212,8	-191,6	8,2	2,1	42,7	2,6	2,1	159,7	8,2	2,1	91,4
3043,9	49,0	170,5	2411,3	-1486,3	-194,8	39,9	10,4	8,1	17,1	8,4	117,8	38,9	5,1	101,2
3071,3	48,7	171,1	2429,4	-1506,6	-191,5	40,4	10,6	7,8	17,0	8,4	119,1	39,5	5,1	100,8
3097,6	48,7	171,4	2446,7	-1526,2	-188,4	40,9	10,7	7,6	17,1	8,4	120,0	40,0	5,2	100,4
3126,2	48,6	171,2	2465,6	-1547,4	-185,2	41,4	10,8	7,4	17,3	8,4	120,1	40,6	5,2	100,4
3153,6	48,7	171,7	2483,7	-1567,7	-182,1	42,0	11,0	7,2	17,3	8,4	121,1	41,1	5,3	99,9
4196,9	51,7	176,0	3151,0	-2368,1	-137,5	62,8	15,9	3,6	23,0	8,9	133,4	62,5	7,7	94,6
4220,7	51,8	175,4	3165,7	-2386,7	-136,1	63,3	16,0	3,5	23,3	9,2	132,9	62,9	7,7	94,9
4251,5	51,9	174,8	3184,7	-2410,8	-134,0	63,9	16,2	3,4	23,6	9,6	132,3	63,5	7,8	95,2
4276,7	51,9	174,6	3200,3	-2430,6	-132,2	64,4	16,3	3,3	23,8	9,7	132,2	64,0	7,8	95,3
4277,0	51,9	174,6	3200,5	-2430,9	-132,2	64,4	16,3	3,3	23,8	9,7	132,2	64,0	7,8	95,3
5220,0	84,1	174,3	3440,4	-3318,0	-38,7	87,6	18,7	0,6	30,5	11,4	141,6	87,1	23,2	91,0
5250,0	84,1	174,3	3443,5	-3347,7	-35,7	88,4	18,7	0,5	30,7	11,5	141,9	87,9	23,4	91,0
5280,0	84,1	174,3	3446,5	-3377,4	-32,7	89,2	18,8	0,5	30,9	11,5	142,2	88,7	23,7	91,0
5310,0	84,1	174,3	3449,6	-3407,0	-29,7	90,0	18,8	0,4	31,1	11,6	142,5	89,5	23,9	91,0
5340,0	84,1	174,3	3452,7	-3436,7	-26,7	90,7	18,8	0,4	31,3	11,6	142,8	90,3	24,2	91,0
6390,0	84,1	174,3	3559,9	-4476,0	77,9	118,0	20,5	178,9	39,4	13,3	150,6	117,7	33,0	91,0
6420,0	84,1	174,3	3562,9	-4505,7	80,9	118,8	20,6	178,8	39,6	13,4	150,8	118,4	33,3	91,0
6450,0	84,1	174,3	3566,0	-4535,4	83,9	119,6	20,6	178,8	39,9	13,4	151,0	119,2	33,6	91,0
6480,0	84,1	174,3	3569,0	-4565,1	86,9	120,4	20,7	178,8	40,1	13,5	151,2	120,0	33,8	90,9
6500,0	84,1	174,3	3571,1	-4584,9	88,9	120,9	20,7	178,7	40,3	13,5	151,3	120,5	34,0	90,9
8400,0	40,0	174,3	4094,2	-6324,9	264,1	166,5	25,6	177,4	54,9	16,4	155,5	166,5	20,1	92,7
8430,0	40,0	174,3	4117,1	-6344,1	266,1	167,1	25,8	177,4	55,0	16,4	155,4	167,0	20,1	92,7
8460,0	40,0	174,3	4140,1	-6363,3	268,0	167,6	25,9	177,4	55,2	16,5	155,4	167,5	20,1	92,7
8467,4	40,0	174,3	4145,8	-6368,0	268,5	167,7	25,9	177,4	55,2	16,5	155,3	167,6	20,1	92,7

9.3 Tabulated data – Case 1

9.3.1 Effect of wellbore position uncertainty

Table 9.3: Analysis of pressure effects by wellbore position uncertainty

		No uncertainty		Maximum TVD		Minimum TVD	
Bit depth	**Bit depth**	**BHP**	**Shoe**	**BHP**	**Shoe**	**BHP**	**Shoe**
TVD [m]	**MD [m]**	**[bar]**	**[bar]**	**[bar]**	**[bar]**	**[bar]**	**[bar]**
1658,43	3400	242,9	242,1	245,1	244,3	240,7	239,9
1683,86	3500	246,7	242,1	249	244,3	244,4	239,9
1709,28	3600	250,5	242,2	252,9	244,3	248,1	240
1734,71	3700	254,3	242,2	256,7	244,3	251,8	239,9
1760,14	3800	258	242,1	260,4	244,1	255,5	239,9
1785,63	3900	261,8	242,1	264,5	244,3	259,1	239,9
1811,97	4000	265,7	242,1	268,4	244,3	262,9	239,9
1834,40	4100	269,6	242,1	272,4	244,2	266,7	239,9
1851,20	4150	271,5	242	274,4	244,2	268,6	239,8

9.3.2 Effect of mud density uncertainty

Table 9.4: Mud density – and wellbore position uncertainty at 3400 m

Bit Depth	*3400*					
	No Uncertainty		Maximum TVD		Minimum TVD	
Mud density	**BPH**	**Shoe**	**BPH**	**Shoe**	**BPH**	**Shoe**
[s.g.]	**[bar]**	**[bar]**	**[bar]**	**[bar]**	**[bar]**	**[bar]**
1,3	239,1	238,3	241,3	240,5	236,9	236,1
1,323	242,9	242,1	245,1	244,3	240,7	239,9
1,34	245,7	244,9	247,9	247,1	243,5	242,7
1,36	249	248,2	251,3	250,4	246,6	245,8
1,38	252,3	251,5	254,6	253,7	250	249,1
1,4	255,6	254,7	257,9	257,1	253,2	252,4

Table 9.5: Mud density – and wellbore position uncertainty at 3700 m

Bit Depth	*3700*					
	No Uncertainty		Maximum TVD		Minimum TVD	
Mud density	**BPH**	**Shoe**	**BPH**	**Shoe**	**BPH**	**Shoe**
[s.g.]	**[bar]**	**[bar]**	**[bar]**	**[bar]**	**[bar]**	**[bar]**
1,3	250,3	238,4	252,8	240,5	247,9	236,2
1,323	254,3	242,2	256,7	244,3	251,8	239,9
1,34	257,2	244,9	259,7	247,2	254,7	242,7
1,36	260,7	248,2	263,2	250,5	258,1	246
1,38	264,1	251,5	266,7	253,8	261,5	249,2
1,4	267,6	254,8	270,2	257,1	264,9	252,5

Table 9.6: Mud density – and wellbore position uncertainty at 4150 m

Bit Depth	*4150*					
	No Uncertainty		Maximum TVD		Minimum TVD	
Mud density	**BPH**	**Shoe**	**BPH**	**Shoe**	**BPH**	**Shoe**
[s.g.]	**[bar]**	**[bar]**	**[bar]**	**[bar]**	**[bar]**	**[bar]**
1,3	267,2	238,3	270,1	240,4	264,4	236,1
1,323	271,5	242	274,4	244,2	268,6	239,8
1,34	274,6	244,8	277,5	247,1	271,6	242,6
1,36	278,3	248,1	281,3	250,4	275,3	245,8
1,38	282	251,4	284,9	253,6	278,9	249,1
1,4	285,6	254,7	288,7	257	282,6	252,4

9.3.3 Effect of uncertainty in geothermal properties

Table 9.7: Effect of uncertainties in geothermal properties with SH = 900 J/kg·K, TC = 1,4 W/m·K

Specific heat capacity		*900*	*J/kg·K*	
Thermal conductivity		*1,4*	*W/m·K*	
	Min TVD		Max TVD	
Bit depth	**BHP**	**Shoe**	**BHP**	**Shoe**
MD [m]	**[Bar]**	**[Bar]**	**[Bar]**	**[Bar]**
3400	238,6	237,9	243	242,3
4150	266,3	238	272,1	242,4

Table 9.8: Effect of uncertainties in geothermal properties with SH = 1500 J/kg·K, TC = 1,4 W/m·K

Specific heat capacity		*1500*	*J/kg·K*	
Thermal conductivity		*1,4*	*W/m·K*	
	Min TVD		Max TVD	
Bit depth	**BHP**	**Shoe**	**BHP**	**Shoe**
MD [m]	**[Bar]**	**[Bar]**	**[Bar]**	**[Bar]**
3400	238,7	238	243,1	242,4
4150	266,4	238,1	272,3	242,5

Table 9.9: Effect of uncertainties in geothermal properties with SH = 900 J/kg·K, TC = 3 W/m·K

Specific heat capacity		*900*	*J/kg·K*	
Thermal conductivity		*3*	*W/m·K*	
	Min TVD		Max TVD	
Bit depth	**BHP**	**Shoe**	**BHP**	**Shoe**
MD [m]	**[Bar]**	**[Bar]**	**[Bar]**	**[Bar]**
3400	239,3	238,5	243,8	243
4150	267,1	238,7	272,9	243,1

Table 9.10: Effect of uncertainties in geothermal properties with SH = 1500 J/kg·K, TC = 3 W/m·K

Specific heat capacity		*1500*	*J/kg·K*	
Thermal conductivity		*3*	*W/m·K*	
	Min TVD		Max TVD	
Bit depth	**BHP**	**Shoe**	**BHP**	**Shoe**
MD [m]	**[Bar]**	**[Bar]**	**[Bar]**	**[Bar]**
3400	239,4	238,6	243,9	243
4150	267,2	238,8	273	243,2

9.3.4 Effect of uncertainty in oil-water ratio of mud

Table 9.11: Effect of uncertainties in oil – water ratio of mud with OWR = 1

Oil-Water ratio		*1*		
Specific heat capacity		*2053*	*J/kg·K*	
Thermal conductivity		*0,49*	*W/m·K*	
	Min TVD		Max TVD	
Bit depth	**BHP**	**Shoe**	**BHP**	**Shoe**
MD [m]	**[Bar]**	**[Bar]**	**[Bar]**	**[Bar]**
3400	239	238,2	243,6	242,7
4150	266,7	238,3	272,6	242,8

Table 9.12: Effect of uncertainties in oil – water ratio of mud with OWR = 3

Oil-Water ratio		*3*		
Specific heat capacity		*1541*	*J/kg·K*	
Thermal conductivity		*0,35*	*W/m·K*	
	Min TVD		Max TVD	
Bit depth	**BHP**	**Shoe**	**BHP**	**Shoe**
MD [m]	**[Bar]**	**[Bar]**	**[Bar]**	**[Bar]**
3400	240,2	239,4	243,4	242,6
4150	268	239,6	272,5	242,7

Table 9.13: Effect of uncertainties in oil – water ratio of mud with OWR = 5

Oil-Water ratio		*5*		
Specific heat capacity		*1374*	*J/kg·K*	
Thermal conductivity		*0,31*	*W/m·K*	
	Min TVD		Max TVD	
Bit depth	**BHP**	**Shoe**	**BHP**	**Shoe**
MD [m]	**[Bar]**	**[Bar]**	**[Bar]**	**[Bar]**
3400	240,2	239,4	243,4	242,5
4150	268	239,6	272,4	242,7

9.4 Tabulated data – Case 2

9.4.1 Effect of wellbore position uncertainty

Table 9.14: Pressure effects by wellbore position uncertainty

		No uncertainty		Maximum TVD		Minimum TVD	
Bit depth TVD [m]	**Bit depth MD [m]**	**BHP [bar]**	**Shoe [bar]**	**BHP [bar]**	**Shoe [bar]**	**BHP [bar]**	**Shoe [bar]**
3214,56	4300	500	498,1	500,6	498,6	499,4	497,5
3323,33	4500	517	498,1	518,1	498,6	515,7	497,5
3385,63	4700	527,1	498,3	529,4	498,9	524,6	497,8
3407,73	4900	531,4	498,8	534	499,3	528,5	498,3
3428,15	5100	535,4	499,2	538,5	499,7	532,2	498,7
3448,56	5300	539,3	499,6	542,7	500,1	535,9	499,1
3468,99	5500	543,3	500	546,9	500,5	539,6	499,5
3489,41	5700	547,3	500,4	551,1	500,9	543,3	499,9
3509,82	5900	551,2	500,7	555,3	501,2	547	500,2
3530,24	6100	555,1	501,1	559,4	501,6	550,7	500,6
3550,66	6300	559	501,4	563,6	501,9	554,3	500,9
3571,08	6500	562,9	501,7	567,8	502,2	558	501,2

9.4.2 Effect of mud density uncertainty

Table 9.15: Mud density – and wellbore position uncertainty at 4300 m

Bit Depth	*4300*					
	No Uncertainty		Maximum TVD		Minimum TVD	
Mud density	**BPH**	**Shoe**	**BPH**	**Shoe**	**BPH**	**Shoe**
[s.g.]	**[bar]**	**[bar]**	**[bar]**	**[bar]**	**[bar]**	**[bar]**
1,5	480,8	478,9	481,4	479,5	480,2	478,4
1,52	487,2	485,3	487,8	485,9	486,6	484,7
1,54	493,6	491,7	494,2	492,3	493	491,1
1,56	500	498,1	500,6	498,6	499,4	497,5
1,58	506,4	504,5	507	505	505,8	503,8
1,6	512,8	510,8	513,4	511,4	512,2	510,2

Table 9.16: Mud density – and wellbore position uncertainty at 5000 m

Bit Depth	*5000*					
	No Uncertainty		Maximum TVD		Minimum TVD	
Mud density	**BPH**	**Shoe**	**BPH**	**Shoe**	**BPH**	**Shoe**
[s.g.]	**[bar]**	**[bar]**	**[bar]**	**[bar]**	**[bar]**	**[bar]**
1,5	512,9	479,9	515,8	480,3	510	479,3
1,52	519,7	486,2	522,6	486,7	516,8	485,7
1,54	526,5	492,6	529,5	493,1	523,5	492,1
1,56	533,4	499	536,3	499,5	530,3	498,5
1,58	540,2	505,4	543,2	505,9	537,1	504,8
1,6	547	511,8	550,1	512,3	543,9	511,2

Table 9.17: Mud density – and wellbore position uncertainty at 5700 m

Bit Depth	*5700*					
	No Uncertainty		Maximum TVD		Minimum TVD	
Mud density	**BPH**	**Shoe**	**BPH**	**Shoe**	**BPH**	**Shoe**
[s.g.]	**[bar]**	**[bar]**	**[bar]**	**[bar]**	**[bar]**	**[bar]**
1,5	526,3	481,2	530	481,7	522,6	480,7
1,52	533,3	487,6	537	488,1	529,5	487,1
1,54	540,3	494	544	494,5	536,4	493,5
1,56	547,3	500,4	551,1	500,9	543,3	499,9
1,58	554,2	506,8	558,1	507,3	550,3	506,2
1,6	561,2	513,2	565,1	513,7	557,2	512,6

Table 9.18: Mud density – and wellbore position uncertainty at 6500 m

Bit Depth	*6500*					
	No Uncertainty		Maximum TVD		Minimum TVD	
Mud density	**BPH**	**Shoe**	**BPH**	**Shoe**	**BPH**	**Shoe**
[s.g.]	**[bar]**	**[bar]**	**[bar]**	**[bar]**	**[bar]**	**[bar]**
1,5	541,4	482,5	546,1	483	536,7	482,1
1,52	548,6	488,9	553,2	489,4	543,8	488,4
1,54	555,8	495,3	560,5	495,8	550,9	494,8
1,56	562,9	501,7	567,8	502,2	558	501,2
1,58	570,1	508,1	575	508,6	565,1	507,6
1,6	577,2	514,5	582,2	515	572,2	514

9.4.3 Effect of uncertainty in geothermal properties

Table 9.19: Effect of uncertainties in geothermal properties with SH = 900 J/kg·K, TC = 1,4 W/m·K

Specific heat capacity		*900*	*J/kg·K*	
Thermal conductivity		*1,4*	*W/m·K*	
	Min TVD		Max TVD	
Bit depth	**BHP**	**Shoe**	**BHP**	**Shoe**
MD [m]	**[Bar]**	**[Bar]**	**[Bar]**	**[Bar]**
4300	496,8	495	498,1	496,1
6500	553	497,7	563,1	498,7

Table 9.20: Effect of uncertainties in geothermal properties with SH = 1500 J/kg·K, TC = 1,4 W/m·K

Specific heat capacity		*1500*	*J/kg·K*	
Thermal conductivity		*1,4*	*W/m·K*	
	Min TVD		Max TVD	
Bit depth	**BHP**	**Shoe**	**BHP**	**Shoe**
MD [m]	**[Bar]**	**[Bar]**	**[Bar]**	**[Bar]**
4300	497	495,1	498,2	496,3
6500	553,8	498	563,6	499

Table 9.21: Effect of uncertainties in geothermal properties with SH = 900 J/kg·K, TC = 3 W/m·K

Specific heat capacity		*900*	*J/kg·K*	
Thermal conductivity		*3*	*W/m·K*	
	Min TVD		Max TVD	
Bit depth	**BHP**	**Shoe**	**BHP**	**Shoe**
MD [m]	**[Bar]**	**[Bar]**	**[Bar]**	**[Bar]**
4300	498	496,1	499,3	497,3
6500	554,5	498,6	564,4	499,7

Table 9.22: Effect of uncertainties in geothermal properties with SH = 1500 J/kg·K, TC = 3 W/m·K

Specific heat capacity		*1500*	*J/kg·K*	
Thermal conductivity		*3*	*W/m·K*	
	Min TVD		Max TVD	
Bit depth	**BHP**	**Shoe**	**BHP**	**Shoe**
MD [m]	**[Bar]**	**[Bar]**	**[Bar]**	**[Bar]**
4300	498,1	496,2	499,4	497,4
6500	554,9	498,9	564,7	499,9

9.4.4 Effect of uncertainty in oil – water ratio of mud

Table 9.23: Effect of uncertainties in oil – water ratio of mud with OWR = 1

Oil-Water ratio		*1*		
Specific heat capacity		*1693*	*J/kg·K*	
Thermal conductivity		*0,57*	*W/m·K*	
	Min TVD		Max TVD	
Bit depth	**BHP**	**Shoe**	**BHP**	**Shoe**
MD [m]	**[Bar]**	**[Bar]**	**[Bar]**	**[Bar]**
4300	497,6	495,7	499,1	497,2
6500	553,8	498	564	499,3

Table 9.24: Effect of uncertainties in oil – water ratio of mud with OWR = 2

Oil-Water ratio		*2*		
Specific heat capacity		*1417*	*J/kg·K*	
Thermal conductivity		*0,47*	*W/m·K*	
	Min TVD		Max TVD	
Bit depth	**BHP**	**Shoe**	**BHP**	**Shoe**
MD [m]	**[Bar]**	**[Bar]**	**[Bar]**	**[Bar]**
4300	497,2	495,3	498,5	496,5
6500	554	498,2	563,8	499,3

Table 9.25: Effect of uncertainties in oil – water ratio of mud with OWR = 3

Oil-Water ratio		*3*		
Specific heat capacity		*1282*	*J/kg·K*	
Thermal conductivity		*0,42*	*W/m·K*	
	Min TVD		Max TVD	
Bit depth	**BHP**	**Shoe**	**BHP**	**Shoe**
MD [m]	**[Bar]**	**[Bar]**	**[Bar]**	**[Bar]**
4300	497,1	495,2	497,9	496
6500	554,2	498,3	563,4	499

9.5 Tabulated data – Case 3

9.5.1 Effect of wellbore position uncertainty

Table 9.26: Pressure effects by wellbore position uncertainty

		No uncertainty		Maximum TVD		Minimum TVD	
Bit depth	**Bit depth**	**BHP**	**Shoe**	**BHP**	**Shoe**	**BHP**	**Shoe**
TVD [m]	**MD [m]**	**[bar]**	**[bar]**	**[bar]**	**[bar]**	**[bar]**	**[bar]**
3582,10	6600	649,7	646,3	654,4	651,4	644	640,7
3602,52	6800	655	646,6	660,5	651,7	649	641
3622,94	7000	661	647,5	666,7	652,5	654,7	641,9
3643,36	7200	666,9	648,3	672,9	653,4	660,3	642,7
3663,78	7400	672,8	649,2	679,1	654,2	666	643,5
3684,20	7600	678,7	650	685,3	655,1	671,6	644,4
3724,08	7800	687,8	650,8	693,6	655,9	681,6	645,1
3811,80	8000	704,5	651,4	709,3	656,5	699,3	645,7
3980,05	8250	734,7	652	738,3	657,2	730,6	646,3

9.5.2 Effect of mud density uncertainty

Table 9.27: Mud density – and wellbore position uncertainty at 6600 m

Bit Depth	*6600*					
	No Uncertainty		Maximum TVD		Minimum TVD	
Mud density	**BPH**	**Shoe**	**BPH**	**Shoe**	**BPH**	**Shoe**
[s.g.]	**[bar]**	**[bar]**	**[bar]**	**[bar]**	**[bar]**	**[bar]**
1,64	634,4	631	639,5	636	628,8	625,6
1,66	642	638,7	647,2	643,7	636,4	633,1
1,68	649,7	646,3	654,4	651,4	644	640,7
1,7	657,4	654	662,7	659,1	651,6	648,3
1,72	665,1	661,6	670,5	666,8	659,2	655,9

Table 9.28: Mud density – and wellbore position uncertainty at 7400 m

Bit Depth	*7400*					
	No Uncertainty		Maximum TVD		Minimum TVD	
Mud density	**BPH**	**Shoe**	**BPH**	**Shoe**	**BPH**	**Shoe**
[s.g.]	**[bar]**	**[bar]**	**[bar]**	**[bar]**	**[bar]**	**[bar]**
1,64	656,9	633,8	663,1	638,7	650,2	628,3
1,66	664,9	641,5	671,1	646,5	658,1	635,9
1,68	672,8	649,2	679,1	654,2	666	643,5
1,7	680,8	656,9	687,2	662	673,8	651,2
1,72	688,7	664,6	695,2	669,8	681,7	658,8

Table 9.29: Mud density – and wellbore position uncertainty at 8250 m

Bit Depth	*8250*					
	No Uncertainty		Maximum TVD		Minimum TVD	
Mud density	**BPH**	**Shoe**	**BPH**	**Shoe**	**BPH**	**Shoe**
[s.g.]	**[bar]**	**[bar]**	**[bar]**	**[bar]**	**[bar]**	**[bar]**
1,64	717,3	636,6	720,8	641,6	713,3	631
1,66	726	644,3	729,6	649,4	721,9	638,7
1,68	734,7	652	738,3	657,2	730,6	646,3
1,7	743,4	659,8	747,1	665	739,3	654
1,72	752,1	667,5	755,9	672,8	748	661,7

9.5.3 Effect of uncertainty in geothermal properties

Table 9.30: Effect of uncertainties in geothermal properties with SH = 900 J/kg·K, TC = 1,4 W/m·K

Specific heat capacity	*900*	*J/kg·K*		
Thermal conductivity	*1,4*	*W/m·K*		
	Min TVD		Max TVD	
Bit depth	**BHP**	**Shoe**	**BHP**	**Shoe**
MD [m]	**[Bar]**	**[Bar]**	**[Bar]**	**[Bar]**
6600	640,7	637,5	651,6	648,2
8250	726	643,5	733	653,7

Table 9.31: Effect of uncertainties in geothermal properties with SH = 1500 J/kg·K, TC = 1,4 W/m·K

Specific heat capacity	*1500*	*J/kg·K*		
Thermal conductivity	*1,4*	*W/m·K*		
	Min TVD		Max TVD	
Bit depth	**BHP**	**Shoe**	**BHP**	**Shoe**
MD [m]	**[Bar]**	**[Bar]**	**[Bar]**	**[Bar]**
6600	641,1	637,9	652	648,6
8250	726,6	643,9	734,3	654,6

Table 9.32: Effect of uncertainties in geothermal properties with SH = 900 J/kg·K, TC = 3 W/m·K

Specific heat capacity	*900*	*J/kg·K*		
Thermal conductivity	*3*	*W/m·K*		
	Min TVD		Max TVD	
Bit depth	**BHP**	**Shoe**	**BHP**	**Shoe**
MD [m]	**[Bar]**	**[Bar]**	**[Bar]**	**[Bar]**
6600	641,6	638,4	652,6	649,1
8250	721,1	643,9	734,8	654,7

Table 9.33: Effect of uncertainties in geothermal properties with SH = 1500 J/kg·K, TC = 3 W/m·K

Specific heat capacity	*1500*	*J/kg·K*		
Thermal conductivity	*3*	*W/m·K*		
	Min TVD		Max TVD	
Bit depth	**BHP**	**Shoe**	**BHP**	**Shoe**
MD [m]	**[Bar]**	**[Bar]**	**[Bar]**	**[Bar]**
6600	641,8	638,6	652,8	649,3
8250	727,5	644,2	735,1	655

9.5.4 Effect of uncertainty in oil – water ratio of mud

Table 9.34: Effect of uncertainties in oil – water ratio of mud with OWR = 3

Oil-Water ratio		*3*		
Specific heat capacity		*1189*	*J/kg·K*	
Thermal conductivity		*0,45*	*W/m·K*	
	Min TVD		Max TVD	
Bit depth	**BHP**	**Shoe**	**BHP**	**Shoe**
MD [m]	**[Bar]**	**[Bar]**	**[Bar]**	**[Bar]**
6600	640,8	637,6	651,7	648,3
8250	726,2	643,4	733,7	654,1

Table 9.35: Effect of uncertainties in oil – water ratio of mud with OWR = 5

Oil-Water ratio		*5*		
Specific heat capacity		*1071*	*J/kg·K*	
Thermal conductivity		*0,39*	*W/m·K*	
	Min TVD		Max TVD	
Bit depth	**BHP**	**Shoe**	**BHP**	**Shoe**
MD [m]	**[Bar]**	**[Bar]**	**[Bar]**	**[Bar]**
6600	641,1	637,9	652	648,6
8250	726,6	643,7	734,3	654,5

Table 9.36: Effect of uncertainties in oil – water ratio of mud with OWR = 7

Oil-Water ratio		*7*		
Specific heat capacity		*1012*	*J/kg·K*	
Thermal conductivity		*0,36*	*W/m·K*	
	Min TVD		Max TVD	
Bit depth	**BHP**	**Shoe**	**BHP**	**Shoe**
MD [m]	**[Bar]**	**[Bar]**	**[Bar]**	**[Bar]**
6600	641,3	638,1	652,2	648,8
8250	726,7	643,9	734,5	654,7

References

[1] H. Hodne, A. Saasen and K. Tellefsen, "BIP 200 Drilling and Well Fluids Technology," University of Stavanger - Compendium, Stavanger, 2011.

[2] C. Wolff and J. de Wardt, "Borehole Position Uncertainty - Analysis of Measuring Methods and Derivation of systematic Error Model," *Journal of Petroleum Technology*, vol. 33, no. 12, pp. 2339-2350, 1981.

[3] H. Williamson, "Accuracy Prediction for Directional Measurement While Drilling," in *SPE 67616*, Revised for publication from SPE 56702, presented at the 1999 SPE Annual Technical Conference and Exhibition held in Houston, Texas, 3-6 October., 2000.

[4] J. Walstrom, A. Brown and R. Harvey, "An Analysis of Uncertainty in Directional Surveying," in *Journal of Petroleum Technology (SPE 2181)*, Presented at SPE 43rd Annual Fall Meeting held in Houston, Tex. Sept. 29 Oct. 1968., 1969.

[5] J. L. Thorogood, "Instrument Performance Models and Their Application to Directional Surveying Operations," in *SPE 18051*, First presented at the 1988 SPE Annual Technical Conference and Exhibition held in Houston, 2-5 October, 1990.

[6] R. Ekseth, "Uncertainties in connection with the determinaton of wellbore positions," Department of Petroleum Engineering and Applied Geophysics, The Norwegian University of Science and Technology, Trondheim, 1998.

[7] "ISCWSA," The Industry Steering Committee on Wellbore Survey Accuracy, [Online]. Available: www.iscwsa.org. [Accessed 2 April 2013].

[8] T. Torkildsen, S. T. Håvardstein, J. Weston and R. Ekseth, "Prediction of Wellbore Position Accuracy When Surveyed With Gyroscopic Tools," in *SPE 90408*, Presented at the 2004 Annual Technical Conference and Exhibition, Houston, 26-29 September, and revised for publication. Revised manuscripc approved 09 September 2007, 2008.

[9] K. Tellefsen, S. Ding, A. Saasen, P. Amundsen, A. Fjogstad and T. Torkildsen, "The Effect of Drilling Fluid Content on Magnetic Shielding of Downhole Compasses in MWDs," in *SPE 150548*, Presented at the SPE Deewater Drilling and Completion Conference held in Galveston, Texas, USA, 20-21 June, 2012.

[10] H. Williamson and H. Wilson, "Directional Drilling and Earth Curvature," in *SPE 62114*, Revised for publication from paper SPE 56013, presented 30 November 1998, 2000.

[11] P. Weijermans, J. Ruszka, H. Jamshidian and M. Matheson, "Drilling with Rotary Steerable Systems Reduces Wellbore Tortuosity," in *SPE/IADC 67715*, Presented at the SPE/IADC Drilling Conference held in Amsterdam, The Netherlands, 27 February - 1 March 2001, 2001.

[12] JoshDif, "Wikipedia," 21 February 2012. [Online]. Available: http://en.wikipedia.org/wiki/File:Triaxial_Ellipsoid.jpg. [Accessed 18 March 2013].

[13] E. W. Weisstein, The CRC concise encyclopedia of mathematics, Illinois, USA: CRC Press, 1998.

[14] IRIS, *Drilling model - internal course.*

[15] E. Cayeux, "Transient Cutting Transport Model - ROP Management and Improvements," SBBU - Centre for Drilling and Wells for Improved Recovery, Report produced by IRIS for for ConocoPhilips, DetNorske, NFR, Statoil, Talisman, Total and Wintershall. Access restricted, 2012.

[16] P. Isambourg, B. Anfinsen and C. Marken, "Volumetric Behavior of Drilling Muds at High Pressure and High Temperature," in *SPE 36830*, Presented at the 1996 SPE European Petroleum Conference held in Milan, Italy, 22-24 October 1996, 1996.

[17] E. C. Robertson, "Thermal Propertioes of Rocks," United States Department of The Interior Geological Survey, 1988, pp. 88-441.

[18] R. E. Toft, "Influence of the Thermo-Physical Parameters of Formation Rock on Temperature Modelling, and Comparison With Rocorded Data From a Drilling

Operation," University of Stavanger, 2011.

[19] A. Kumar, A. P. Singh and R. Samuel, "Analythical Model to Predict the Effect of Pipe Friction on Downhole Temperatures for Extended-Reach Drilling (ERD)," in *IADC/SPE 151254*, Presented at the 2012 IADC/SPE Drilling Conference and Exhibition held in San Diego, California, USA, 6-8 March 2012, 2012.

[20] A. Pilehvari, J. Azar and S. Shirazi, "State-Of-the-Art Cuttings Transport in Horizontal Wellbores," in *SPE 37079*, Presented at the 1996 SPE International Conference on Horizontal Well Technology held in Calgary, 18-20 November, 1999.

[21] R. Clark and K. Bickham, "A Mechanistic Model for Cuttings Transport," in *SPE 28306*, Prepared for presentation at the SPE 69th Annual Technical Conference and Exhibition held in New Orleans LA U.S.A., 25-28 September 1994, 1994.

[22] Y. Rao, "Generalized compressibility factor correlation," in *Chemical Engineering Thermodynamics*, Hyderguda, Hyderabad, India, University Press, 1997, p. 63.

[23] E. Cayeux, "Emblement of DrillScence for Foam Circulation," IRIS - Stavanger, Report produced for OMW "Confidential", 2012.

[24] E. Cayeux, B. Daireaux, E. Dvergsnes and F. Florence, "Toward Drilling Automation: On the Necessity of Using Sensors That Relate to Physical Models," in *SPE/IADC SPE-163440-MS*, Presented at the SPE/IADC Drilling Conference and Exhibition held in Amsterdam, The Netherlands 5-7 March 2013, 2013.

[25] E. C. Bingham, Fluidity and Plasticity, New York: McGraw-Hill Book Co., Inc., 1922.

[26] O. Skjeggestad, Boreslam Teknologi, 1989.

[27] R. Robertson and H. Stiff, Jr., "An Improved Mathematical Model for Relating Shear Stress to Shar Rate in Drilling Fluids and Cement Slurries," in *SPE 5333*, Presented at the SPE-AIME Rocky Mountain Regional Meeting held in Denver, Colo. April 7-9 1975, 1976.

[28] W. Herschel and R. Bulkley, "Konsistenzmessungen von Gummi-Benzollösungen," in *Kolloid-Zeitschrift*, vol. 39, Leipzig, 1926, pp. 291-300.

[29] M. Versan Kok and T. Alikaya, "Effect of Polymers on the Rheologicla Properties of KCL/Polymer Type Drilling Fluids," Department of Petroleum and Natural Gas Engineering Middle East Technical University, Ankara, Turkey, 2005.

[30] O. Houwen and T. Geehan, "Rheology of Oil-Base Muds," in *SPE 15416*, Presented at the 61st Annual Technical Conference and Exhibition of the Society of Petroleum Engineers held in New Orleans LA OCtober 5-8 1986, 1986.

[31] E. Cayeux, "IRIS Report 2012/346," 2013.

[32] A. Einstein, "Eine Neue Bestemmung Der Moleküldimensionen," University of Zürich, 1906.

[33] E. Hastcheck, "Die Viskosität Der Dispersoide," in *Kolloid-Zeitschrift*, vol. 8, 1910, pp. 34-39.

[34] E. Llewellin, S. Wilson and H. Mader, "The rheology of a bubbly liquid," *The Royal Society London Series A*, no. 458, pp. 987-1016, 2002.

[35] M. Johnson and N. Ryan, "Transition from laminar to turbulent flow in pipes," *AIChE Journal*, vol. 5, no. 4, pp. 433-435, 1959.

[36] EXLOG, Theory and Application of Drilling Fluid Hydraulics, IHRDC, Boston, Massachusetts, USA, 1985.

[37] V. C. Kelessidis, P. Dalamarinis and R. Maglione, "Experimental study and predictions of pressure losses of fluids modeled as Herschel–Bulkley in concentric and eccentric annuli in laminar, transitional and turbulent flows," *Journal of Petroleum Science and Engineering*, no. 77, pp. 305-312, 2011.

[38] K. Founargiotakis, V. Kelessidis and R. Maglione, "Laminar, transitional and turbulent flow of Herschel-Bulkley fluids in concentric annulus," in *The Canadian Journal of*

Chemical Engineering, vol. 86, 2008, pp. 676-683.

[39] M. Haciislamoglu and U. Cartalos, "Practical Pressure Loss Predictions in Realistic Annular Geometries," in *SPE 28304*, Presented at the SPE 69th Annual Technical Conference and Exhibition held in New Orleans LA, U.S.A, 25-28 September 1994, 1994.

[40] A. Ramadan, M. Enfins, H. Miftah-El-Kheir, M. Laget and A. Saasen, "The Effect of Drillstring Rotation on Equivalent Circulation Density: Modeling and Analysis of Field Measurements," in *SPE 135587*, This paper was prepared for presentation at the SPE Annual Technocal Conference and Exhibition held in Florence, Italy, 19-22 September 2010, 2010.

[41] "Extended-Reach Wells," *Oilfield Review*, vol. 22, no. 3, pp. 4-15, 2010.

[42] E. Cayeux, T. Mesagan, S. Tanripada, M. Zidan and K. Fjelde, "Real-Time Evaluation of Hole Cleaning Conditions Using a Transient Cuttings Transport Model," in *SPE/IADC 163492*, Presented at the SPE/IADC Drilling Conference and Exhibition held in Amsterdam, The Netherlands, 5-7 March, 2013.